Methodologies for the Reliable and Efficient Design of Helmet Against Head Injury

A thesis submitted to The University of Manchester for the degree of

Doctor of Philosophy

in the Faculty of Science and Engineering

2022

Shunfeng Li

Department of Mechanical, Aerospace and Civil Engineering

School of Engineering

Contents

Word count: 41,337

List of Figures

List of Tables

Abbreviations

ABS	Acrylonitrile-butadiene-styrene
ANOM	Analysis of mean
BBA	Building block approach
BrIC	Brain injury criterion
CFRP	Carbon fibre reinforced plastics
CSDM	Cumulative strain damage measure
CSF	Cerebrospinal fluid
CT	Computed tomography
DAI	Diffuse axonal injury
EDH	Epidural hematoma
EHSS	Equivalent half-sine shape
EHVS	Equivalent haversine shape
EITS	Equivalent isosceles triangular shape
ENTS	Equivalent negative triangular shape
EPP	Expanded polypropylene
EPS	Expanded polystyrene
EPTS	Equivalent positive triangular shape
ESS	Equivalent square shape

FE	Finite element
FGF	Functionally graded foam
FGPF	Functionally graded polymeric foam
FRP	Fibre reinforced plastics
GAMBIT	Generalized acceleration model for brain injury threshold
GHBMC	Global Human Body Models Consortium
GFRP	Glass fibre reinforced plastics
GSI	Gadd severity index
HIC	Head injury criterion
HIP	Head injury power
ICFEHM	Imperial College finite element head model
ICH	Intracerebral hematoma
KFRP	Kevlar fibre reinforced plastics
LCS	Loading curve shape
MAC	Micro-agglomerate cork
MIPS	Multi-Directional Impact Protection System
MRI	Magnetic resonance imaging
OAD	Orthogonal array design
PC	Polycarbonate
RAIDS	Road Accident In-depth Studies
R-PP-L	Rigid-perfectly plastic-locking
SAH	subarachnoid haemorrhage
SDH	Subdural hematoma
SDOF	Single degree of freedom

SEA	Specific energy absorption
SUFEHM	Strasbourg University finite element head model
TBI	Traumatic brain injury
THUMS	Total Human Model for Safety
UCDBTM	University College Dublin Brain Trauma Model
UDF	Uniform-density foam
ULPFEHM	University of Louis Pasteur finite element head model
WHO	World Health Organization
WSUHIM	Wayne State University Head Injury Model
WSTC	Wayne state tolerance curve

Nomenclatures

$v(t)$	Translational velocity
$\omega(t)$	Angular velocity
$a(t)$	Translational acceleration
$\alpha(t)$	Angular acceleration
$Z(t)$	Fundamental kinematic parameters, i.e. $v(t)$, $\omega(t)$, $a(t)$, $\alpha(t)$, of the head when subjected to impacts
t	Impact time
Z_m	Maximum value of $Z(t)$
t_1, t_2	Two arbitrary points of time within the impact duration $(t_1 < t_2)$
$G(t)$	Function of generalized acceleration model for brain injury threshold
a_c	Limit for a net translational acceleration
α_c	Limit for a net angular acceleration
n, m, and S	Empirical constants for the function of $G(t)$
M	Mass of the head
$a_i(t)$	Translational components of accelerations $(i = x, y, z)$
$\alpha_i(t)$	Rotational components of accelerations $(i = x, y, z)$
I_{ii}	Principal moments of inertia of the head $(i = x, y, z)$
ω_x	Peak angular velocities of the head in the x-axis directions
ω_y	Peak angular velocities of the head in the y-axis directions

ω_z	Peak angular velocities of the head in the z-axis directions
ω_{xc}	Critical value for ω_x
ω_{yc}	Critical value for ω_y
ω_{zc}	Critical value for ω_z
ICP	Intracranial pressure
σ_v	von Mises stress
ε_p	Maximum principal strain
A_{max}	Peak acceleration transmitted to head (unit: 1 g = 9.8 m/s^2)
ρ	Density of EPS foam
c	Side length of the honeycomb cell
t	Wall thickness of the honeycomb cell
σ_p	Plateau stress of honeycomb under out-of-plane compression
σ_y	Yield stress of the material
$\boldsymbol{x}$	Design variable for optimisation
$L_m(l^n)$	The orthogonal array design
$G_i(\boldsymbol{x})$	Constrain function for optimisation
k	Number of constraints
$R(\boldsymbol{x})$	The objective function for optimisation
R_{new}	The new objective function for optimisation
$P(\boldsymbol{x})$	Penalty function
λ	Scaling factor
V_i	Difference between the proposed constraint and the design results
w^α	Weighting factor
$\rho_f(x)$	Power-law function to determine the density of FGPF

ρ_{f1}	Density at the top end of FGPF
ρ_{f2}	Density at the bottom end of FGPF
x	Distance from the top end of FGPF
T	Thickness of FGPF
n	Gradient exponent that governs the variation of FGPF densities
L_i	i-th independent foam layers of FGPF, $i \in (1, \ldots \ldots, z)$
ε	Compressive strain
ε_y	Yield strain
ε_d	Onset strain of densification
$\Delta\varepsilon_y$	Transition zone at the yield strain
$\Delta\varepsilon_d$	Transition zone at the densification strain
E_0	Initial tangent modulus of EPS foam
E_s	Tangent modulus of the solid material of EPS foam ($E_s = 3.3$ GPa)
A_0	Initial geometric stiffness
Φ_0	Initial relative density
ρ_0	Initial density of EPS foam
ρ_s	Density of the solid material of EPS foam ($\rho_s = 1050$ kg/m^3)
$A(\varepsilon)$	Geometric stiffness
$\Phi(\varepsilon)$	Relative density
$E(\varepsilon)$	Tangent modulus
$\sigma(\varepsilon)$	Compressive stress without consideration of the strain-rate effect
E_1	Tangent modulus of the plateau phase
A_1	Geometric stiffness at yield strain
$\dot{\varepsilon}$	Compressive strain-rate

σ_s	Quasi-static rate-independent stress
σ_d	Dynamic rate-dependent stress
DIF	Dynamic increase factor
$\rho_f^{L_i}$	Density for the corresponding independent foam layers of FGPF
$\varepsilon_d^{L_i}$	Densification strain for the corresponding independent foam layers of FGPF
$\sigma_y^{L_i}$	Yield stress for the corresponding independent foam layers of FGPF
σ_F	Yield stress of FGPF obtained from the analytical solution
σ_{ys}	Yield stress of the solid material of EPS foam (σ_{ys} = 135 MPa)
φ	Volume fracture of foam ($\varphi = 0.9$)
W	Absorbed energy
ε_F	Compressive strain for FGPF
Δ_F	Compressed displacement for FGPF
$\sigma_F(\varepsilon_F)$	Rate-independent stress-strain relations for FGPF
$\sigma_F^d(\varepsilon_F)$	Rate-dependent stress-strain relations for FGPF
d	Structural deflection
$F(x)$	Transient force
m	Mass of FGPF
$A(t)$	Acceleration-time history
T_d	Impact duration for $A(t)$

Abstract

To achieve better helmet protection to prevent head injury in impact accidents, continuous efforts have been made to improve helmet design using advanced materials with a deeper understanding of head injury mechanisms. However, the methodologies for helmet design efficiency from the material level have not received sufficient attention, which restricts the efficiency to improve helmet protection. This thesis aims to develop methodologies for the reliable and efficient design of helmet against head injury from three different underpinning aspects, including the optimisation method for helmet structural design, the analytical method for helmet material analysis and the numerical method to predict head impact responses at the tissue level.

Firstly, a structural optimisation method is developed for efficient and reliable helmet design based on the high biofidelity head-helmet coupled model. The honeycomb-filled helmets coupled with the finite element head models are developed to improve helmet protection against both head kinematics and tissue-level responses. It is found that a reasonable design of honeycomb filler can largely improve helmet protection. Further, an orthogonal array design optimisation method based on the coupled head-helmet modelling is provided to efficiently achieve the optimised geometries of honeycomb filler and liner foam density for the honeycomb-filled helmet design.

Secondly, an analytical method is developed from the material level to quickly characterise the potential advanced materials to guide helmet design. Based on the idealised rigid-perfectly-plastic-locking model of uniform density polymeric foam, a

new analytical model is developed and then numerically validated for the effective characterisation of functionally graded polymeric foam (FGPF) under uniaxial compressions. It is found that the compressive responses of FGPF can be well predicted by the analytical model using three basic material parameters, i.e. gradient exponent and foam densities at top and bottom surfaces. An optimisation study is also implemented here to better the crashworthiness of FGPF.

Thirdly, a quantitative numerical method is developed for a deeper understanding of head impact responses to support effective helmet design. The high biofidelity THUMS head model is employed to study the interactive influences of different translational acceleration loading configurations (i.e. loading curve shape, peak magnitude and impact duration) on head tissue-level responses. The quantitatively interactive effects of loading configurations on head response are determined. In addition, the correlations between head injury criterion (HIC) and tissue-level injury predictors are studied. A good correlation is found between the HIC and maximum principal strain responses.

In general, this research provides several methodologies that cover three important aspects for the reliable and efficient design of helmet against head injury. The optimisation method based on the head-helmet model can significantly improve the computational efficiency of helmet design; the analytical method from the material level can offer a more efficient solution to guide helmet material selection and analysis; the quantitative numerical results on head tissue-level responses can provide a rapid estimation of head injury mechanisms. These methods and findings can support the reliable and efficient design and improvement of the helmet.

Declaration

No portion of the work referred to this thesis has been submitted in support of an application for another degree or qualification of this or any other university or other institute of learning.

Copyright

i.   The author of this thesis (including any appendices and/or schedules to this thesis) owns certain copyright or related rights in it (the "Copyright") and he has given The University of Manchester certain rights to use such Copyright, including for administrative purposes.

ii.   Copies of this thesis, either in full or in extracts and whether in hard or electronic copy, may be made only in accordance with the Copyright. Designs and Patents Act 1988 (as amend) and regulations issued under it or, where appropriate, in accordance with licensing agreements which the University has from time to tie. This age must form part of such copies made.

iii.   The owner of certain copyright, patents, designs trademarks and other intellectual property (the "Intellectual Property") and any reproductions of copyright works in the thesis, for example graphs and tables ("Reproductions"), which may be described in this thesis, may not be owned by the author and may be owned by third parties. Such Intellectual Property and Reproductions cannot and must not be made available for use without the prior written permission of the owner(s) of the relevant Intellectual Property and/or Reproductions.

iv.   Further information on the conditions under which disclosure, publication and commercialisation of this thesis, the Copyright and any Intellectual Property and/or Reproductions described in it may take place is available in the University Intellectual Property Policy (see http://documents.manchester.ac.uk/DocuInfo.aspx?DocID=24420), in any relevant Thesis restriction declarations deposited in the University Library, The University Library's regulations (see http://www.library.manchester.ac.uk/about/regulations/) and in The University's policy on Presentation of Theses.

Acknowledgements

Publications

1. **Shunfeng Li**, Q.M. Li*. Head responses subjected to frontal translational acceleration loads. *International Journal of Mechanical Sciences*, 2022, 231: 107598.

2. **Shunfeng Li**, Q.M. Li*. Response of functionally graded polymeric foam under axial compression. *International Journal of Mechanical Sciences*, 2021, 210: 106750.

3. **Shunfeng Li**, Zhi Xiao, Yunfei Zhang, Q.M. Li*. Impact analysis of a honeycomb-filled motorcycle helmet based on coupled head-helmet modelling. *International Journal of Mechanical Sciences*, 2021, 199: 106406.

4. **Shunfeng Li**, Q.M. Li*. Impact protection performance of a novel helmet design with honeycomb reinforced liner. *MACE PGR Conference 2020*, The University of Manchester, May 2020, Manchester, UK (***Awarded the 2nd Prize for the Best Poster***)

1 Introduction

1.1 Background

Nowadays, head injury is one of the leading causes of death and long-term disability in the world [1]. Each year, approximately 10 million individuals worldwide suffer from head injury [2], in which around 1 million people in Europe are admitted to hospital due to head injury [3] and about 1.7 million head injury cases occur in the United States [4]. In addition, head injury is the highest killer for adults under the age of 40 in China [5]. The high proportion of death and hospitalization due to head injury has caused huge financial loss to society and has caused a tremendous impact on the development of society [6].

Among all the various causes of head injury, road traffic collision accidents continue to dominate others, as shown in Figure 1.1 [7]. According to the World Health Organization (WHO) report in 2018, road traffic mortality rises continuously and steadily with the rapid increase of global motorization from 2000 to 2016; the number reached 1.35 million in 2016, as shown in Figure 1.2 [1]. Motorcyclists are one of the most vulnerable road users in various types of traffic accidents, i.e. the 2019 UK Department of Transport annual report on road casualties showed that the casualty rate per passenger mile for motorcyclists is 26 times higher than that of car occupants [8]. Data analysis of Great Britain's Road Accident In-depth Studies (RAIDS) presented different head injuries that occurred to 267 RAIDS motorcyclists between 2013 and 2020, in which 8.3% sustained a

skull fracture, 3.7% sustained subdural haematoma, 10.1% sustained a subarachnoid haemorrhage and 9.4% sustained a focal brain injury [9]. To increase motorcyclists' safety, wearing a helmet is the only protective measure to prevent or mitigate head injury when subjected to impacts [10].
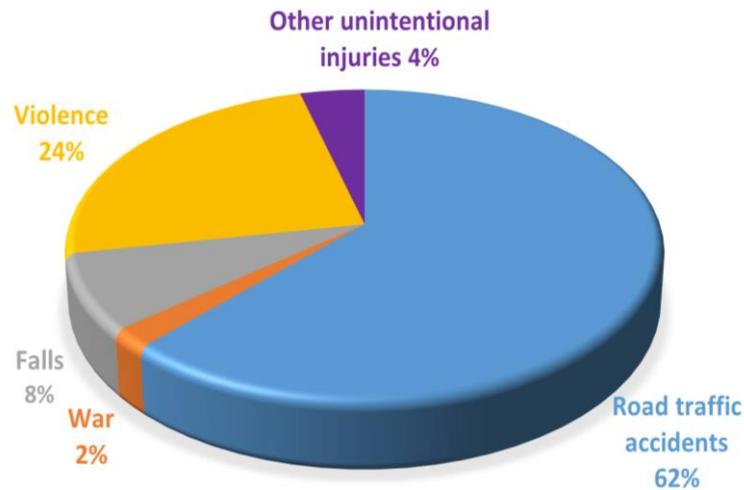
Figure 1.1. Distribution of head injury by causes (redrawn from [7])
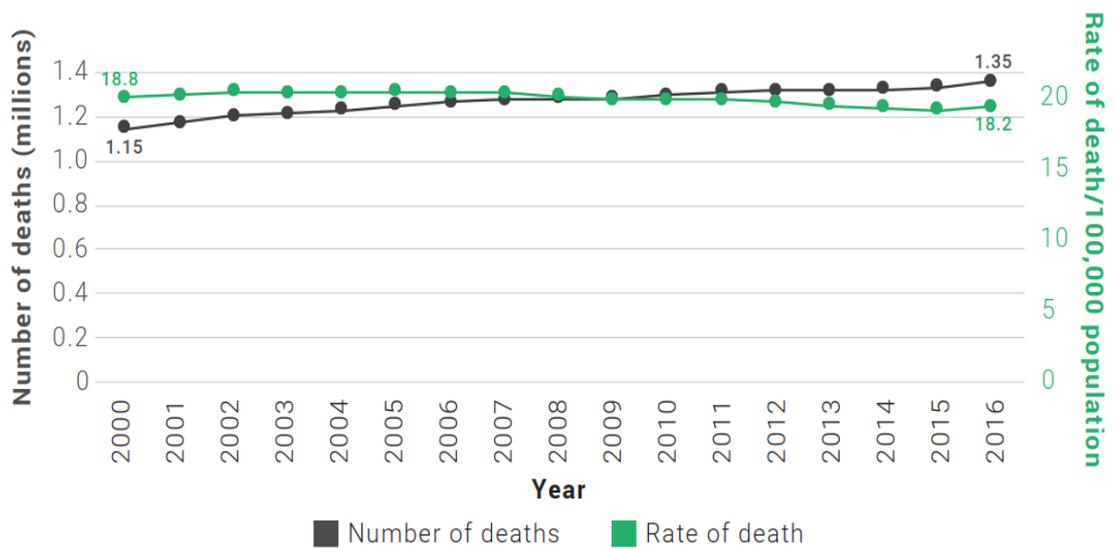
Figure 1.2. Number and rate of traffic death worldwide reported by WHO [1]

1.2   Motivation

As illustrated in Figure 1.3, a typical full-face motorcycle helmet is made up of six basic components, including the rigid outer shell, impact-absorbing liner, comfort/fit padding, face shield, retention system and additional face protection/ventilation system [11]. The impact protection performance of a helmet mostly depends on the rigid outer shell and impact-absorbing inner liner [12]. The thin and stiff helmet shell is commonly made of engineering plastics, such as polycarbonate (PC) and acrylonitrile-butadiene-styrene (ABS), which can disperse the impact loads over a large area to prevent penetration and reduce the direct load on the human head [13, 14]. In addition, the thick and soft helmet liner is often made of polymeric foams, such as expanded polystyrene (EPS) foam and expanded polypropylene (EPP) foam, which can dissipate most impact energy, increase the impact distance and extend the impact duration, thereby reducing the impact loads transmitted to the head [13, 14].
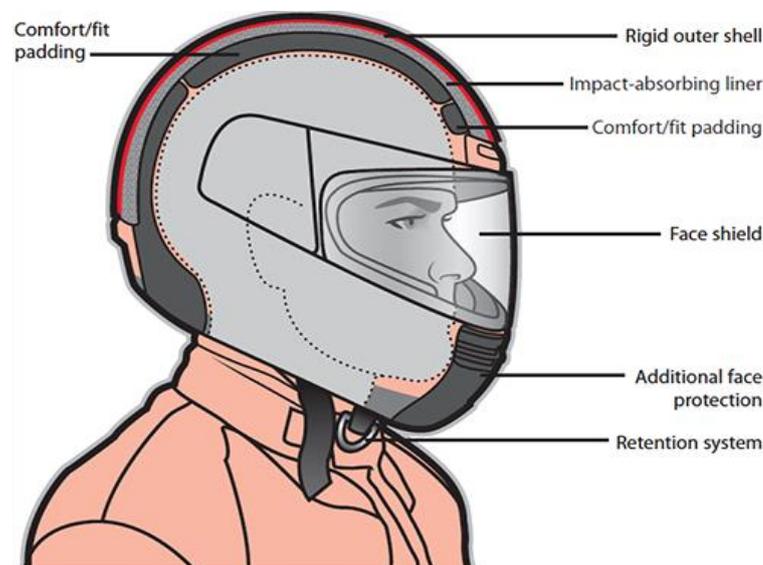
Figure 1.3. Basic components for a typical full-face motorcycle helmet [11]

The main function of a helmet is to maximally absorb collision kinetic energy, attenuate the impact force and prolong the impact duration in order to reduce the impact load and impact energy delivered to the brain and protect the head from various injuries during

impact scenarios [12, 13]. Due to the existence of practical constraints, e.g. space, weight and cost, there is always a protective limit for a designed helmet to prevent the transmission of excessive impact load/acceleration to the head (Figure 1.4) for severe accidents [12]. Thus, continuous efforts have been made to improve helmet design and its protection performance [15-18].
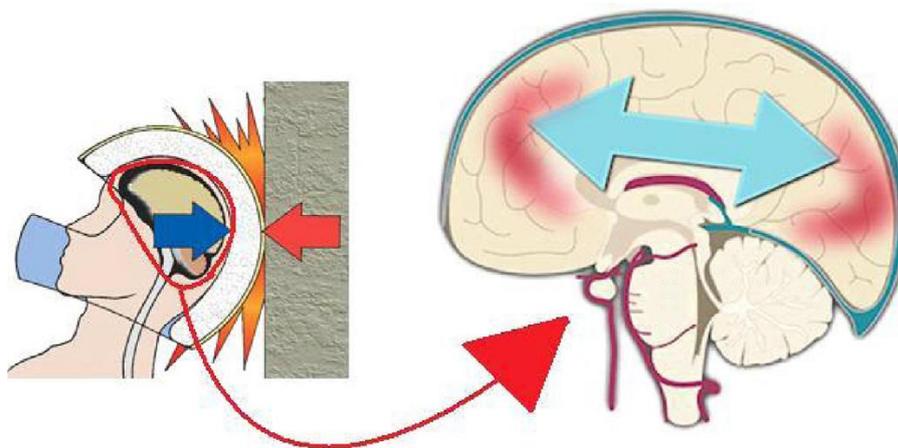
Figure 1.4. The helmeted head injury occurs in an impact accident [12]

A helmet design usually involves the geometrical design and material selection to satisfy both the functional and protective requirements under the imposed constraints, e.g. size, weight and regulations [12, 19-23]. The design of the helmet is an iterative process, during which the helmet performance is predicted by structural analysis and assessed by physical testing at different design stages [24]. With the continuous development of computational mechanics, it becomes feasible to design a helmet using the interactive head-helmet numerical model [25], in which structural optimisation can be adopted to make helmet design more efficient and reliable than a traditional design [26]. Meanwhile, the development of advanced energy-absorbing materials, together with the development of advanced material design, offers an extra dimension for helmet optimisation [27-29]. However, the above-mentioned methodologies for efficient and optimal helmet design from the material level still have many challenges and research gaps. In this regard, the reported helmet optimisation studies focus more on the overall

head kinematics to assess helmet protection, whereas they have seldom been implemented with tissue-level responses using a helmeted high biofidelity head model [30, 31]. The head responses considered at the tissue level are much more fundamental than the empirical head kinematics for the description of head injuries, and therefore, the use of a high biofidelity head model offers a more reliable and advanced method for helmet design and protection assessment [32]. One of the main obstacles to the use of the high biofidelity head model is the computational efficiency issue associated with the use of a high biofidelity head-helmet coupled model [25, 33-35]. Regarding the material level for helmet design, although the use of advanced impact-attenuating materials can further improve helmet protection by offering many more designable parameters (e.g. material properties and geometrical configurations), too many design parameters demand much more significant computational and experimental resources to find a reasonable optimum material design for the helmet [27, 36, 37]. In addition, the helmeted head cannot fully prevent the occurrence of head injury in accidents, due to the excessive impact load/acceleration transmitted to the head, thus helmet design with a deeper understanding of head injury mechanisms can support effective helmet protection enhancement [13], indicating that the study of head impact responses is also of significance to the reliable and efficient design of helmet [26, 29, 38-41].

1.3 Aim and objectives

This thesis aims to provide the methodologies to support the reliable and efficient optimal design of helmet from the material level. As illustrated in Figure 1.5, three main underpinning aspects need to be addressed to achieve this goal, i.e. (i) developing an effective helmet optimisation method based on the high biofidelity head-helmet modelling, which can improve the reliable and efficient helmet design, (ii) exploring an analytical method to quickly characterise a type of advanced energy-absorbing material,

which can provide a more efficient material selection and analysis for helmet design than that of experimental or numerical methods, and (iii) offering a quantitative numerical method using the high biofidelity head model to further understand the head impact responses and its injury mechanisms, which can also support an effective helmet design.
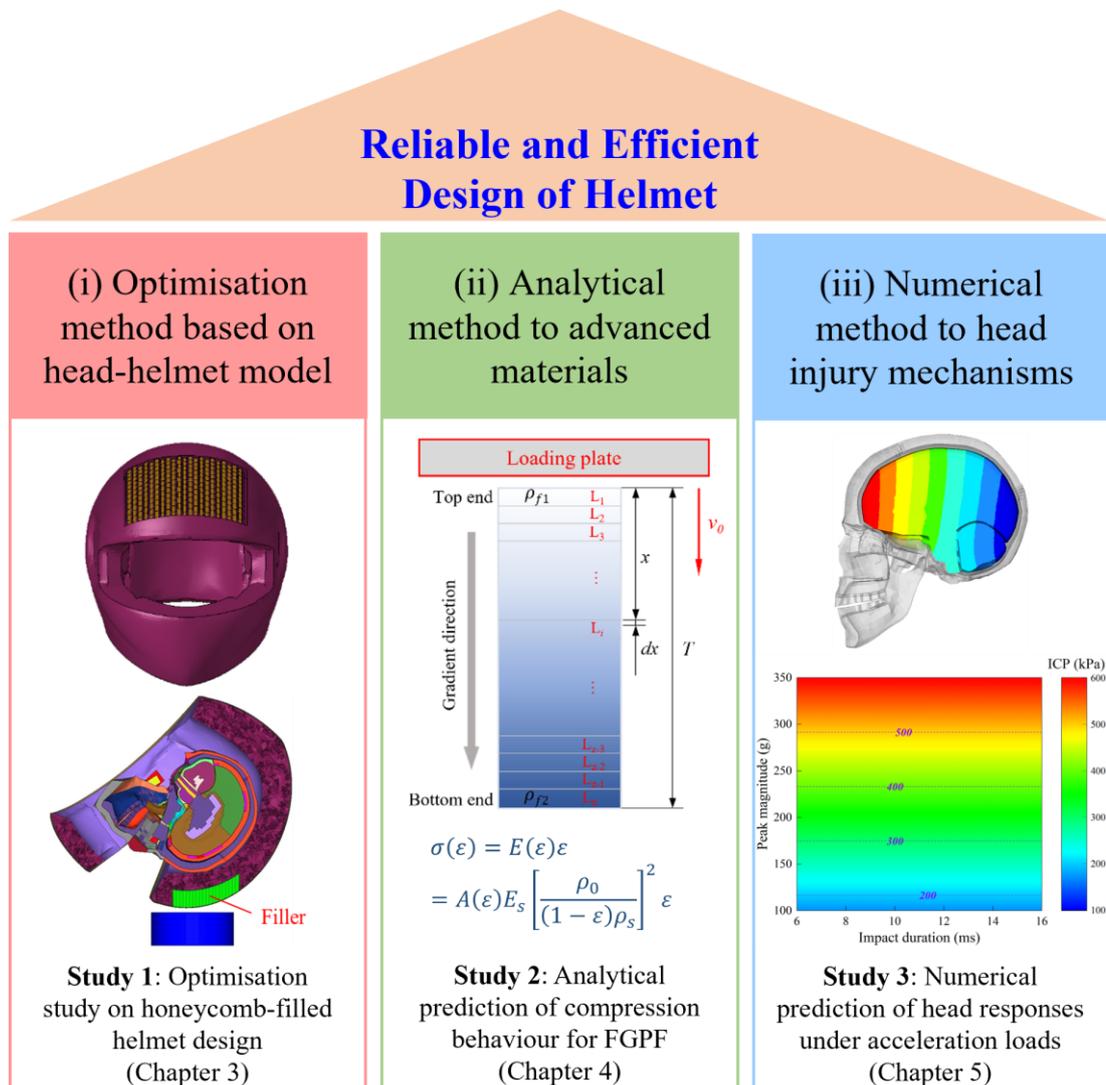
Figure 1.5. Methodologies and their corresponding studies to support the reliable and efficient design of helmet against head injury

As shown in Figure 1.5, three specific studies are presented in this thesis to better show the three mentioned general methodologies to support the reliable and efficient helmet

design. **Study 1-**optimisation study on honeycomb-filled helmet design: a novel helmet design with a honeycomb reinforces helmet liner is selected as an example due to the lightweight and excellent crush resistance performance of aluminium honeycomb as well as the increased design parameters that honeycomb filler can offer, e.g. side length and wall thickness of honeycomb cell, for helmet optimisation [42]. **Study 2-**analytical prediction of compression behaviours for functionally graded polymeric foam (FGPF): FGPF is adopted as an example because FGPF is a type of promising advanced material that can be employed to upgrade the impact-attenuating capacity of the helmet liner as well as compensate excessive stiffness of the composite shells [27]. **Study 3-**numerical prediction of head responses under acceleration loads: impact acceleration can be transmitted to the helmeted head and then cause head injuries [12]. A deeper understanding of head impact responses under different acceleration loads can guide the effective helmet design [43]. The frontal translational acceleration loads with different loading configurations (i.e. curve shape and peak magnitude as well as impact duration) are employed here to demonstrate the methodology.

The corresponding objectives are outlined below.

Study 1: (i) to establish the head-helmet models for replacing the time-consuming, expensive and inflexible experimental helmet design; (ii) to propose a novel honeycomb-filled helmet liner design to improve helmet protection in terms of head kinematic-based and tissue-level injury predictors; (iii) to develop an efficient optimisation method based on the head-helmet modelling for efficiently optimising the design of the honeycomb-filled helmet.

Study 2: (i) to propose an analytical method for quickly characterising the mechanical responses of FGPF under uniaxial compression, which can improve the efficiency of material selection and analysis for helmet design; (ii) to build the

corresponding FGPF FE models for validating the accuracy of proposed FGPF analytical model; (iii) to implement optimisation study for achieving the optimal configuration for the crashworthiness of FGPF under compression loads.

Study 3: (i) to characterise the translational acceleration loads using three key configurations, including loading curve shape, peak magnitude and impact duration, which can be used to simulate different head impact scenarios based on a high biofidelity head model; (ii) to analyse quantitatively the interactive influences of acceleration loading configurations on head tissue-level responses, which can provide a rapid estimation of head response according to the acceleration loads; (iii) to investigate the correlations between tissue-level injury responses and the most used head injury criterion (HIC) for further understanding the head injury mechanisms and injury criteria, which can also support an effective helmet design.

1.4   Outline of this Thesis

The thesis is presented in an alternative format based on published journal papers. Results and their analysis are presented in a self-contained format suitable for presentation in peer-reviewed journals. Symbols are defined in the context of each chapter but may represent different physical parameters in another chapter. All references for each chapter are listed at the end of this thesis. This thesis is organized into the following six chapters.

Chapter 1 comprises a brief introduction to present the background, motivation and aim of this thesis. Figure 1.5 shows three aspects presented in this thesis, each of which corresponds to one possible solution for the efficient and reliable design of helmet against head injury.

Chapter 2 gives a literature review of the studied subject, including the impact

biomechanics of head injury, the development of human head finite element (FE) models and their applications, and potential advanced energy-attenuating materials for the improvement of helmet design. The critical comments on reviewed literature are given and the research gaps in the field of research are further identified.

To improve the reliability and efficiency of helmet design using an efficient structural optimisation method based on the head-helmet coupled modelling, **Chapter 3** develops a methodology for the analysis of a representative motorcycle helmet based on coupled head-helmet FE modelling. The head-helmet model is further employed to investigate a honeycomb-filled helmet design, in which the lightweight honeycomb filler is used to fill the helmet liner to enhance its protectability. Based on the head-helmet modelling, an optimisation method using an orthogonal array design is carried out to efficiently find the optimal design for the honeycomb-filled helmet.

To improve helmet design from the material level by the analytical method, **Chapter 4** studies a potential advanced energy-absorbing material, FGPF, which can be used to improve the design of the helmet liner. Based on the compressive constitutive model of uniform density EPS foam and the idealised rigid-perfectly plastic-locking model for the EPS foam, the analytical model for FGPF is proposed to efficiently predict the compression characteristics of FGPF. A discrete optimisation study is also conducted to maximise the crashworthiness performance of FGPF.

To obtain a deeper understanding of head impact responses and their injury mechanisms that can also support effective helmet design, **Chapter 5** used the high biofidelity head model to study the interactive influences of the peak magnitude and impact duration of frontal translational acceleration loads with different loading curve shapes on head tissue-level injury predictors, i.e. intracranial pressure, von Mises stress and maximum principal strain in the brain. The correlations between *HIC* and tissue-level injury

predictors are further studied.

Chapter 6 draws the main conclusions of this thesis based on the studies presented in the above chapters. Finally, recommendations for possible future research following this thesis are also presented.

2 Literature Review

2.1 Impact biomechanics of the human head

To improve the performance of helmet protection for the reduction of the probability and severity of head injury in impact accidents, it is important to understand the basic anatomical structure of the human head and the knowledge of the impact biomechanics of head injury. Thus, this section introduces the anatomy of the human head and gives the classification and description of different kinds of head injuries and the underlying injury mechanisms. In addition, the head kinematic-based and tissue-level injury predictors are summarised and evaluated to quantify the consequences of head injury.

2.1.1 Anatomy of the human head

The human head is one of the most complex natural structures, as the head consists of the central nervous system, numerous sensory organs, the bony skull structure, meninges and soft skin for their protection and support [44]. Figure 2.1 illustrated the multi-layer structure of the human head, with the outermost layer of skin of scalp followed by the bone of skull, the meninges and the brain [45]. Anatomically, the 5 mm to 7 mm thickness scalp comprises soft tissue layers of dermal skin, subcutaneous connective tissues, a muscle and a fascial layer [44]. Below the scalp, as shown in Figure 2.2, the skeletal bony skull consists of eight cranial bones and 14 facial bones with the thickness varying from 4 mm to 7 mm [46]. Below the skull, the meninges which consist of three different layers of membranes, including the outermost layer of dura mater, the middle layer of arachnoid

mater and the inner layer of pia mater, can support and protect the brain [44]. The pia mater covers the brain, and the gap of the meninges and ventricles of the brain are filled by the cerebrospinal fluid (CSF), which thus can cushion the brain from mechanical shock [44].
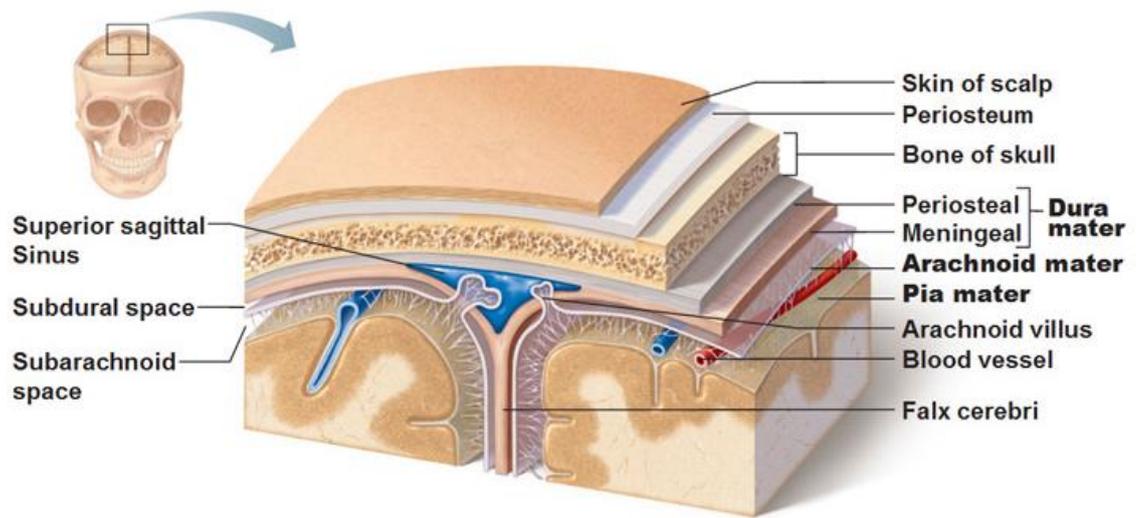
Figure 2.1. Illustration of the multi-layer structure of the head [45]
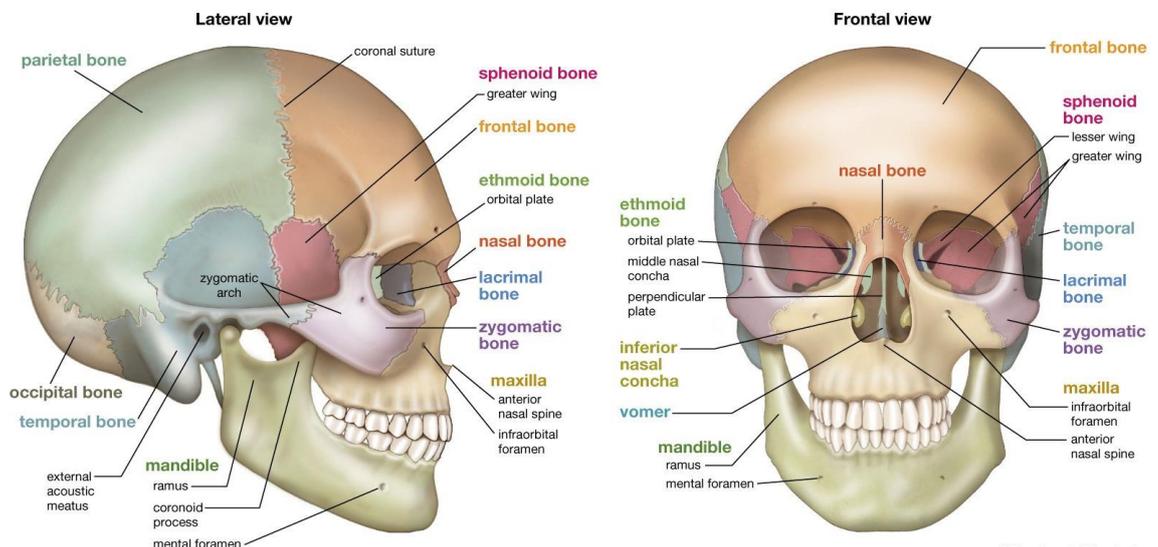
Figure 2.2. Lateral and anterior views of a skull [46]

The average mass of an adult head is around 4.50 ~ 5.00 kg, of which the brain accounts for one-third of the total head weight, while the average masses for the male and female brains are 1.60 kg and 1.45 kg, respectively [47]. The brain is enveloped within the skull

and can be divided into three main parts, including the cerebrum, cerebellum and brainstem, as shown in Figure 2.3 [48]. It can be observed from the figure that, the cerebrum is the largest part of the brain and accounts for 80% of total brain mass, while the cerebellum is the second largest part of the brain accounting for 11% of brain mass [49]. The brainstem originates from the posterior part of the brain and connects the brain adjoining and the spinal cord [48]. As the brain is bathed in the CSF, the brain neither sinks nor floats in the CSF, due to the very similar density of the brain and CSF [47].
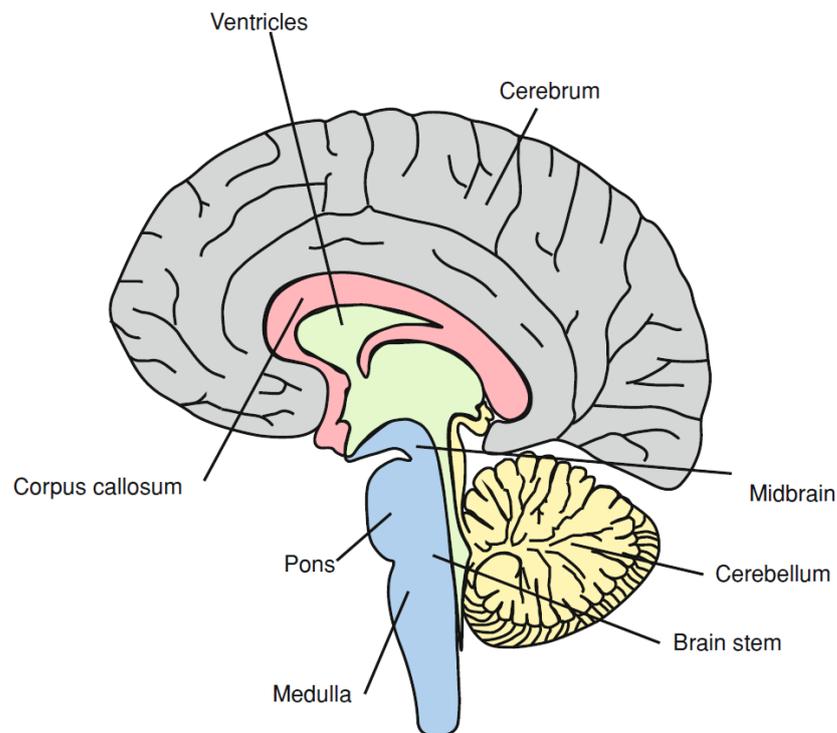
Figure 2.3. The brain in the mid-sagittal plane [48]

2.1.2 Classification of head injury

Many different head injuries can be characterised during impact accidents [50]. To facilitate analysis, a schematic overview of all types of head injury is summarized in Figure 2.4. In principle, open or closed head injuries can be diagnosed according to whether the dura matter is injured (open) or not (closed), head injuries can also be divided into two different types: skull injury and brain injury [51].
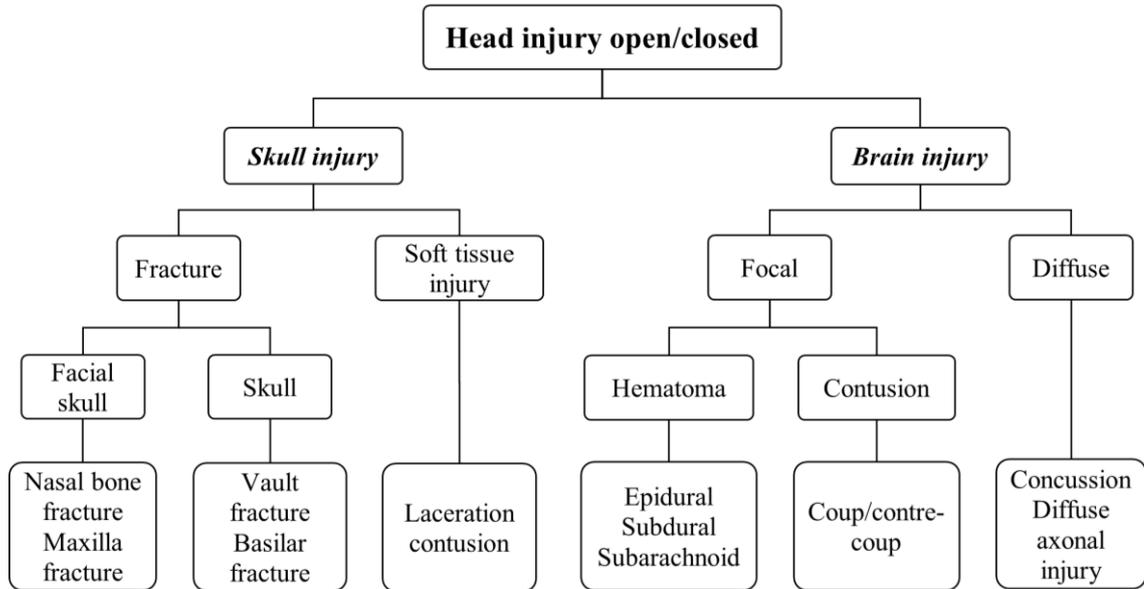
Figure 2.4. Classification of head injury (redrawn from [51])

In terms of skull injury, soft tissue injuries of scalp and facial injuries are commonly found in head injury accidents, but these injuries are regarded as minor or moderate injuries, and more severe injuries to the skull can arise from fractures, e.g. basilar and vault fractures [51]. With respect to the brain, as summarised in Figure 2.4, the injuries are clinically classified into two different forms: focal injury and diffuse injury [52]. The focal brain injury is a lesion that led to local damage which is visible to the eyes, such injury often results in loss of function and a reduction in the amount of brain mass, so the severity of this type of injury is very high [53]. The focal injuries consist of contusions (coup and contrecoup) and three types of hematomas, such as epidural haematoma (EDH), subdural haematoma (SDH), and subarachnoid haemorrhage (SAH) [54, 55]. Diffuse injuries mainly consist of concussion and diffuse axonal injury (DAI), these injuries are invisible to the eyes and can affect a large volume of the brain [51].

Three types of haematomas, i.e. EDH, SDH and SAH, are shown in Figure 2.5 and described as follows. EDH, which forms in the inner surface of skull and the periosteum of the dura mater, is not a frequently occurring head injury [55]. SDH occurs between the

dura matter and brain tissue, and SDH is a highly dangerous brain injury with a high mortality rate of up to 30% [56]. SAH is bleeding in the space between the arachnoid mater and the pia mater [57]. In addition, contusions are the most common focal injury, which frequently occurs at the impact site (resulting in coup contusion) and the opposite site of impact (resulting in contrecoup contusion) [58].
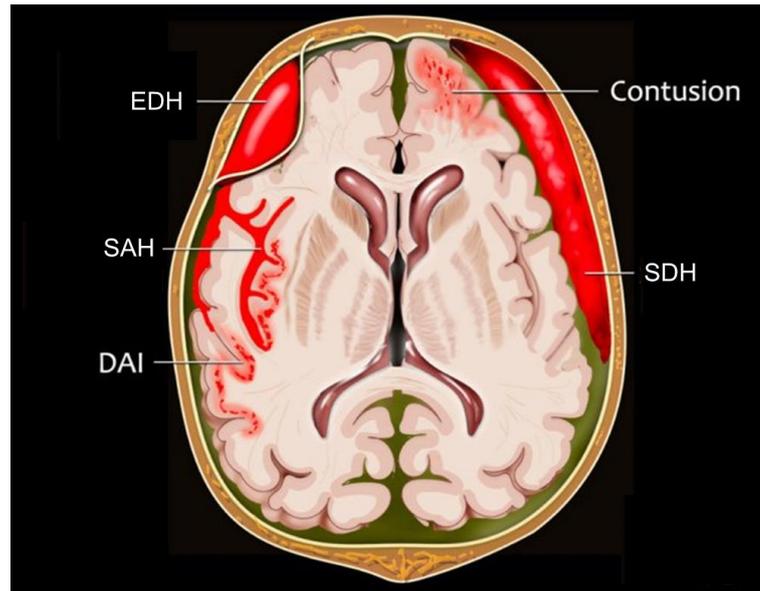
Figure 2.5. Some types of brain trauma (redrawn from [59])

As for diffuse injury to the brain, concussion is also called mild traumatic brain injury, which can lead to temporary impairment of body operations, such as headaches and problems with concentration, memory, balance, coordination, etc [60]. Usually, the angular acceleration that lasts for a long time causes shock and structural deformation of the brain, which leads to a concussion [57]. Diffuse axonal injury (DAI) refers to the mechanical disruption of the axons in the cerebral hemispheres and the subcortical white matter, which is a severe form of traumatic brain injury and usually resulted from shear loadings [51]. DAI is one of the most dangerous head injuries, which is the main cause of disability and even death of patients [57].

2.1.3   Head injury mechanisms

Various head injury mechanisms are presented in Figure 2.6. In principle, head injury is the consequence of static (force applied with a duration more than 200 ms) and/or dynamic (force applied with a duration less than 200 ms) loads during accidents [61]. The static load commonly causes multiple skull fractures after the maximum deformation of the head is reached [51]. The injury caused by a static load is relatively rare in a head injury accident, whereas the dynamic load is the predominately loading scenario in most injury accidents [51]. The dynamic load applied to the head can be classified into two categories, contact and non-contact loads (Figure 2.6), which can lead to different injury responses of the head [51]. Direct or indirect contact impact load to the head can result in the deformation of skull, and then cause fractures on the impact site [62]. Furthermore, focal brain injuries like hematomas or contusions may be observed after skull deformation [53]. Also, rapid contact impact load can produce stress wave propagation within the head, which may lead to a pressure gradient in the brain (Figure 2.7) and then cause focal brain injury [63]. Regarding the non-contact impact situations, sudden acceleration or deceleration results in an inertial load to the head [61]. Acceleration is regarded as translational or rotational. Translational acceleration can make the pressure change in the head which leads to focal brain injury; while rotational acceleration usually caused brain movements and leads to diffuse brain injury [64].
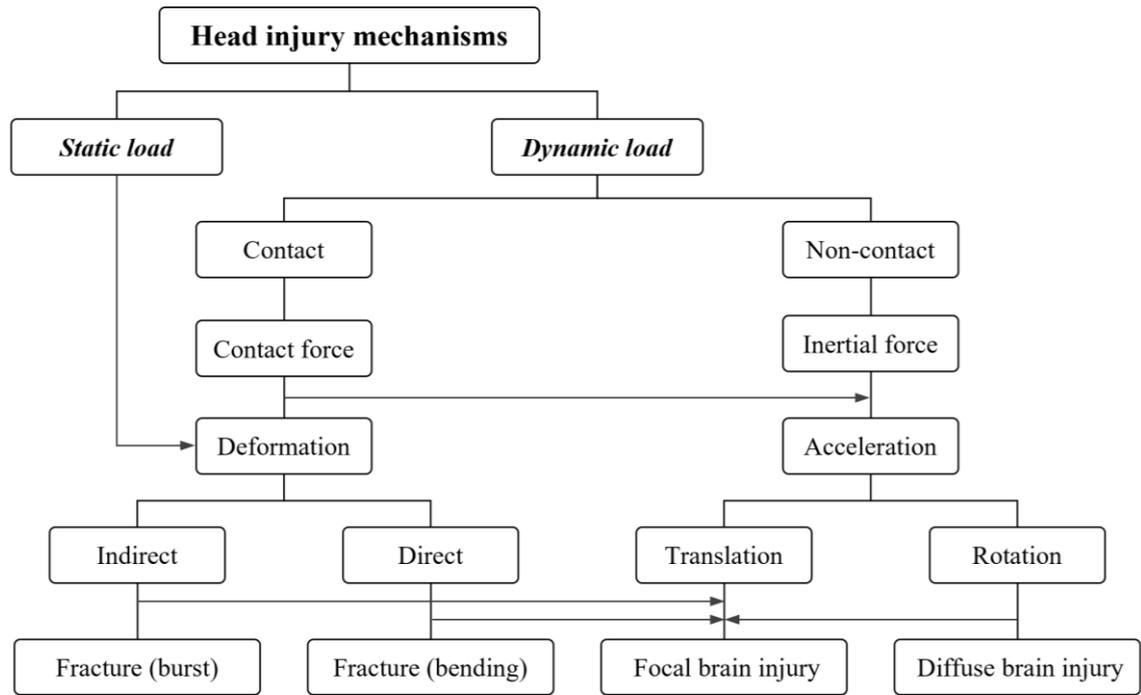
Figure 2.6. Head injury mechanisms caused by mechanical loads (redrawn from [51])
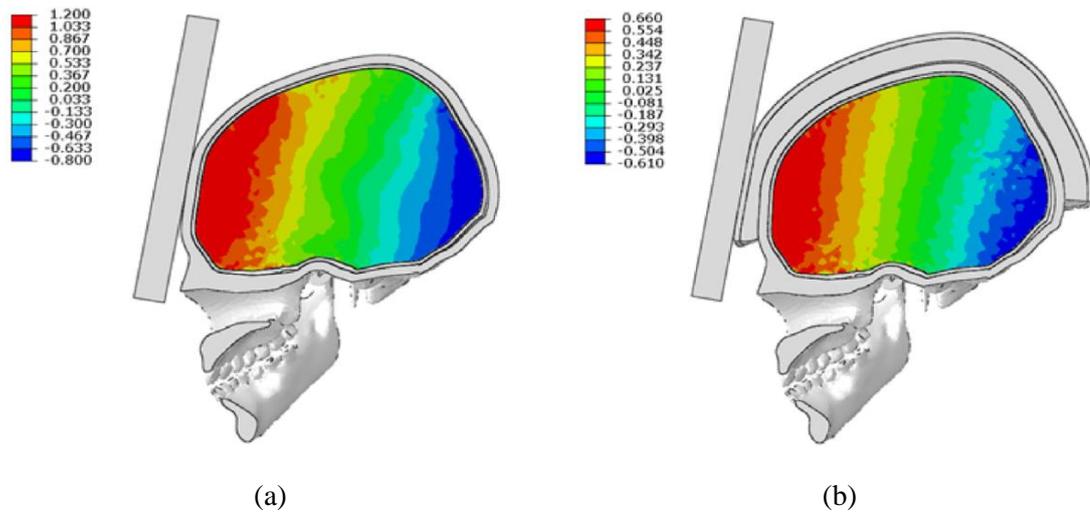
Figure 2.7. Gradient brain pressure distribution during blunt impact, (a) head without helmet protection, (b) head with helmet protection [65]

2.1.4 Head injury predictors

To predict the possibility and severity of head injury in accidents, numerous head kinematic-based and tissue-level injury predictors have been developed. This section introduces several common kinematic-based injury predictors according to their historical developments and the tissue-level injury predictors.

2.1.4.1 Kinematic-based injury predictors

Fundamental kinematic parameters

The fundamental kinematic parameters, e.g. relative displacement, impact velocity and acceleration, can be selected to assess head injury risk using their corresponding maximum values [66], defined as

$$Z_m = \max\{|Z(t)|\}, \tag{2.1}$$

where the parameter $Z(t)$ can represent the translational velocity $v(t)$, angular velocity $\omega(t)$, translational acceleration $a(t)$ and angular acceleration $\alpha(t)$ of the head; and the Z_m denotes the maximum value of these mentioned kinematic parameters.

Gadd severity index

In 1966, the first head injury criteria, the Gadd severity index (GSI), was proposed according to the well-known Wayne State Tolerance Curve (WSTC) which is an acceleration-time tolerance curve obtained from cadaver head impact tests [67], as presented in Figure 2.8. The GSI is defined as

$$GSI = \int a(t)^{2.5} dt, \tag{2.2}$$

where $a(t)$ is the resultant translational acceleration in g's. The $GSI = 1000$ is recommended as the head impact injury threshold [68].
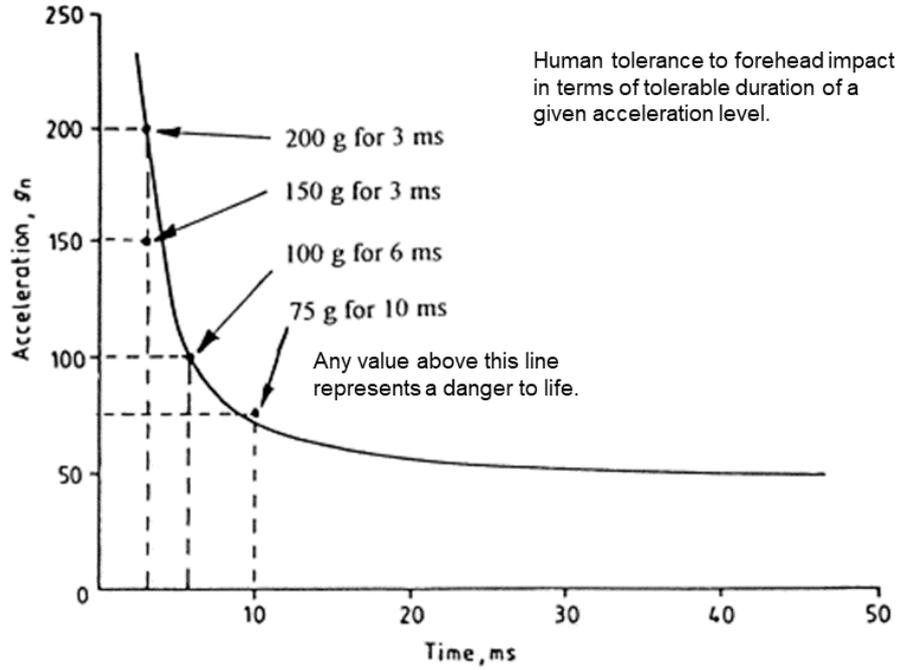
Figure 2.8. Wayne State Tolerance Curve (redrawn by [69])

Head injury criterion

In 1971, the head injury criterion (HIC) was suggested from the GSI to further consider a time average effect during an impact event [70]. Nowadays, HIC is the most common criterion to evaluate the risk of head injury in related head safety protection standards, such as the helmet standards ECE 22.05 [19] and the vehicle safety standard FMVSS 208 [71]. The HIC is defined as

$$HIC = \max_{t_1, t_2} \left\{ (t_2 - t_1) \left[\frac{1}{(t_2 - t_1)} \int_{t_1}^{t_2} a(t) dt \right]^{2.5} \right\}, \tag{2.3}$$

where t_1 and t_2 ($t_1 < t_2$) are two arbitrary points of time (in second) within the impact period. The different time intervals, such as $t_2 - t_1 \leq 15$ ms or 36 ms, can be adopted in the above safety standards to assess head injury by calculating the corresponding HIC values. For example, the threshold HIC value in Standard ECE 22.05 [19] is 2400 to ensure that motorcycle helmet protection can mitigate head injury, while the threshold value of 1000 is adopted in Standard FMVSS 208 [71].

*Generalized acceleration model for brain injury threshold (**GAMBIT**)*

In 1986, the generalized acceleration model for brain injury threshold $(GAMBIT)$ was proposed to combine the effects of both translational and rotational kinematics [72]. The $GAMBIT$ is defined as

$$G(t) = \max\left\{\left[\left(\frac{a(t)}{a_c}\right)^n + \left(\frac{\alpha(t)}{\alpha_c}\right)^m\right]^{1/s}\right\}, \tag{2.4}$$

where $a(t)$ and $\alpha(t)$ are the translational and angular accelerations in g's and rad/s^2, respectively; a_c and α_c represent the respective limits for a net translational and net angular acceleration; n, m, and S are empirical constants, and $n = m = S = 2$, $a_c = 250$ g and $\alpha_c = 25000$ rad/s^2 are adopted in reported studies [73, 74]. The $G(t) = 1$ is considered as the injury threshold for head under impact loads.

Head injury power

In 2000, the head injury power (HIP) was also developed to consider both effects of translational and rotational accelerations [73]. The HIP is defined as

$$HIP = \max\left\{M \sum a_i(t) \int a_i(t)dt + \sum I_{ii}\alpha_i(t) \int \alpha_i(t)dt\right\}, \tag{2.5}$$

where M is the mass of the head, $a_i(t)$ and $\alpha_i(t)$ represent the translational and rotational components of accelerations, respectively; I_{ii} denotes the principal moments of inertia of the head; and subscript i denotes the anatomical axes ($i = x, y, z$). Based on the head impact accident data and analysis, a mild head injury can be predicted when the $HIP = 12.8$ kW [73].

Brain injury criterion

In 2013, the brain injury criterion (BrIC) was proposed to predict brain injury risk due

to the angular velocities [75].

$$BrIC = \sqrt{\left(\frac{\omega_x}{\omega_{xc}}\right)^2 + \left(\frac{\omega_y}{\omega_{yc}}\right)^2 + \left(\frac{\omega_z}{\omega_{zc}}\right)^2}, \qquad (2.6)$$

where ω_x, ω_y and ω_z are the peak angular velocities of the head in three orthogonal directions; the ω_{xc}, ω_{yc} and ω_{zc} are critical angular velocities in their direction that can lead to a 50% probability of severe head injuries when $BrIC = 1$, and $\omega_{xc} = 66.25$ rad/s, $\omega_{yc} = 56.45$ rad/s and $\omega_{zc} = 42.87$ rad/s were determined by using the FE head models [75].

2.1.4.2   *Tissue-level injury predictors*

With the rapid development of computational technology in the FE method over the past decades, many high biofidelity FE head models (see Section 2.2) have been developed and validated for more detailed and accurate computational-based studies of head injury when subjected to impacts [62]. Head tissue-level injury predictors, e.g. intracranial pressure, von Mises stress, maximum principal strain, maximum shear strain, strain-rate and strain energy, can be obtained using the high biofidelity head models to assess head injury [76]. Furthermore, the high biofidelity head models can also be used to consider other strain-based injury predictors, e.g. the cumulative strain damage measure (CSDM), which is the cumulative volume fraction of the brain matter experiencing strains exceeding a defined threshold [55].

In comparison with the tissue-level injury predictors, kinematic-based injury predictors assess head injury by using the empirical functions (Section 2.1.4.1), which were developed based on the pure translational and/or rotational motions of the head [67, 70, 72, 73, 75], implying that kinematic-based predictors lack directional sensitivity. Whereas head injury can be influenced by the impact direction [77, 78]. Tissue-level

predictors can be obtained from the high biofidelity head models without losing the directional effect of loadings on the head responses [76]. On the other hand, kinematic-based predictors use only global head responses to predict head injuries, whereas the tissue-level predictors can correlate the local head responses to head injuries [32]. Therefore, tissue-level predictors are more fundamental and advanced than kinematic-based predictors.

2.1.5   Methods to study head impact responses

To develop more efficient and reliable head safety systems, e.g. protective helmets, it is of great practical significance to investigate the characteristics of head responses to different impacts and the relevant injury mechanisms. Many studies have been undertaken to explore head impact responses using experimental, analytical and numerical methods over the past decades.

In the early stage, the investigation mainly focused on experimental works using living human subjects or cadavers [79-85]. For example, Lissner et al. [79] used the drop test of human cadaveric heads to obtain the head acceleration and its loading duration, based on which the well-known WSTC was proposed, see Figure 2.8. Nahum et al. [81] conducted linear impact tests on human cadaveric heads to obtain data on the impact force, head acceleration and intracranial pressure. Hardy et al. [85] acquired the data on head displacement and deformation during head impact experiments. All these studies [79-85] generated many valuable experimental data and helped to achieve a preliminary understanding of head impact responses and their injury mechanisms. However, increased ethical consideration has led to more stringent regulations on cadaveric tests. Meanwhile, expensive human cadaveric tests can only measure limited testing data. To understand more fundamental mechanics underpinning head injury mechanisms, efforts have been put into analytical studies.

Analytical studies on head injury have been reported in literature [19, 20, 66, 71, 86-91]. Based on the earliest WSTC, the relationship between the average head acceleration and loading duration was developed as the *GSI* [86], which can be used to predict severe head injury. Then, the *GSI* was modified by Versace [87] as the *HIC*, which is the most commonly-used criteria to assess head injury in many safety regulations, such as helmet standards ECE 22.05 [19] and FMVSS 218 [20]. To enhance head injury prevention in impacts, Zhou et al. [89] proposed an analytical model, which includes key parameters in head impact tests, e.g. initial impact velocity, stopping distance and the *HIC*, to identify a preferred design range for stopping distance and reveal the *HIC* sensitivity to impact velocity. In addition, Wu and Beaudet [90] investigated analytically several different head impact waveforms to find optimal waveform to achieve the minimal *HIC*. Recently, Yang and Li [91] further used the *HIC* and equivalent single degree of freedom (SDOF) analytical method to determine the safest deceleration-time history for head impact protection and then present injury boundaries using non-dimensional quantities.

The analytical investigations [19, 20, 66, 71, 86-91] revealed the basic relationship between head kinematics and injury severities, which can help in predicting head injury quickly and guiding the practical design of safety systems for head protection. However, these simplified analytical models cannot represent the detailed anatomical features of the head since the human head is one of the most complex natural structures [62]. This means that analytical models may not sufficiently reflect the realistic head impact circumstances and are unable to predict the detailed tissue-level responses of the head in impact accidents, which are much closer to the direct causes of head injuries. As such, more efforts have been put into the numerical studies using the high biofidelity head models, which are presented in Section 2.2.

2.2 Finite element method for head injury prevention

With the rapid development of computer power and relevant imaging technologies, e.g. computed tomography (CT) imaging technology and magnetic resonance imaging (MRI) technology, over the past decades, accurate and high-resolution anatomically geometries of the head have been obtained for the development of the high biofidelity FE head models [76, 92-94]. Nowadays, these validated high biofidelity head models can measure the tissue-level injury predictors and have become very powerful tools to enhance the study of head injury mechanisms as well as helmet design [41, 95-98]. To obtain more benefits from current FE methods, several typical high biofidelity head models are introduced in this section. It should be noted that there are many differences (e.g. the geometrical sizes, material properties, material models, boundary conditions and skull-brain interface) among the following high biofidelity head models, the complete comparisons among different head models can be found in many review papers [62, 76, 99], thus the comparison of the head models are not presented here to avoid overshadowing the main purposes of this section.

2.2.1 High biofidelity FE head models

2.2.1.1 *Wayne State University head injury model*

Figure 2.9 shows an overview of the Wayne State University head injury model (WSUHIM). The first version of WSUHIM consisting of 6,080 nodes and 7,351 elements was built by Ruan et al. [100] in 1993 and this model was then improved by Zhou et al. [101] in 1995 with 17,656 nodes and 22,995 elements. In 2001, Zhang et al. [102] further developed the model using damageable material properties to represent the facial bone and the skull, and hope that such a model can simulate bony fractures. Furthermore, this head model was continuously revised and updated by Viano et al. [103] in 2005, and the

latest WSUHIM was improved with 281,800 nodes and 314,500 elements, and the detailed anatomical features of a head, such as scalp, skull, meninges, CSF, cerebrum, cerebellum, falx, ventricles, brainstem, were considered in the model. In 2013, Mao et al. [104, 105] updated the WSUHIM and integrated the head model with other parts of the full human body model, i.e. the Global Human Body Models Consortium (GHBMC). Thus, the new model is also known as the GHBMC head model. All these WSUHIMs have been used widely by researchers to investigate head impact injury [106-108].

| (a) | (b) |
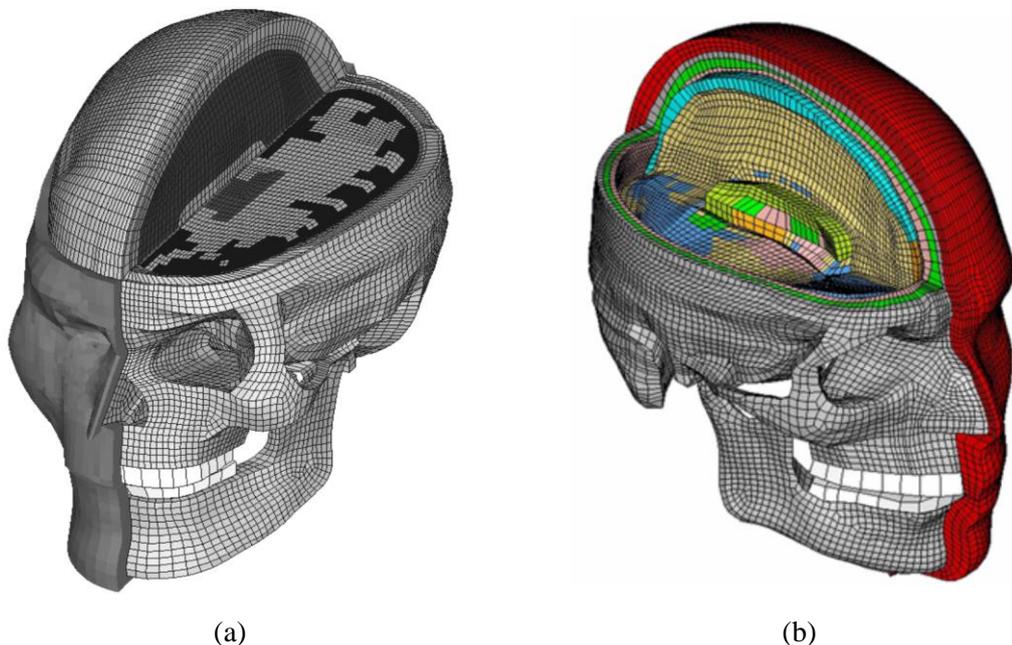
Figure 2.9. (a) Wayne State University head injury model [102], and (b) Global Human Body Models Consortium (GHBMC) head model [104]

2.2.1.2   Strasbourg University finite element head model

Figure 2.10 shows a lateral cross-sectional view of the Strasbourg University finite element head model (SUFEHM), which is also known as the former University of Louis Pasteur finite element head model (ULPFEHM) [109]. Based on the obtained MRI data, Kang et al. [110] first developed the SUFEHM under the commercial FE code RADIOSS in 1997. The model can represent the detailed anatomical features of a head (e.g. skull, scalp, CSF, brain, brainstem, falx and tentorium, etc.) using 11,939 nodes and

13,208 elements. In this model, shell elements were used to simulate the skull, falx and tentorium, while brick elements were adopted to model other parts. To expand the usage of SUFEHM, Deck and Willinger [41] transferred this model to FE code LS-DYNA in 2009. As such, this model has been extensively used in various applications, like traffic accidents, the automotive industry and helmet design [25, 109, 111, 112].
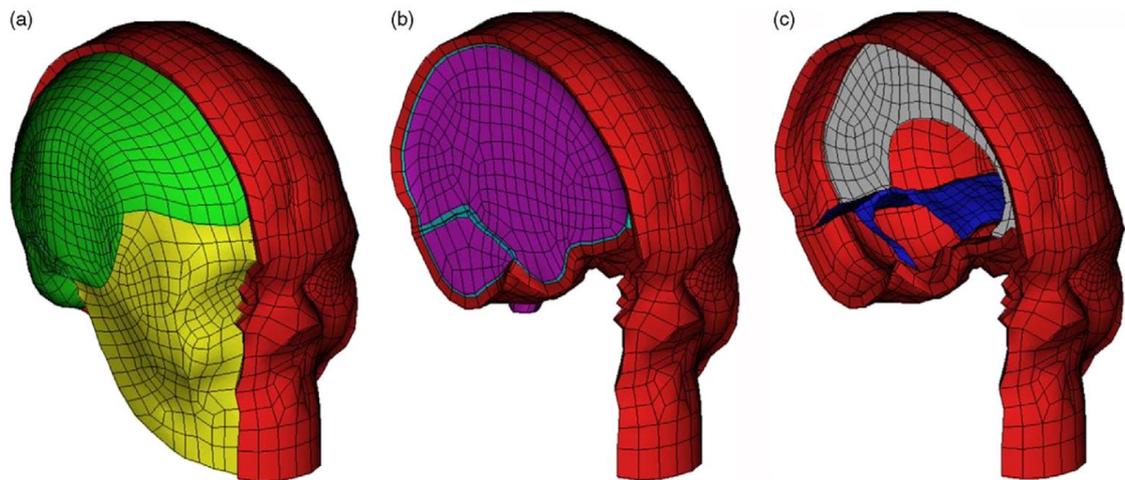
Figure 2.10. Strasbourg University finite element head model [113]

2.2.1.3   *Kungliga Tekniska Högskolan finite element head model*

Figure 2.11 illustrates the Kungliga Tekniska Högskolan finite element head model (KTHFEHM). In 2002, Kleiven and von Holst [114, 115] developed a detailed and parameterised head model, which can simulate different sizes of heads with various element mesh densities. Thus, this model is allowed to scale the dimension of a specific segment of the population and represent the dimension of a particular test specimen. The detailed anatomical features of the head (i.e. skull, facial bones, scalp, CSF, cerebrum, cerebellum, spinal cord, dura mater, falx, tentorium, a simplified neck bone and neck muscles) are established in this model with 19,350 nodes and 18,326 elements. The KTHFEHM now has become a useful tool for the investigation and improvement of head injury prevention [116-119].
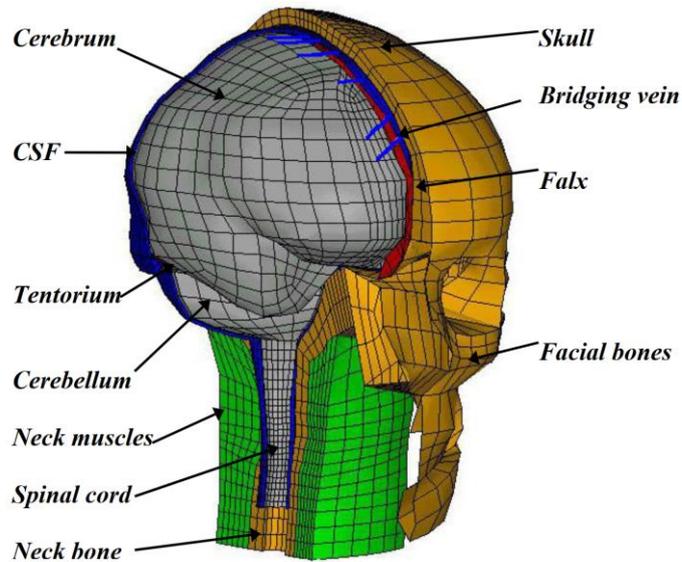
Figure 2.11. Kungliga Tekniska Högskolan finite element head model [120]

2.2.1.4   Total Human Model for Safety head model

Figure 2.12 displays a lateral cross-sectional view of the Total Human Model for Safety (THUMS) head model, which consists of 256,948 elements with mesh sizes ranging from 1.2 mm to 5 mm. Researchers from the Toyota Motor Corporation established the high biofidelity full human body models for the research and development of the automotive industry [121]. The first generation of the THUMS model (Version 1) was released in 2000 to predict the impact behaviours of total human bodies during vehicle collision accidents, the head and brain tissues were simplified as solid parts in this model [122]. In the following years, the THUMS model was continually evolved and significantly improved followed by five more versions (Version 2 in 2005, Version 3 in 2008, Version 4 in 2010, Version 5 in 2015, and Version 6 in 2019) to broaden the scopes of the model with different genders, ages, posture, also to offer more precise reproduction of numerical simulations with finer element size and accurate material properties for each part of the human body [123, 124]. In this regard, the parts of the head, including facial bone, eyeballs, teeth, skin, skull, CSF, falx, cerebrum, cerebellum, mandible, etc., can be well-reflected in the THUMS head model [125]. Various head impact experiments were adapted to continually validate the accuracy of this model [124]. Thus, the THUMS head

models can be applied to different impact loading conditions to predict the tissue-level responses of the head [126-130].
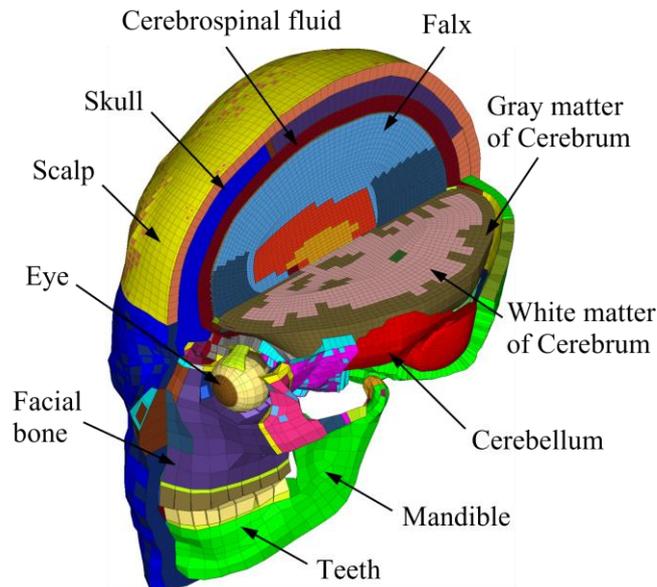
Figure 2.12. Total Human Model for Safety (THUMS) head model

2.2.1.5   *Imperial College finite element head model*

Figure 2.13 shows the high-fidelity Imperial College finite element head model (ICFEHM). Based on the high-resolution MRI data of a 34-year-old male subject, Mazdak et al. [131] developed an in-house code to generate the finite element mesh, and then set up this head model using the commercial FE code LS-DYNA in 2017. Nearly one million hexahedral elements and a quarter of a million quadrilateral elements were used in this model to represent eleven tissues, such as the scalp, skull, brain meninges, CSF, subarachnoid space and ventricles, etc [131]. The very detailed anatomical feature sulci was also established in this model [131]. Recently, the ICFEHM has been increasingly applied to predict brain responses under blunt [98, 132, 133] and blast [134-136] impact loads.
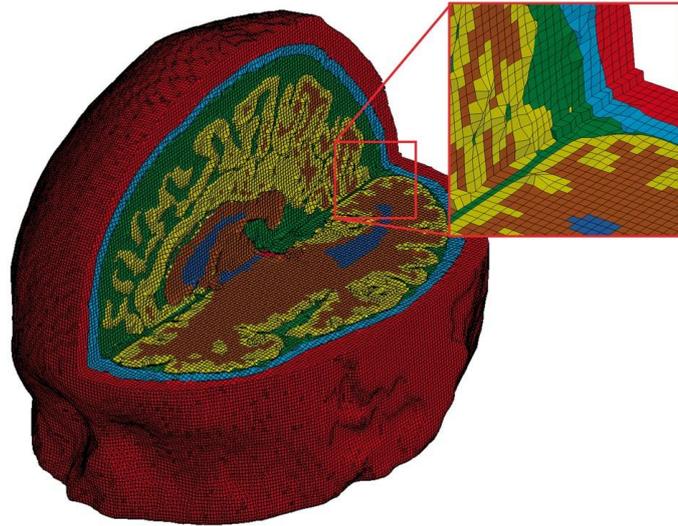
Figure 2.13. Imperial College finite element head model [131]

2.2.2 Head impact responses predicted by the head models

As mentioned in Section 1.2, the helmet cannot completely prevent the excessive impact load/acceleration transmitted to the head, which results in consequent head injury [12]. To improve head impact protection, head models have become a powerful tool to replicate different head impact events to investigate head responses and injury mechanisms [96, 108, 137-143]. Comparing to the use of other impact loading conditions [38, 143], such as the application of impact velocity or impact force to the head, imposed acceleration loading is still a widely accepted and practically applicable loading specification for a head injury [98, 132]. As such, many studies [95, 98, 132, 144-148] have inputted one or several types of acceleration loads into the head models to evaluate head injury, and it was found that head responses are significantly affected by the acceleration loading configurations, e.g. loading curve shapes, peak magnitude and impact duration. In this regard, Kleiven [95] developed KTHFEHM to investigate the effects of impact duration on intracranial pressure and strain, and found a good correlation between the HIC and brain strain responses under translational acceleration loads. Post et al. [144, 145] employed the University College Dublin brain trauma model (UCDBTM) to study the influences of loading curve shape, peak magnitude and

impact duration of impact accelerations on the maximum principal strain and von Mises stress in the brain. The effects of these acceleration loading configurations were also systematically studied by Bian and Mao [146] by considering the strain responses using the GHBMC head model. Overall, these reported results show the effects of each different acceleration loading condition on head responses; however, the interactive influences of peak magnitude and impact duration with different loading curve shapes on the head responses have yet to be revealed clearly.

It is widely known that a deeper understanding of head injury mechanisms can support the effective development of protection systems, e.g. helmets [13]. Thus, to support the effective helmet design, it is of significance to perform numerical studies using the high biofidelity head models to further improve the understanding of head responses when subjected to impacts.

2.2.3   Head models used for the helmet protection

According to helmet standards [19, 20, 22], a headform should be equipped with the helmet to measure the resultant acceleration at the centre of gravity of the headform during the helmet standard drop test, which is to assess the helmet protection performance against head kinematics. The usage of a high biofidelity head model can help to measure more detailed tissue-level injury predictors to assess the helmet protection performance more intuitively and realistically [62, 76, 99]. In general, there are three different ways to employ the high biofidelity head models [25, 26, 29, 96, 97, 132, 140, 149, 150] for helmet protection, which are presented as follows. (i) The helmeted headform kinematics acquired from experimental tests [19, 20, 22] can be applied to the high biofidelity head models to evaluate the tissue-level injury predictors and then to assess the performance of helmet protection [132, 149]. For example, both Yu et al., [149] and Abayazid et al., [132] applied experimental headform kinematics to the ICFEHM to assess helmet protection

against the tissue-level injury predictors. (ii) To numerically replicate helmet protection under more different impact scenarios, the FE models of the helmets are positioned on the simplified head models (e.g. Hybrid III head model [151]) to obtain head kinematics under the assumed impact, then the head kinematics are used as input to the high biofidelity head models to measure the tissue-level injury predictors [26, 96, 150]. For example, Meng et al., [96] employed the Hybrid III head-helmet coupled model to obtain head kinematics, and then input these acquired kinematics to the KTHFEHM to compare the biomechanical differences of helmeted head under free fall and guide fall drop impacts. (iii) The high biofidelity head model can be directly coupled with the helmet model to replicate a more realistic helmeted head impact scenario, and the protection performance of the helmet can be directly assessed using the high biofidelity head-helmet coupled model [25, 29, 97, 140]. In this regard, as shown in Figure 2.14, Tinard et al., [25] coupled the SUFEHM with a composite helmet model to improve helmet design with regard to the tissue-level injury predictors. Xiao et al., [97] developed the GHBMC head-helmet coupled model to predict the head tissue-level responses of motorcyclist during impact against front end of vehicle.
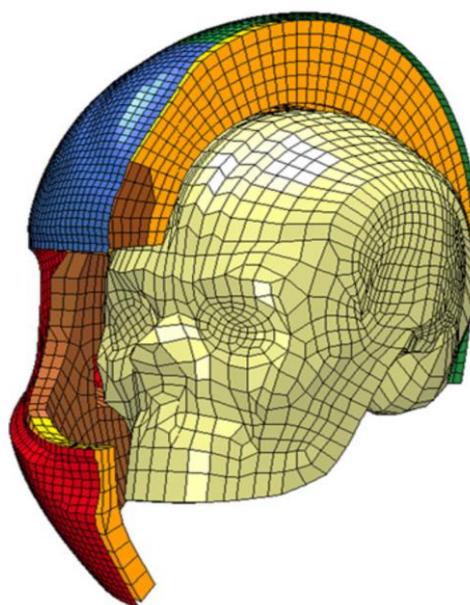
Figure 2.14. Illustration of helmeted SUFEHM coupled model [25]

In general, the first and second above-mentioned methods can save the costs of computational time and resources, due to the high biofidelity head models employed without coupling the helmet; whereas the more realistic helmeted head impact scenarios cannot be replicated. In contrast, the high biofidelity head-helmet coupled modelling method can directly characterise the helmeted head impact responses and assess the helmet protection performance; however, the high biofidelity head-helmet modelling method demands more computational costs for the impact simulations.

2.2.4 Head-helmet coupled modelling for helmet optimisation

An improvement of helmet design usually involves different geometrical designs and material selections [12, 35, 42, 152-154], which are under the imposed constraints presented in different helmet standards [19, 20, 22]. In other words, the design of helmet protection can be influenced by many different factors, including the structural configurations and material parameters, e.g. density, Young's modulus and stiffness of the material, geometries of helmet parts, etc [152, 155-157]. Based on head-helmet coupled modelling, optimisation studies can be carried out to seek the optimal design of different factors for helmet protection [12, 26, 30, 31, 33, 36].

Regarding helmet optimisation, Khosroshahi et al. [33] built a composite shell helmet FE model (Figure 2.15) coupled with a Hybrid III head-neck dummy to output neck axial force to find optimal configurations for the eight-ply composite chin bar. Three angles (i.e. θ_1, θ_2 and θ_3) with seven design candidates (i.e. 0, 15°, …, 90°) were selected in their study, and thus a total of 7^3 (= 343) possible ply lay-ups were simulated for the optimisation study. They also used the ISO headform-helmet coupled model to measure the head accelerations and *HIC* values for passing the requirements of the helmet standard ECE 22.05 [19]. Rueda et al. [36] developed a helmeted rigid headform model to optimise the energy-absorbing layered foam liner against head accelerations

and impact behaviours of liner foam; three impact velocities and three impact positions and 37 combinations of foam density configurations were considered in their study, indicating that a total of 3×3×37 (= 333) impact simulations were performed for this optimisation study. In comparison with the head kinematics obtained from the simplified head-helmet models for helmet optimisation [33, 36], a more reliable helmet optimisation can be performed against advanced tissue-level predictors (Section 2.1.4.2), which can be evaluated using the high biofidelity head-helmet models. However, to the author's knowledge, only Willinger's group [30, 31] used the high-fidelity ULPFEHM fitted with the helmet model to find the optimal parameters for helmet design, and they conducted 16 simulations to optimise four different parameters, i.e. elastic limit and its Young's modulus of the liner foam, thickness and its Young's modulus of the helmet shell. It is evident that these 16 simulations cannot cover enough possible design space for the optimisation of four different parameters, and therefore, the obtained optimal configurations of the helmet may not represent the best designs.
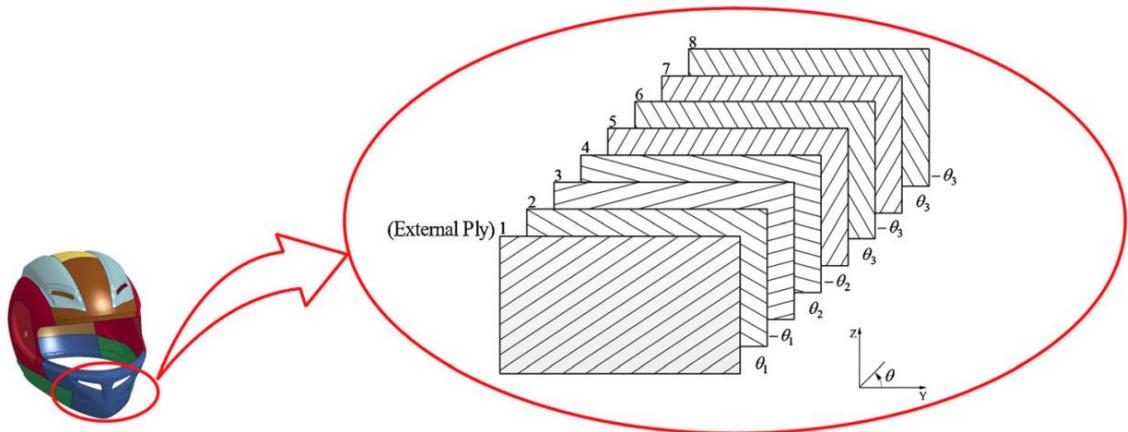
Figure 2.15. The chin bar ply lay-up in a composite shell motorcycle helmet [33]

The full factorial design (see Section 3.4.1.1 presented in **Chapter 3**), which considers all possible combinations of all design factors with their corresponding candidates, has been used in current helmet optimisation to ensure the reliability of the optimal result [33, 36]. As such, a great number of simulations need to be performed by using this full

factorial optimisation method, the computational costs can even increase in geometric order of magnitude when the numbers of design parameters and their possible candidates increase, which can limit the efficient development of helmet design. For example, three individual angles were considered for the optimisation of the eight composite plies (Figure 2.15), if the individual angles increased from three to four, the possible simulations can significantly increase from 7^3 (= 343) to 7^4 (= 2,401). Thus, it is significant to find an efficient method to improve the computational efficiency of helmet optimisation, which can help to obtain more benefits from the high biofidelity head-helmet models to improve the reliable and efficient helmet design

2.3　Advanced impact-attenuating materials for the helmet

As mentioned in Section 1.2 and illustrated in Figure 2.16, the protection performance of a helmet mostly depends on the basic components of an impact-absorbing inner liner and stiff outer shell [12, 158]. Thus, continuous efforts have been paid to the potential advanced impact-attenuating materials for the improvement of the inner liner and outer shell in order to enhance helmet protection to minimize head injury during impact accidents [12, 28, 33, 159]. This section describes two typical potential advanced impact-attenuating materials, i.e. functionally graded foam (FGF) materials and fibre reinforced plastics (FRP) composites, for the helmet inner liner and outer shell, respectively.

Outer shell   Inner liner
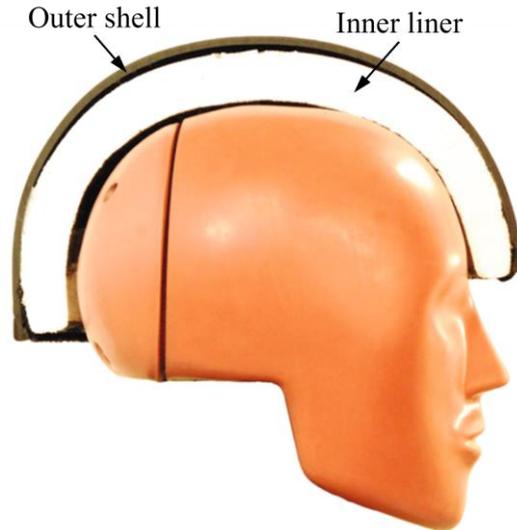
Figure 2.16. Motorcycle helmet inner liner and outer shell (modified from [158])

2.3.1   Helmet inner liner

The helmet inner liner is responsible for absorbing most collision kinetic energy and dispersing the load over a larger area of the head to avoid stress concentration during impact accidents [12]. From the aspect of impact energy dissipation, the inner liner is the most important component of a helmet, which is of the greatest potential to increase the energy absorption capability through an optimised material design, so that the protection performance of the helmet can be enhanced, and thus, the impact energy transmitted to the head can be mitigated to minimize head injury occurrence [12].

In general, the helmet liner is made of a relatively thick polymer foam, e.g. expanded polystyrene (EPS) foam or expanded polypropylene (EPP) foam, due to their lightweight and energy-absorbing capacity of multidirectional impact resistance [43]. As shown in Figure 2.17, the typical compressive stress-strain responses can be characterised by three distinctive sequential regimes, including (i) linear elastic regime wherein stress increases linearly with strain until reaching a local maximum, (ii) plateau regime wherein stress is relatively constant over a large range of strain, and (iii) densification regime wherein stress increases rapidly with strain [160]. The energy absorption per unit

volume of foam material can be calculated by integrating the stress-strain curve.
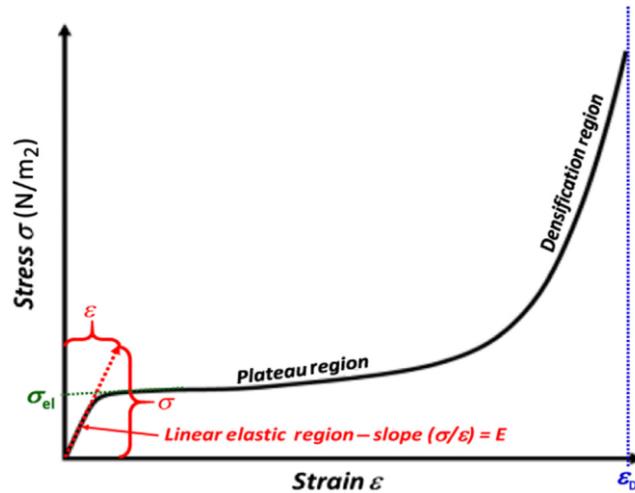
Figure 2.17. Typical compressive stress-strain curve for the polymeric foam [160]

According to the reported literature [12, 161-164], the foam density of the helmet liner usually ranges from 30 kg/m^3 to 90 kg/m^3, which indicates that the impact-absorbing capacity of helmet liners can be regulated by varying the density of liner foam. The compressive stress-strain responses of EPS foams with different densities are compared in Figure 2.18, it is found that the higher density can lead to a higher crushing load to compress the foam material [165], which means that the maximum energy absorption of liner foam can be achieved by using the maximum foam density. However, the excessively high foam density may result in too high crushing stress at the plateau regime and further lead to the excessively high impact load transmitted to the head [152]. Also, the maximum foam density is limited by the weight requirement of helmet design [19]. In contrast, if the foam density is too low, the impact energy cannot be absorbed completely at the plateau regime, and thus the densification regime could be reached to produce a rapid rise of crushing stress, which can lead to excessively high impact load transmitted to the head [152, 165]. As such, a reasonably good selection of foam density for the helmet liner should be able to dissipate the most impact energy and keep the impact load transmitted to the head at a safer level.
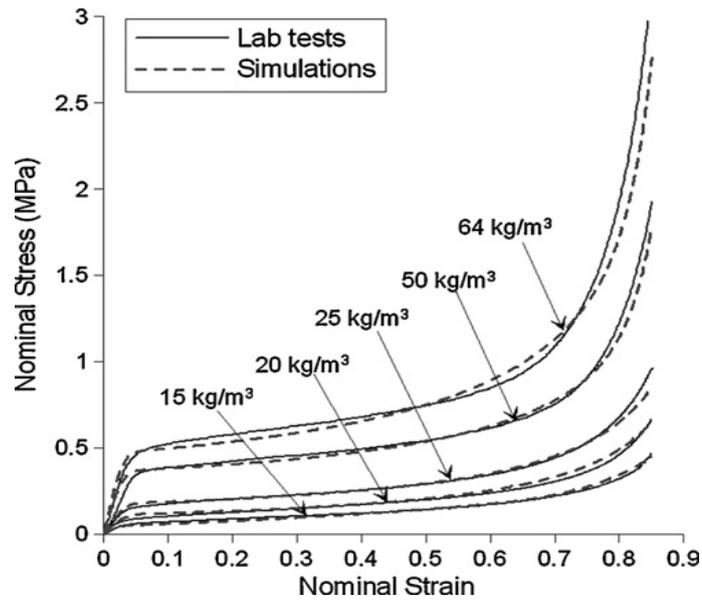
Figure 2.18. Experimental and numerical compressive stress-strain curves for EPS foams with different densities [165]

Natural bio-inspired materials and structures, as shown in Figure 2.19, which have evolved for millions of years to achieve excellent and efficient mechanical properties, can inspire the development of protective equipment [166, 167]. Inspired by natural materials and structures, e.g. bamboo [168], pomelo [169] and palm [170], for energy absorption applications, the concept of functionally graded foam (FGF) materials with the density-gradient design has been introduced [171]. Due to the high similarity between impact protections on pomelo and helmeted head, the pomelo was set as an example here. As illustrated in Figure 2.20, the pomelo with a weight of up to 6 kg and from a height of 15 m can acquire considerable impact energy when falling from the tree to the ground [172]. As shown in Figure 2.20(c), a thick foam-like pomelo peel, whose structural density changes from the flavedo towards the pulp, can act as a functional shock-absorbing layer to dissipate considerable kinetic energy during impact, thus the inner fruit and its seeds are protected from suffering mechanical damage [173]. Thielen et al. [173, 174] experimentally revealed the excellent impact resistance of pomelo peel is due to the density gradient for the foam-like structure. In addition, many other studies

[175-178] demonstrated that FGF materials can be employed to improve the impact-attenuating capability of protective structures. It implies that FGF materials with varying foam density could be a potential advanced impact-absorbing material for the improvement of helmet protection. In other words, the helmet liner made of FGF materials may offer better cushion and protective functions than the conventional design of helmet liner [27]. Furthermore, the application of FGF materials can also provide more designable space to find a possible better solution to compensate the excessive stiffness of composite shells, as analysed in the following Section 2.3.2.
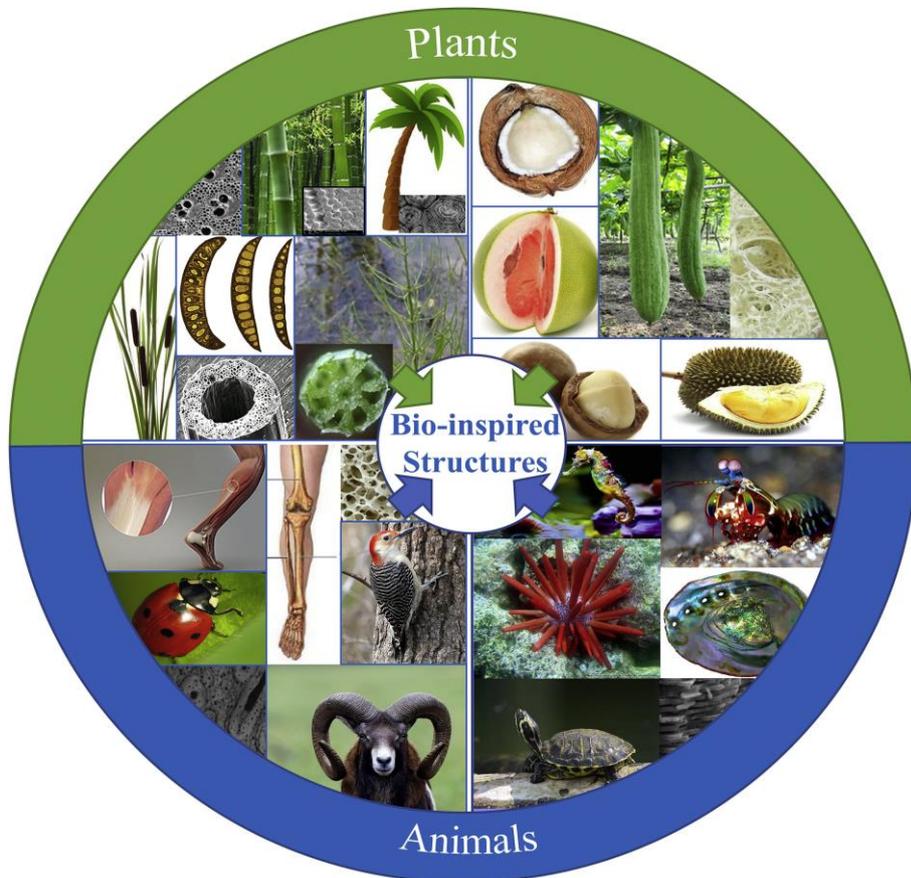
Figure 2.19. Biological materials/structures can inspire the design of novel bio-inspired materials/structures with excellent energy-absorbing capacities [166]
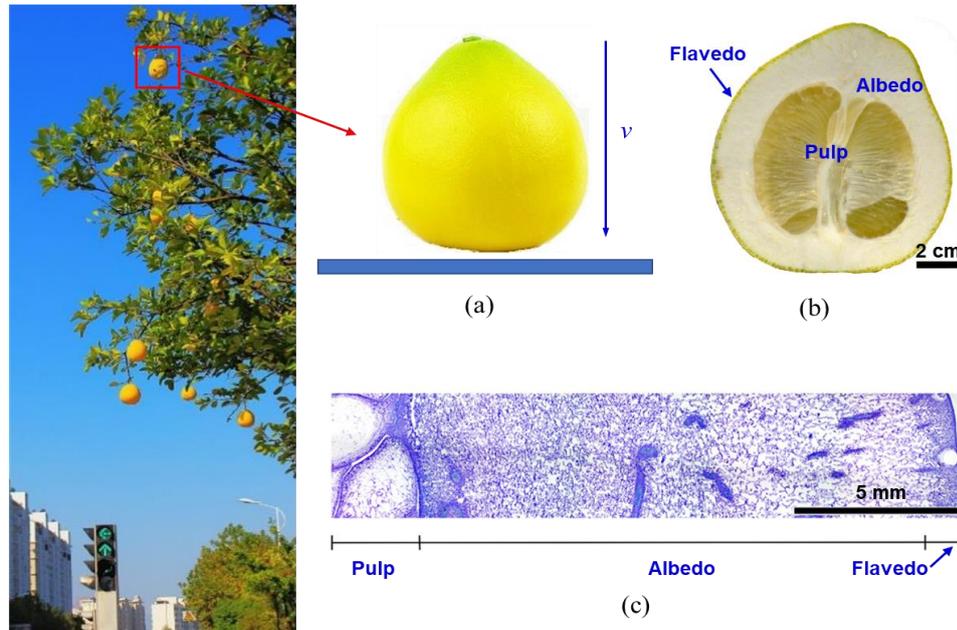
Figure 2.20. Illustration of impact scenarios, (a) pomelo drops from the tree to impact the ground, (b) cross-sectional view of a pomelo, (c) thin-section of a pomelo peel sample [173]

Inspired by the significant potential of FGF materials to improve the impact-attenuating capability of foam structures, Cui et al. [165] investigated the energy-absorbing capacity of polymeric FGF made from EPS foam using numerical modelling, based on which they further [27] introduced this polymeric FGF to an equestrian helmet to improve the protection performance of the helmet. FGF materials have also been widely investigated and introduced to many other impact applications due to their better energy-absorbing capacities than their corresponding uniform density foam (UDF) counterparts [173, 174, 176-183]. For example, Sun et al. [176] numerically studied the aluminium FGF filler to fill thin-walled structures and concluded that the aluminium FGF filler is superior to the UDF counterpart in axial crushing resistance of foam-filled structures. Fang et al. [178] further proved that FGF filler can significantly enhance the lateral crashworthiness of aluminium foam-filled structures in comparison with the conventional UDF filler. Furthermore, based on the computational models of FGF materials, Zhang et al. [180] conducted an optimisation study to obtain the most appropriate design of metallic FGF under ball impacts.

As mentioned above, FGF materials can be characterised and designed using the FE modelling method [165, 173, 174, 176-183]. As shown in Figure 2.21, a computational model of FGF need to be regarded and modelled as a combination of numerous discretely independent UDF layers with different foam densities [184]. To establish the FGF FE model, a great number of material properties should be determined in advance to define the numerous UDF layers with different foam densities [176, 184]. It indicates that considerable time is required for the development of the FGF FE model, which can limit the efficient design and application of FGF materials. In addition, the experimental method on FGF materials for helmet design is also expensive, inflexible and time-consuming [185]. Therefore, to improve the efficient analysis and selection of polymeric FGF materials for helmet design, it is necessary to develop an analytical method that can characterise the mechanical behaviours of polymeric FGF materials.
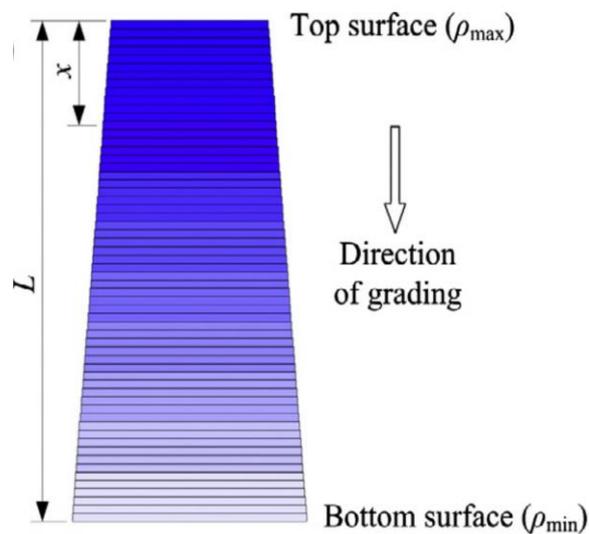
Figure 2.21. Schematic of density grading patterns for the tapered FGF [184]

Regarding the analytical studies on foam materials, Gibson and Ashby [186] systematically explained the deformation mechanisms of UDF under compression, they analytically predicted the compressive responses of UDF using the simplified tri-linear responses, including a linearly elastic phase, a constant plateau phase and a stiff

densification phase; however, the nonlinear responses of foam materials cannot be described. Schraad and Harlow [187] developed a stochastic analytical model to describe the nonlinear compressive responses of disordered foam materials, however, this model is only useful for UDF. Kiernan and Gilchrist [188] further proposed a constitutive model to define the large strain compressive responses of polymeric foam, which can be used for the FE model development of polymeric FGF material by defining numerous discretely independent UDF layers (Figure 2.21); however, the proposed constitutive model still cannot be used to analytically characterise polymeric FGF materials. As such, there is still a lack of efficient constitutive models available for polymeric FGF materials.

2.3.2   Helmet outer shell

The first purpose of the stiff outer shell is to prevent the helmet from penetrating to avoid direct contact between the impactor and head which can lead to severe head injury [13]. The outer shell is also designed to spread the impact over a larger area of the helmet surface for the extensive deformation of inner liner foam to dissipate more impact kinematic energy transmitted to a human head [14]. Furthermore, the helmet shell can initially absorb the impact energy with 10% ~ 34% of the total impact energy could be dissipated [12].

Based on these above-mentioned functions of the helmet shell, the hard helmet shell is generally made from thermoplastics, like acrylonitrile-butadiene-styrene (ABS) and polycarbonate (PC), with a typically 3 ~ 5 mm thickness [43]. Recently, the fibre reinforced plastics composites, such as glass fibre reinforced plastics (GFRP), carbon fibre reinforced plastics (CFRP) and Kevlar fibre reinforced plastics (KFRP), which are made of both high-performance fibres and matrix, have become feasible solutions for helmet design improvement, due to their lightweight and excellent crashworthy characteristics compared to conventional engineering plastics [189, 190]. At present, the

helmet outer shell made from FRP composites is gradually replacing the thermoplastic ones and has attracted more and more related research [18, 33, 154, 159, 191-193]. The differences between the thermoplastics and FRP composites for the design of helmet outer shells are summarized in Table 2.1.

Table 2.1. Comparisons between thermoplastics and composites for the helmet shell

Material	Thermoplastics, such as PC and ABS; composites, such as GFRP, CFRP, and KFPR [194].
Property	Thermoplastics show isotropic material behaviours[195], while FRP composites are anisotropic materials [196].
Stiffness	The stiffness of the FRP composite shell is higher than a thermoplastics counterparts [197], which indicates that the stiffer FRP shell can spread impact through minor deformation, where the energy is predominantly absorbed by the helmet liner [198].
Energy absorption	Thermoplastic shells absorb impact energy by both structural bulking and plastic deformation [199], while FRP composite shells may dissipate more impact energy through complex damage mechanisms like fibre breakage, matrix cracking and delamination [200].
Low-energy impact	Thermoplastic shells of more effective protection during a low-energy impact, due to their lower stiffness are more likely to cause a large deformation to dissipate impact energy [157].
High-energy impact	FRP composite shells can provide substantial protection in a high-energy impact, their complex damage mechanisms can help in absorbing a large amount of impact energy [198].
Fracture and rebound	Thermoplastic shells are more likely to fracture and rebound than FRP counterparts, which results in less protectability of helmet [194]
Design	The softer thermoplastic shells are often designed in combination with the stiffer and high-density liner foams, due to the compensation of relatively poor energy-absorbing capacity, whereas the softer low-density liner foams are recommended for the stiffer FRP composite shells [201].
Cost	Thermoplastic shells are cheaper than composite counterparts [154]; thus, composites are more likely to be used for the most advanced helmets [199].

In general, FRP composite shells are stiffer than their thermoplastic counterparts [197]. In high-energy impact accidents, composite shells can absorb more impact energy through different damage mechanisms, e.g. fibre breakage, matrix cracking and delamination [200]. However, at low-energy impacts, little amount of energy is absorbed by composites because the high stiffness prevents delamination failure which is the main trigger of the energy absorption mechanisms of composite shells, leading to a higher impact load transmitted to the head [164]. In contrast, the softer thermoplastic shells can show better protective characteristics at low-energy impact [12]. To overcome the main drawback of FRP composite shells at low-energy impact and promote their applications in helmet design, low-density softer foams are recommended for helmet liners to combine the stiffer composite shells [199]. However, the uniform low-density foams may reduce the impact-attenuating capacity of the helmet liner [43], and the combination of composite shells and low-density liner foams may not improve helmet protection under certain circumstances. As described in Section 2.3.1, the polymeric FGF materials made from density-gradient polymer foam, could be a possibly better choice for helmet liners to compensate excessive stiffness of the composite shells without the reduction of impact-attenuating capacity of the helmet liner. As such, the significant need for the analytical method to analyse the compressive characteristics of polymeric FGF materials is highlighted again for the efficient design of helmet design.

2.4 Conclusions

In this chapter, the literature on the impact biomechanics of the human head, finite element method for head injury prevention and potential advanced impact-attenuating materials for helmet design are reviewed. It is shown that several research gaps exist in the current studies/methodologies that can limit reliable and efficient helmet design.

Firstly, helmet design can be improved from the structural optimisation aspect. Most helmet optimisation has been implemented based on the head kinematics measured by the simplified head-helmet models, whereas the advanced tissue-level injury predictors evaluated by the high biofidelity head-helmet models have been seldom employed, which limits the reliable design of the helmet. Also, the full factorial optimisation used in the current helmet design demands significant computational resources, which also limits the efficient improvement of helmet design. Thus, there is an imminent need to find an efficient optimisation method based on the high biofidelity head-helmet model to improve the reliable and efficient helmet design.

Secondly, helmet protection can be improved from the material level. Polymeric FGF could be a potential advanced energy-attenuating material to improve the design of the helmet liners and compensate excessive stiffness of composite helmet shells. It not only inherits the advantages of UDF but also increases design parameters. However, regarding the design of FGF materials, the numerical method for FGF materials demands considerable time for the FE model development, whereas the experimental method is not an efficient choice too. It highlights a significant need to find a rapid and effective analytical method to characterise the compressive responses of polymeric FGF to support efficient material analysis and selection for helmet design.

Thirdly, helmet design can be improved by a better understanding of head impact response and its injury mechanism. As mentioned in Section 2.2.3, the helmeted head accelerations obtained from the experiments/simulations can be applied to the high biofidelity head models (without coupling the helmet) to efficiently investigate helmet design in terms of head tissue-level injury predictors. In this regard, as mentioned in Section 2.2.2, to improve head impact protection with a deeper understanding of head injury mechanisms, the high biofidelity head models have been widely used to reveal the

influences of each acceleration loading configuration (e.g. loading curve shapes, peak magnitude and impact duration) on head responses. However, the interactive effects of peak magnitude and impact duration with different loading curve shapes on the head responses have yet to be revealed clearly.

In summary, to provide the methodologies for the reliable and efficient design of helmet against head injury, all these above-mentioned research aspects will be covered in this thesis and presented in the following chapters.

3 Head-Helmet Coupled Modelling with Optimisation

Publication Information

---

[*]Corresponding author.

3.1 Introduction

With the rapid development of computational mechanics, interactive head-helmet coupled modelling has been widely used to support helmet design against head responses [25, 26, 29, 96, 97, 140, 150]. Since the helmet design can be affected by many different design factors, such as structural configurations and material parameters [12, 35, 42, 152-154] as well as the requirements prescribed in helmet standards [19, 20, 22], helmet optimisation based on head-helmet modelling has been carried out to find the optimal design of different factors to improve helmet protection [12, 26, 30, 31, 33, 36]. The head kinematics measured by the simplified head-helmet models have been employed in most helmet optimisation studies [33, 36]. However, the more fundamental and advanced tissue-level injury predictors (Section 2.1.4.2) obtained by the high biofidelity head-helmet model have seldom been considered in helmet optimisation [30, 31], which can limit the reliable design of the helmet. In addition, the full factorial design used in previous helmet optimisation by considering all possible combinations of helmet design demands remarkable computational costs, which significantly limits the efficient helmet design [33]. As such, to improve the reliable and efficient helmet design, it is necessary to find a more efficient helmet optimisation method based on the high biofidelity head-helmet modelling.

To demonstrate the efficient optimisation method for helmet design, a honeycomb-filled motorcycle helmet design, in which an aluminium honeycomb was used to reinforce the helmet liner, was selected in this chapter as an example. This is because the lightweight honeycomb is of excellent crush resistance capacity and can also provide many designable parameters, e.g. side length and wall thickness of the honeycomb cell, for helmet design optimisation [202-206]. Although the honeycomb was reported in some previous studies [35, 42, 207] to improve the protection performance of novel helmet

design, only the head kinematics and helmet structural behaviours were measured to assess the novel helmet protection, whereas the advanced tissue-level head injury predictors were not evaluated. It highlights again the significance of high biofidelity head-helmet modelling for the novel helmet design.

To fill the above research gaps, this chapter is aimed to propose an efficient helmet optimisation method to improve the honeycomb-filled helmet design by using a representative high biofidelity head-helmet model. First, a full-face motorcycle helmet was reconstructed to develop a typical helmet model; then, standard drop tests were performed to validate the helmet model, which is coupled with a Hybrid III head model, based on the acceleration histories transmitted to the head. A high biofidelity THUMS head-helmet model was further established to explore the tissue-level responses of the helmeted head during impacts. Then, the honeycomb model was developed and validated by the out-of-plane compression tests. Based upon the above validated FE models, a honeycomb-filled helmet design was proposed together with a parametric study for the understanding of the effects of honeycomb filler on helmet impact protection. Finally, an orthogonal array design combined with the discrete optimisation method was introduced to the helmeted head models to efficiently seek the optimal design for the honeycomb-filled helmet.

3.2 Finite element models

There are stringent regulations on the experiments on cadavers due to ethical considerations. Therefore, it is much more difficult to measure the internal responses of the head by experimental method. In this regard, the FE method can offer an alternative option to the experimental method for the study of the head kinematics and tissue-level responses subjected to external loads. In this section, the FE models, such as the Hybrid

III head model and high biofidelity THUMS head model, motorcycle helmet model and honeycomb model, were applied to investigate the helmeted head responses when subjected to impact loadings.

3.2.1 Head models

3.2.1.1 Hybrid III head model

According to the Standard ECE 22.05 for the motorcycle helmet [19], a metal headform should be equipped with the helmet for the measurement of the acceleration at the centre of gravity of the headform during the drop test, which is a way to study the acceleration transmitted to the head to assess the helmet protection performance. Figure 3.1 shows the Hybrid III 50th percentile male head model [151], which was adopted here for simulating the drop test of the helmeted headform. An acceleration sensor was set at the gravity centre of this head model to output the acceleration-time history. A rigid material model *MAT_20: RIGID available in commercial FE code LS-DYNA was adopted to simulate the accelerometer, while the skin and skull were modelled using visco-elastic material model *MAT_6: VISCO-ELASTIC and elastic material model *MAT_1: ELASTIC, respectively. The mass of the Hybrid III head model is 4.50 kg, and 21,908 elements were used in this model.

<div align="center">(a)   (b)</div>
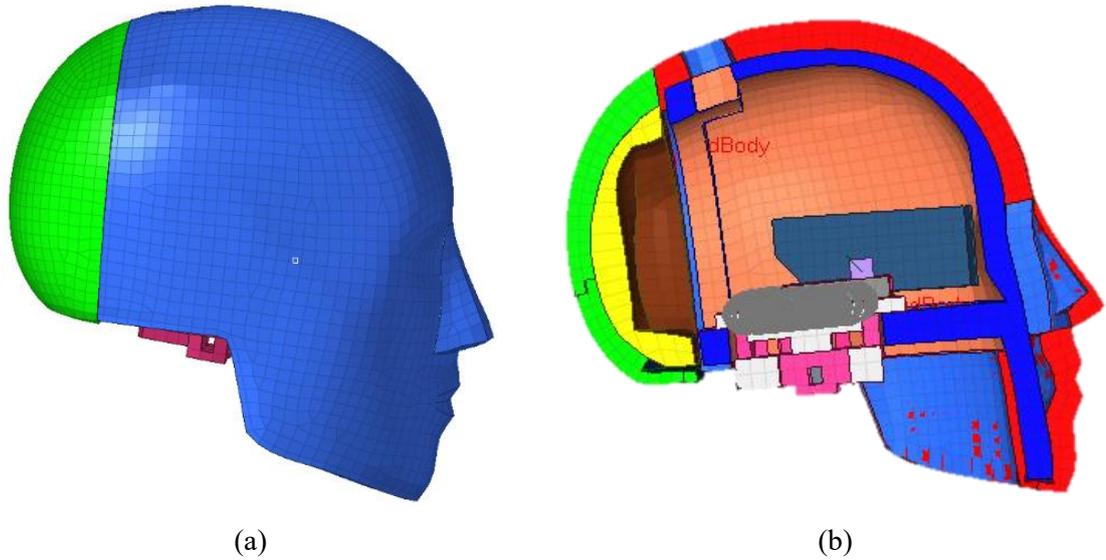
Figure 3.1. The Hybrid III head model, (a) overview of the head model, (b) sectional view of the head model

3.2.1.2 *THUMS head model*

As shown in Figure 3.2, the THUMS 50th percentile male head model (Version 3) was used in this chapter for investigating the tissue-level responses of the head during impacts. The THUMS model was developed by researchers in the Toyota Motor Corporation and validated against a wide range of head impact testing data, such as brain pressure, acceleration of the brain and relative skull-brain motion [121, 208]. The main anatomical features of the head have been considered in the model, such as skin, skull, cerebrum, cerebellum, brainstem, falx, cerebrospinal fluid, etc [208]. The skull was modelled by the elastic-plastic material model *MAT_24: PIECEWISE_LINEAR_PLASTICITY in LS-DYNA, and the brain was modelled using a hypoelastic constitutive model *MAT_77: OGDEN_RUBBER. In total, 49,700 elements were used to build this head model, and the mass of the model is 4.39 kg. As mentioned above, this validated high biofidelity THUMS head model is appropriate for predicting the tissue-level responses of the head during impact scenarios.
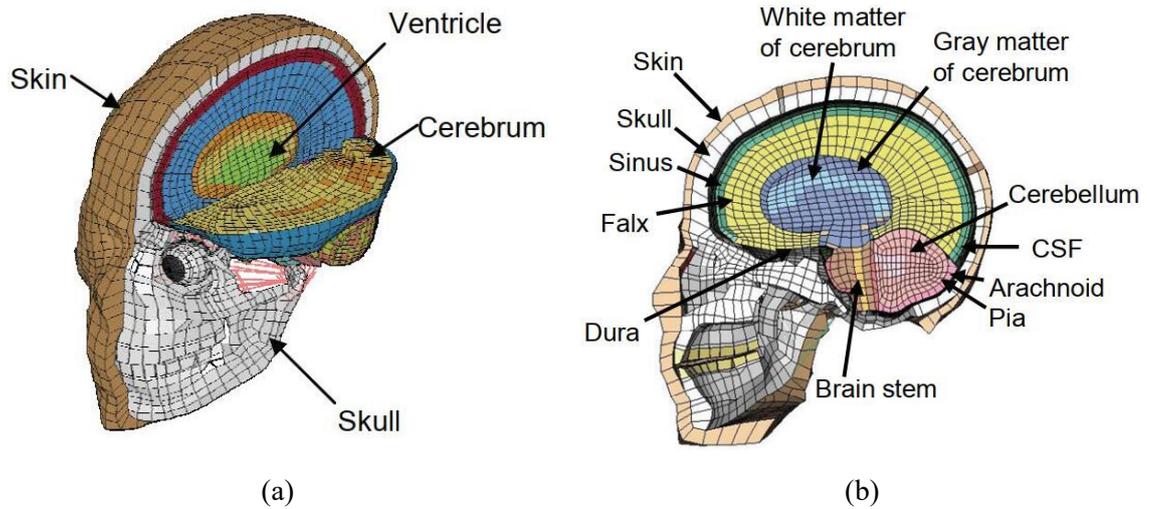
Figure 3.2. The THUMS head model, (a) oblique view of the head model, (b) lateral view of the head model [208]

3.2.2   Helmet model

3.2.2.1   *Development of helmet model*

A representative full-face motorcycle helmet AGV-K3, which meets the requirement of Standard ECE 22.05 [19], was selected here as a reference for the development of the helmet model. The details for the helmet model development are illustrated in Figure 3.3. The selected helmet was first scanned using GOM non-contact optical 3D scanner, as shown in Figure 3.3(b). It should be noted that only the outer shell and inner liner of the helmet were scanned, whereas the face shield and comfort pads of the helmet were not considered here due to their negligible effect on the energy absorption of the helmet during impact [12]. After the geometric configuration of the helmet was performed in Figure 3.3(c), the helmet geometry was imported to the commercial FE software HYPERMESH to build the helmet model through a series of procedures, such as meshing elements, assigning material properties and defining boundary conditions, as shown in Figure 3.3(d).
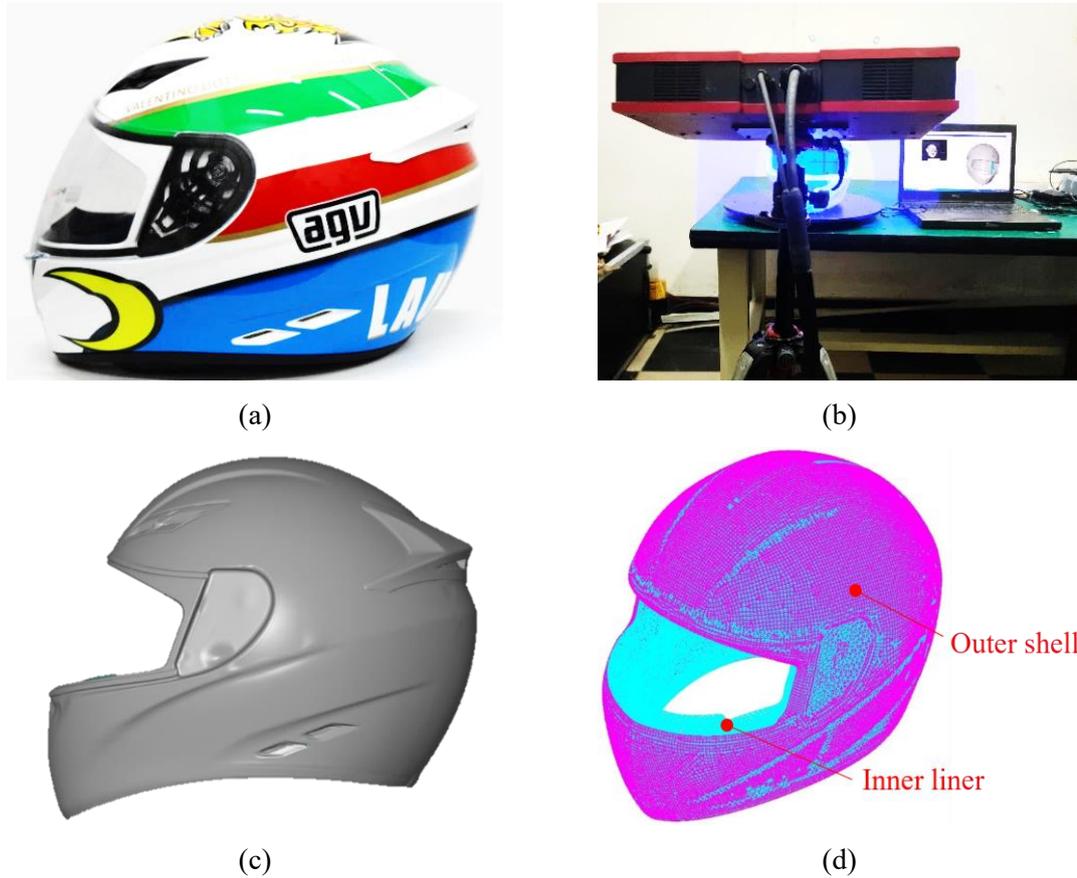
Figure 3.3. Details for the helmet model development, (a) motorcycle helmet, (b) 3D scanning by the GOM scanner, (c) geometric reconstruction of helmet, (d) overview of helmet model

The helmet outer shell was made of ABS with a thickness of 4 mm and the EPS liner foam with a variable thickness ranging from 6 mm to 45 mm. An elastoplastic material model *MAT_3: PLASTIC_KINEMATIC and foam material model *MAT_63: CRUSHABLE_FOAM in LS-DYNA were adopted for the outer shell and the inner liner of the helmet, respectively [97]. Based on the mesh convergence study, 24,595 full integrated Belytschko-Tsay shell elements with a mesh size of 4 mm were applied for the outer shell, and 360,387 solid elements with one-point integration were used for the inner liner with an average size of 4 mm. The total mass of this helmet model is 1.67 kg. Because the bolt joints and adhesive bonds were used to connect the outer shell and inner liner, a tied interface *CONTACT_TIE_NODES_TO_SURFACE was selected to simulate the interactions of the outer shell and inner liner; both the static and dynamic

frictional coefficients were set to be 0.3 on the interface [209]. The material properties of ABS shell and EPS foam are listed in Table 3.1 with their original sources, the nominal compressive stress-strain curve for EPS foam is presented in Figure 3.4.

Table 3.1. Summary of material properties

Material	Density (kg/m^3)	Young's modulus (GPa)	Poisson's ratio	Yield stress (MPa)
ABS shell [210]	1200	2	0.37	34.3
EPS foam [27]	80	0.019	0.01	0.58
Anvil/platen [211]	7850	210	0.33	/
AA3003 [203]	2730	69	0.33	145
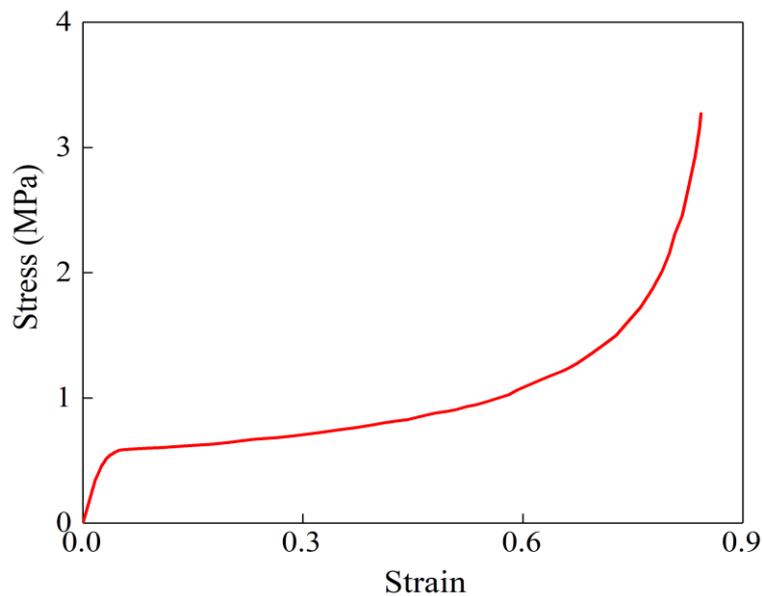
Figure 3.4. Nominal uniaxial compressive stress-strain curve for EPS foam with the density of 80 kg/m^3 (redrawn from [27])

3.2.2.2   *Validation of the helmet model*

As shown in Figure 3.5(a), the standard free drop tests on the front impact position, i.e. Point B, of the helmet, were carried out for validating the accuracy of the helmet model. Based on the Standard ECE 22.05 [19], the helmet fitted with a metal headform released

from a drop height of 2.9 m, which can lead to an initial velocity of 7.5 m/s for the helmet crash to the rigid flat anvil, as illustrated in Figure 3.5(b). Three identical drop impact tests for the helmet were performed to ensure the repeatability of experimental results. An accelerometer PCB-356B21 was instrumented at the centre of gravity of the headform to record the acceleration-time history during the test. The measured acceleration data were filtered with a CFC-1000 low-pass filter, which has a pass frequency range from 0.1 Hz to 1000 Hz, in accordance with Standard SAE J211 [212]. As shown in Figure 3.5(c), a simulation of the drop test was conducted using the helmet model coupled with the Hybrid III head model where both the initial impact velocity of 7.5 m/s and gravity acceleration were set as the impact conditions for the coupled Hybrid III head-helmet model. The fixed flat anvil was modelled using a rigid material model *MAT_20: RIGID, whose material properties are summarized in Table 3.1. Both experimental and numerical results were presented in Figure 3.5(d)-(f). The numerical acceleration-time histories are in good agreement with the experimental results, as shown in Figure 3.5(d). It should be noted that Standard ECE 22.05 [19] specified two types of drop tests, i.e. flat anvil impact test and kerbstone impact test. Meanwhile, Standard ECE 22.05 recommends five impact positions for a complete assessment of helmet protection performance. Although only flat anvil tests for the front impact position were considered in this study, the methodology developed is also applicable to other types of impact tests. Table 3.2 summarizes all peak acceleration and *HIC* values for three drop impact tests and their corresponding simulations. Based on the results in Table 3.2 and Figure 3.5, the helmet model is validated by the drop tests.

(a)

(b)

(c)

(d)

(e)

(f)
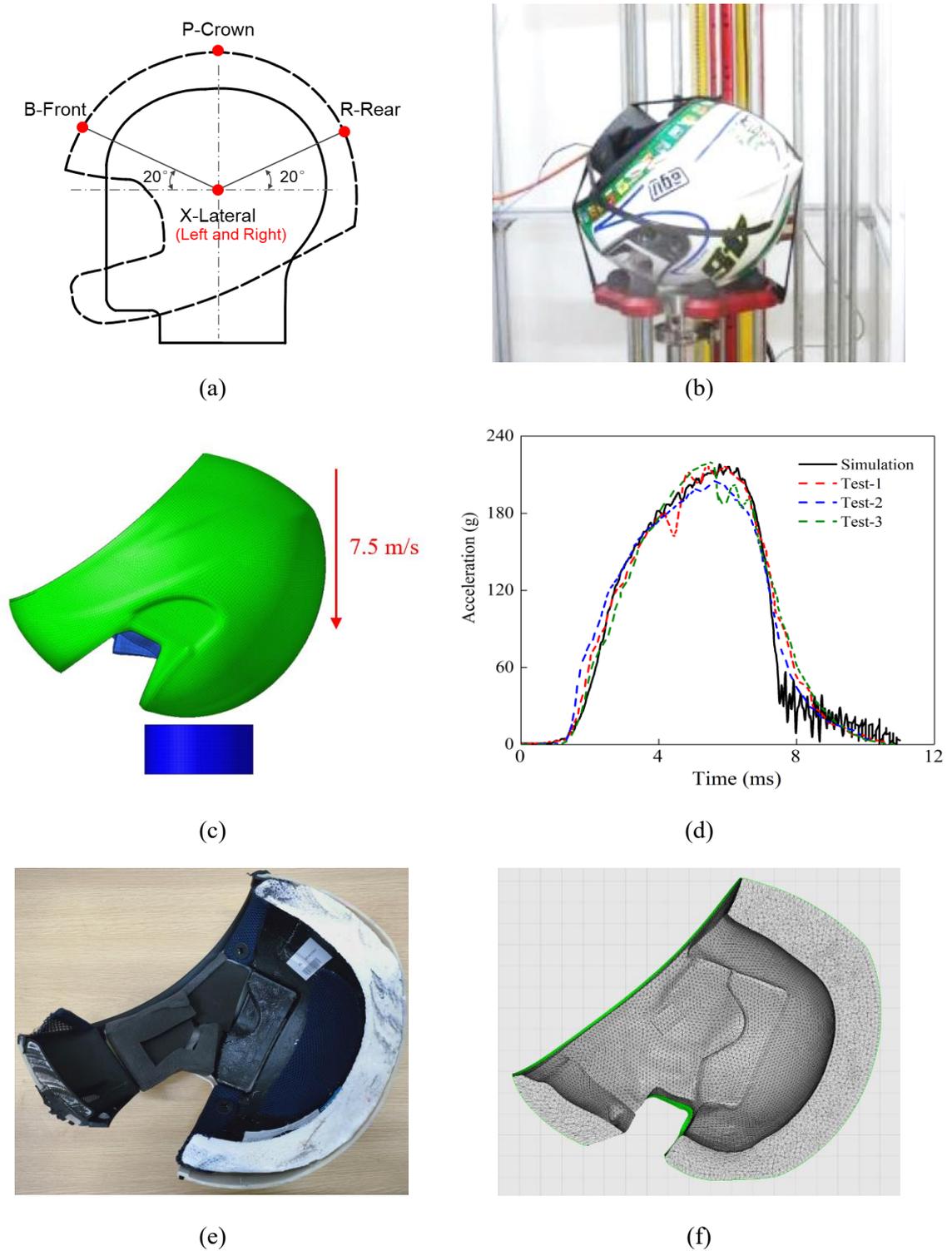
Figure 3.5. Experiments and simulation of drop impact test for the helmeted head, (a) impact points of helmet, (b) drop test for helmeted headform, (c) numerical simulation of drop test, (d) acceleration histories transmitted to the head measured in three tests described in Table 3.2, (e) final deformation of the helmet after drop test experiment, (f) final deformation of helmet model after drop test simulation

Table 3.2. Experimental and numerical results of the drop impact tests

	Peak acceleration (A_{max})	HIC value
Drop test-1	217.4 g	1990
Drop test-2	204.9 g	1882
Drop test-3	219.2 g	1955
Average of tests	213.8 g	1963
FE Simulation	215.1 g	1985
Standard deviation of tests	6.36	44.99

3.2.3 Honeycomb model

3.2.3.1 Development of the honeycomb model

A lightweight honeycomb made of aluminium alloy AA3003 was used to improve the energy-absorbing capacity offered by the inner liner to enhance helmet protection under impacts. As shown in Figure 3.6, a FE model of honeycomb column under out-of-plane compression was developed. The honeycomb was placed on the fixed rigid platen and loaded by a moving upper rigid platen. The final displacement was set as 40 mm. The honeycomb model has a structural configuration of length × width × depth = 78 mm × 77 mm × 50 mm and 14 × 15 cells. The cells are determined by the geometry of side length × wall thickness ($c \times t$ = 3.2 mm × 0.08 mm). The loading velocity of 400 mm/s used in the FE model was much higher than the loading rate of 4 mm/min in the experiment to largely increase the computational efficiency, which is acceptable because aluminium is insensitive to the strain-rate [169, 213-215]. Therefore, both strain-rate and inertia effects were negligible in the numerical simulation.
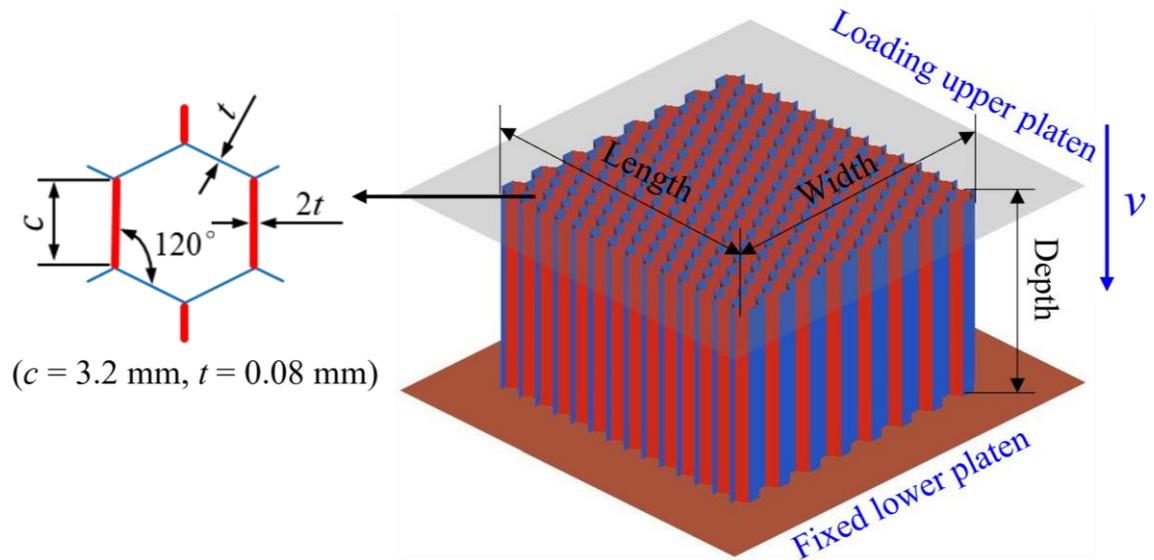
Figure 3.6. Honeycomb model subjected to out-of-plane compression

Based on the mesh convergence study, the Belytschko-Tsay shell elements with a mesh size of 0.5 mm were adopted to model the honeycomb, as shown in Figure 3.6. The 'AUTOMATIC_SINGLE_SURFACE' contact was used in the honeycomb model to avoid self-penetration during compression, and the static and dynamic frictional coefficients were set to be 0.3 [203] and 0.2 [216], respectively. An elastoplastic material model *MAT_3: PLASTIC_KINEMATIC in LS-DYNA was utilized to simulate the material characteristics of the honeycomb, and the rigid material model *MAT_20: RIGID was selected for the upper and lower platens. The mechanical properties of the aluminium honeycomb are summarized in Table 3.1, and the nominal tensile stress-strain curve for the AA3003 is presented in Figure 3.7 [203].
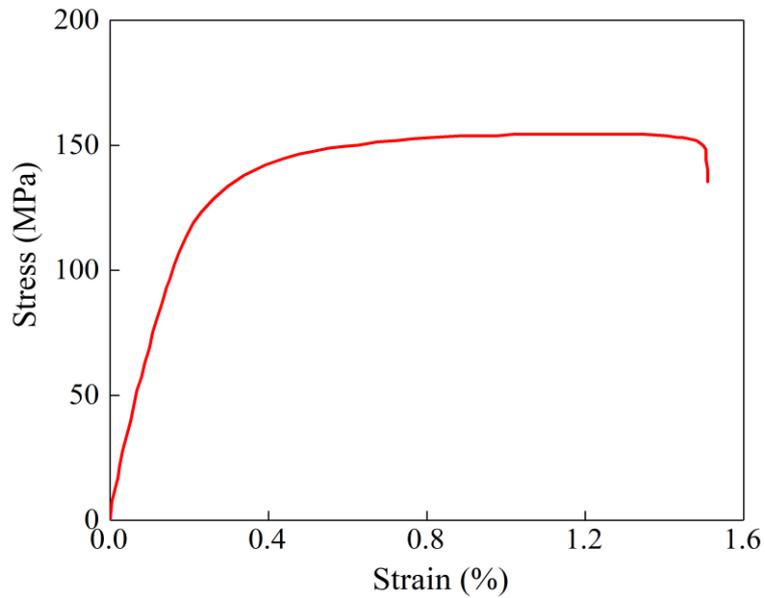
Figure 3.7. Nominal tensile stress-strain curve for the AA3003 (redrawn from [203])

3.2.3.2   *Validation of honeycomb model*

The honeycomb model was validated before it was introduced to the proposed helmet model. Aluminium honeycomb specimens under out-of-plane compression were carried out to validate the honeycomb model, as shown in Figure 3.8. Three identical honeycomb specimens, with the same geometrical configurations of length × width × depth = 78 mm × 77 mm × 50 mm and $c \times t$ = 3.2 mm × 0.08 mm, were tested to ensure the repeatability of experiments. These quasi-static tests were performed using the universal testing machine INSTRON 5985 with a loading capacity of 150 kN. The honeycomb specimens were compressed by the top platen at a constant crosshead speed of 4 mm/min and the loading displacement was set to be 40 mm.

Three force-displacement curves for the aluminium honeycomb specimens subjected to out-of-plane compression tests are presented in Figure 3.9 and compared with the corresponding numerical results predicted by the honeycomb model. As compared in Figure 3.9(a), three experimental force-displacement curves almost coincided with each other, indicating the excellent repeatability of the honeycomb specimen under

out-of-plane compression. In comparison with the numerical simulation, both the overall tendency of the force-displacement curve and the deformation pattern of the honeycomb model show very good agreement with the experimental results, demonstrating the accuracy of the honeycomb model.
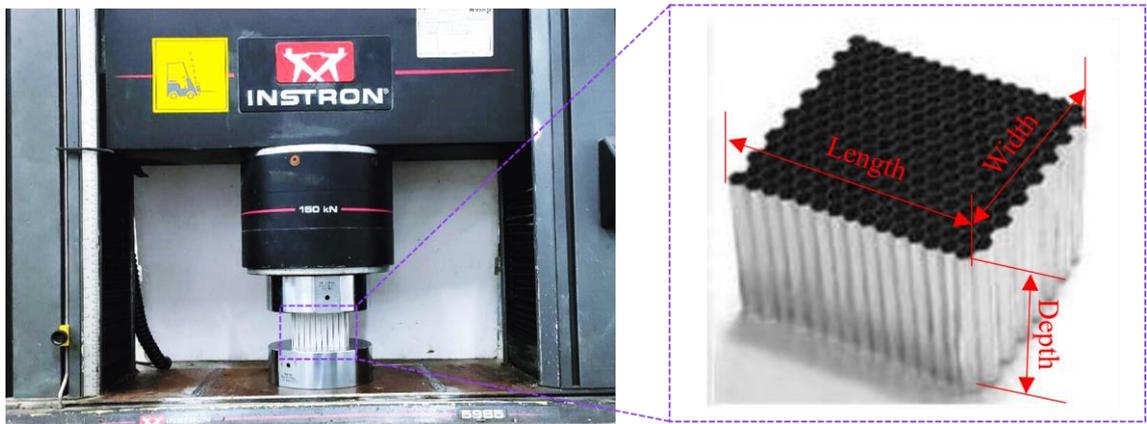
Figure 3.8. Aluminium honeycomb specimen under out-of-plane compression

(a)   (b)
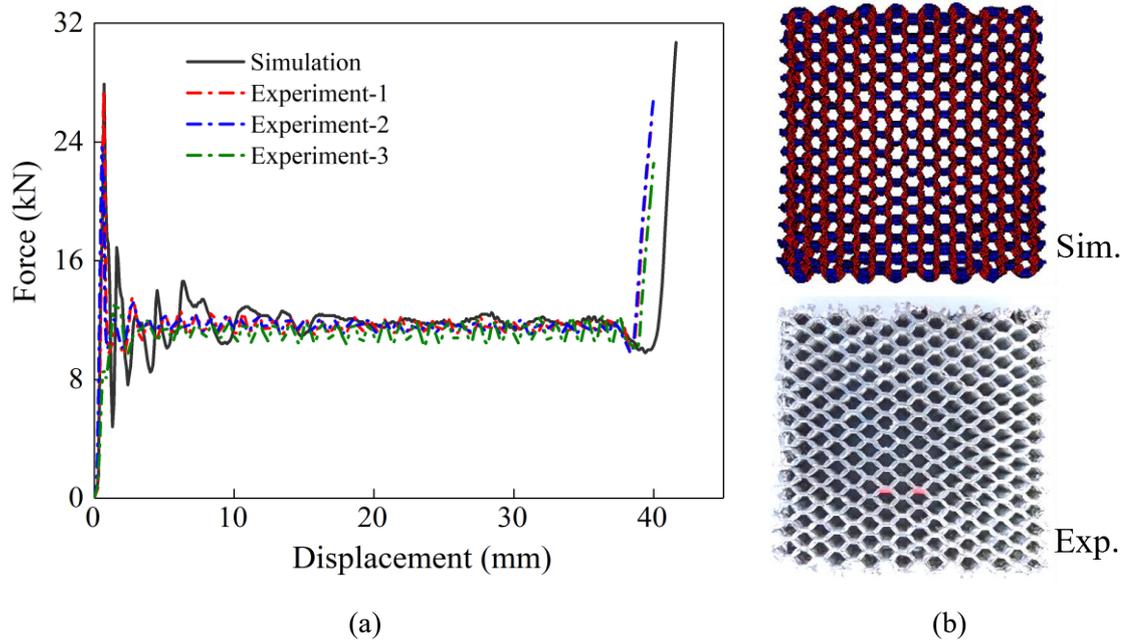
Figure 3.9. Numerical and experimental results for the honeycomb specimens under out-of-plane compression, (a) force-displacement curves, (b) deformation of honeycomb

3.3   Numerical simulation results

3.3.1   Honeycomb-filled helmet design

To improve helmet impact protection, this study introduced a novel design of helmets with an aluminium honeycomb to reinforce the front part of the inner liner, as illustrated in Figure 3.10. A tied interface *CONTACT_TIE_NODES_TO_SURFACE was used to model the connection of the inner liner and honeycomb filler. According to the experimental results of the out-of-plane compression of the honeycomb presented in Figure 3.9, the plateau stress of the honeycomb specimen ($c \times t = 3.2$ mm $\times$ 0.08 mm) can be calculated, which is about 2 MPa. In accordance with Gibson and Ashby's study [186], the plateau stress of regular hexagon honeycomb columns under out-of-plane compression can be predicted by the following analytical model,

$$\sigma_p \approx 6.6\sigma_y \left(\frac{t}{c}\right)^{\frac{5}{3}},\tag{3.1}$$

where the σ_p is the plateau stress and σ_y is the yield stress of aluminium material. Thus, the plateau stress of the honeycomb specimen can be analytically predicted as $\sigma_p \approx 2.05$ MPa, which demonstrates that Eq (3.1) can be applied to this study. According to Caserta et al.'s study [42], the best motorcycle helmet performance can be achieved when using honeycomb filler with a crush strength of 0.7 MPa, which can offer a general direction for choosing the geometry of the honeycomb cell. As such, three different cells for honeycomb fillers, i.e. C5T4 ($c \times t = 5$ mm $\times$ 0.04 mm, $\sigma_p \approx 0.31$ MPa), C5T5 ($c \times t = 5$ mm $\times$ 0.05 mm, $\sigma_p \approx 0.44$ MPa) and C5T6 ($c \times t = 5$ mm $\times$ 0.06 mm, $\sigma_p \approx 0.6$ MPa), were adopted here to study the effects of honeycomb fillers on helmet protection performance. It should be noted that a much wider range of honeycomb geometries was selected for a further optimisation study in Section 3.4. Based upon the validated models in Section 3.2, the head models coupled with the helmet

models with/without honeycomb filler were developed to investigate the effects of honeycomb filler on the helmet protection performance based on head responses, such as head kinematics and the tissue-level injury predictors.
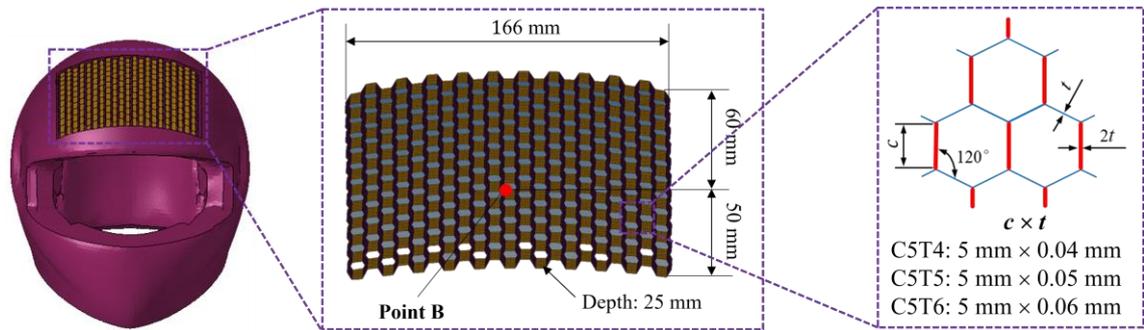
Figure 3.10. Illustration of the helmet with honeycomb filler

3.3.2 Acceleration transmitted to the head

As shown in Figure 3.11, virtual drop tests for the four different Hybrid III head-helmet models, i.e. conventional helmet without honeycomb filler and novel helmets with different honeycomb fillers, were carried out to investigate the influences of honeycomb filler on the acceleration transmitted to the helmeted head. Noting that three different configurations of honeycomb fillers, i.e. C5T4, C5T5 and C5T6, were considered here to explore the effects of honeycomb configuration on the acceleration responses of head-helmet models and one conventional helmet without honeycomb filler was selected for the comparison.
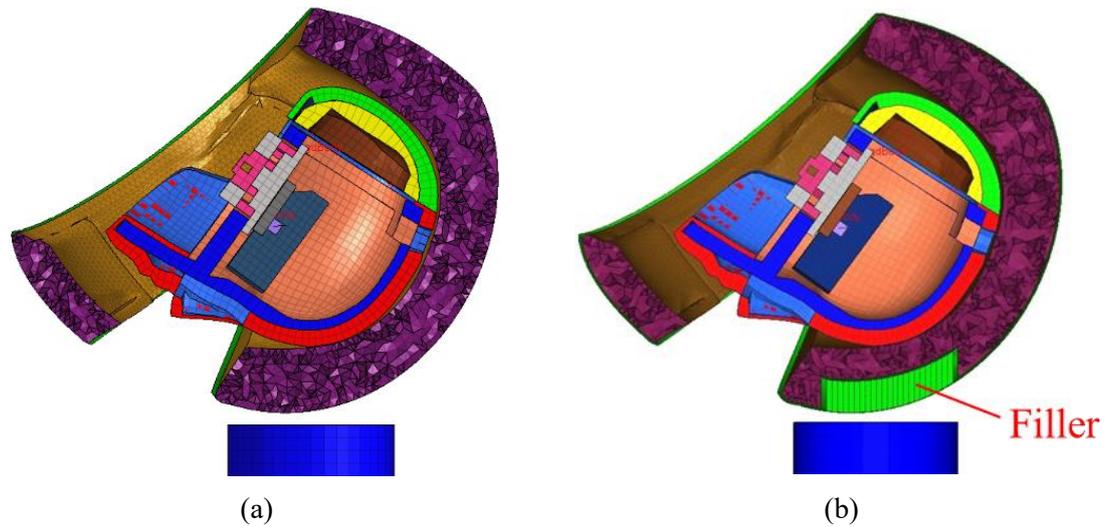
Figure 3.11. Sectional view of the Hybrid III head-helmet models, (a) helmet without honeycomb filler, (b) helmet with honeycomb filler

The acceleration-time curves from four different Hybrid III head-helmet models under drop tests are shown in Figure 3.12. It can be found that three helmets with honeycomb fillers can help in reducing the peak acceleration transmitted to the head in comparison with the conventional helmet without honeycomb fillers. The values of both peak acceleration and HIC for all simulated models are compared in Table 3.3, in which the weights of helmets with/without honeycomb fillers were listed. The peak acceleration and HIC values for the helmet with three different honeycomb fillers are lower than the corresponding values (A_{max} = 215.1 g and HIC = 1985) for the conventional helmet without filler, which demonstrates the positive effect of honeycomb fillers on the improvement of helmet protection performance. In addition, the helmet with filler C5T4 is of the best impact protection due to the smallest peak acceleration and HIC values (A_{max} = 161.5 g and HIC = 1269), which can be explained by the deformation patterns of the three honeycomb fillers during the impact, as shown in Figure 3.13. The load resistance of honeycomb fillers decreased with the decrease of the honeycomb cell wall thickness from 0.06 mm to 0.04 mm, which promotes honeycomb filler C5T4 to deform and spread the impact load over a larger area. Consequently, the energy absorption is increased due to a larger area of effective liner to absorb energy and reduce the

acceleration transmitted to the head.
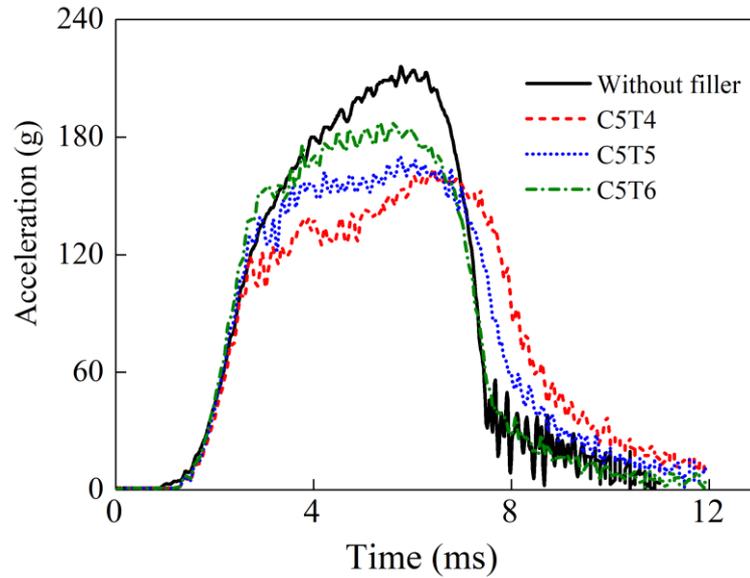
Figure 3.12. Acceleration-time curves transmitted to the head in drop test simulations for four different helmets

Table 3.3. Numerical results of four Hybrid III head-helmet models

	Weight	Peak acceleration (A_{max})	*HIC* value
Helmet without filler	1.672 kg	215.1 g	1985
Helmet with filler C5T4	1.662 kg	161.5 g	1269
Helmet with filler C5T5	1.666 kg	170.3 g	1440
Helmet with filler C5T6	1.669 kg	188.2 g	1730

Honeycomb filler C5T4   Honeycomb filler C5T5   Honeycomb filler C5T6

(a)

Honeycomb filler C5T4   Honeycomb filler C5T5   Honeycomb filler C5T6

(b)
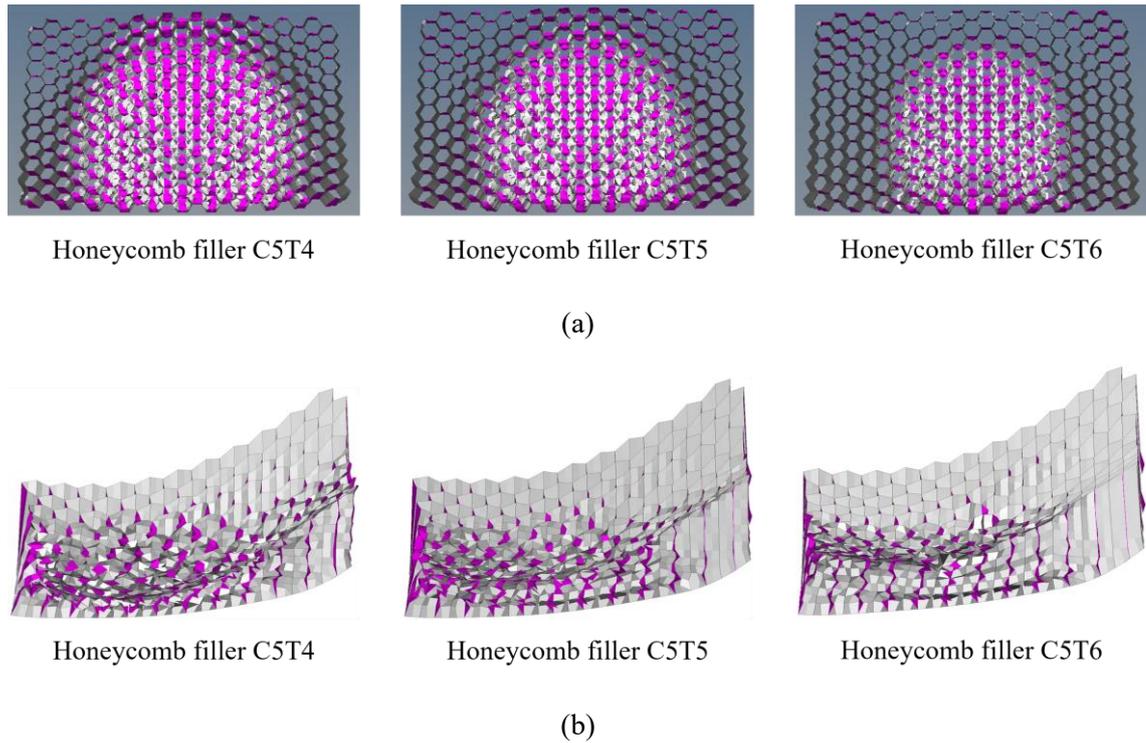
Figure 3.13. Final deformation for three different aluminium honeycomb fillers, (a) top view, (b) lateral view

3.3.3   Tissue-level responses of the head

As shown in Figure 3.14, to assess the impact protection performance of helmets with/without honeycomb filler in terms of the tissue-level responses of the head, virtual drop tests were performed on four different THUMS head-helmet models, including one conventional helmet without filler and three helmets with different honeycomb fillers, i.e. C5T4, C5T5 and C5T6, coupled with the THUMS head model. According to the medical report [217], the possibility of brain injury is significantly higher than the likelihood of skull fracture. Usually, the head under the helmet protection is unlikely to suffer the injuries of skull fracture, but brain injuries occur very frequently. Thus, the tissue-level responses, such as intracranial pressure (ICP) and von Mises stress (σ_v) in the brain, were adopted for the head injury analysis.
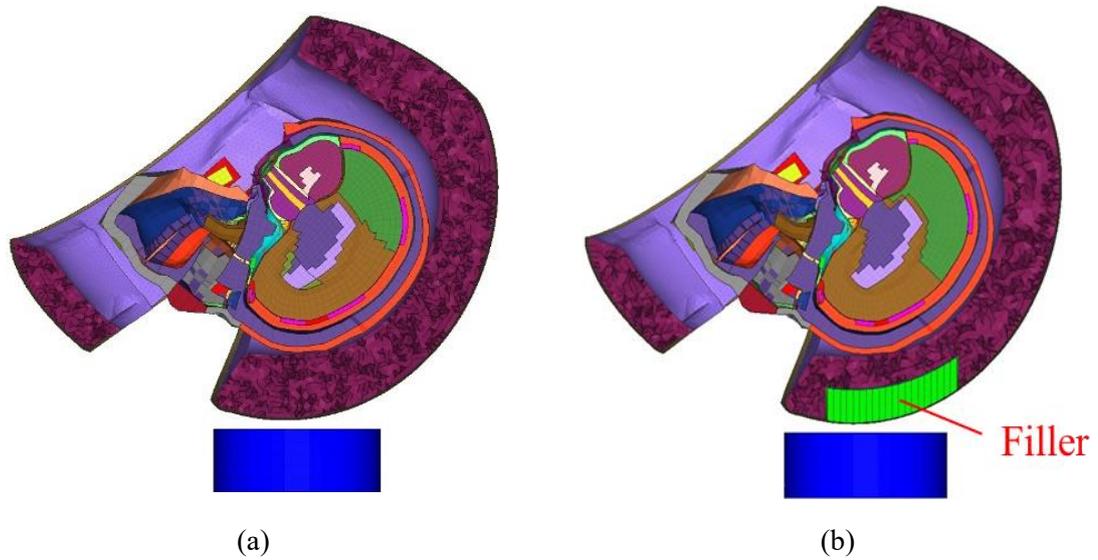
Figure 3.14. Sectional view of the THUMS head-helmet models, (a) helmet without honeycomb filler, (b) helmet with honeycomb filler

3.3.3.1   *Intracranial pressure*

The *ICP* gradient across the brain can be observed from the numerical results, and the distributions of the *ICP* contour for the THUMS head-helmet models at different impact times (i.e. 2.5, 4.0, 5.5 and 7.0 ms) are presented in Figure 3.15. These gradient pressure agree well with those measured by Nahum et al. [81] and other simulated results in the reported literature [104, 218]. Among four different THUMS head-helmet models, the conventional helmet without honeycomb filler is of a maximum *ICP* value of 228.8 kPa, which is lower than a common threshold value of 235 kPa for the serious brain injury but higher than a threshold of 173 kPa for the moderate brain injury [219], indicating that the helmeted head cannot be protected perfectly and head injury may still happen. Therefore, there is a great need to further improve helmet protection to reduce head injury. As for the novel helmets, the values of *ICP* for the helmet with honeycomb filler C5T4 and C5T5 were 196.6 kPa and 218.6 kPa, respectively, lower than the value for the conventional helmet, while the helmet with honeycomb filler C5T6 gave the largest *ICP* value of 239.1 kPa. In comparison with the conventional helmet without filler, a novel helmet with honeycomb filler C5T4 or C5T5 can help in decreasing the *ICP* value for reducing the

possibility and severity of head injury; however, the helmet with honeycomb filler C5T6

shows a negative effect on the impact protection improvement.
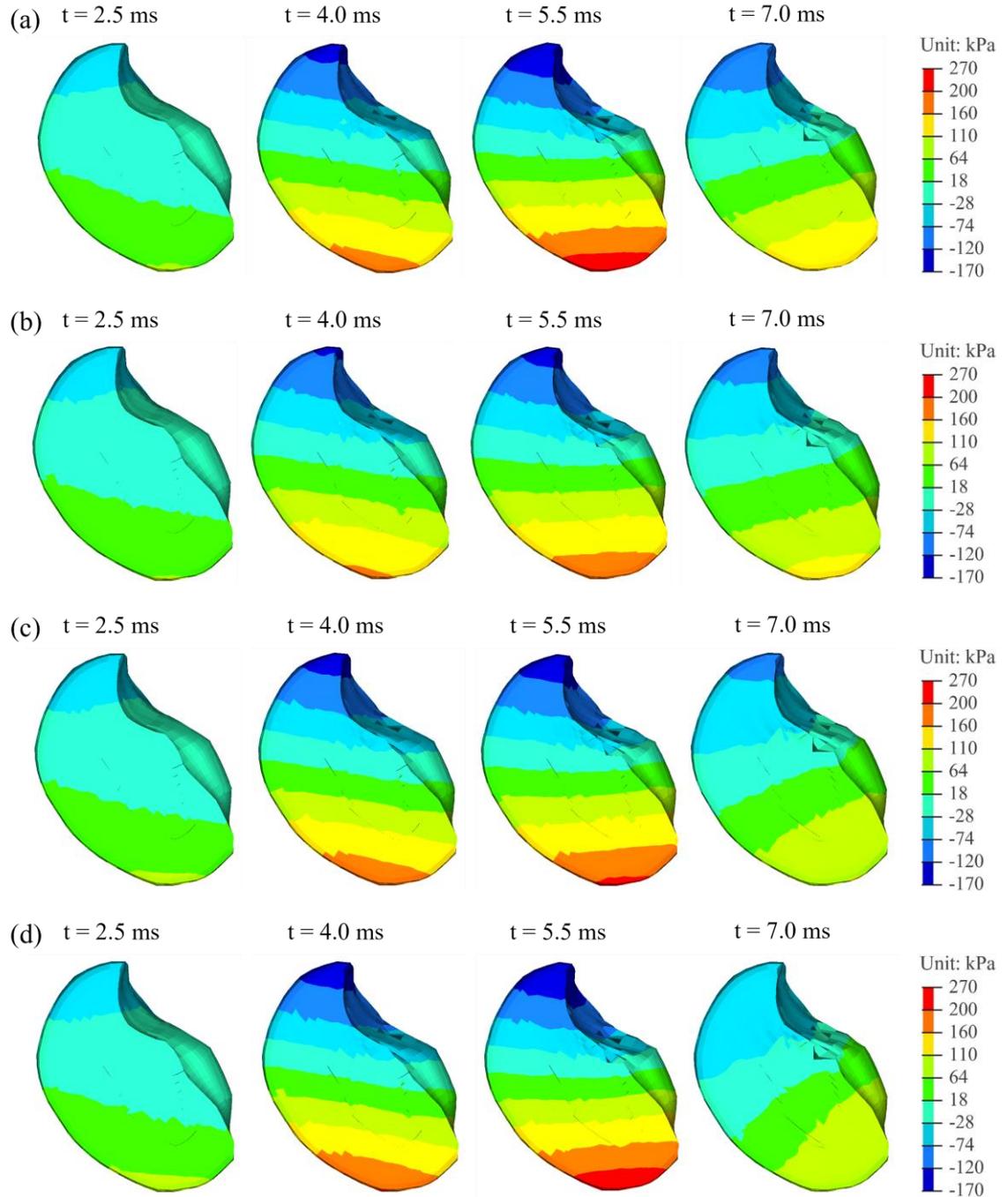
Figure 3.15. *ICP* gradients for four THUMS head-helmet models, (a) helmet without honeycomb filler (Max *ICP* = 228.8 kPa), (b) helmet with honeycomb filler C5T4 (Max *ICP* = 196.6 kPa), (c) helmet with honeycomb filler C5T5 (Max *ICP* = 218.6 kPa), (d) helmet with honeycomb filler C5T6 (Max *ICP* = 239.1 kPa)

3.3.3.2   *von Mises stress*

The distributions of the σ_v contour for the THUMS head-helmet models at different times (i.e. 2.5 ms, 4.0 ms, 5.5 ms and 7.0 ms) are illustrated in Figure 3.16, in which very similar patterns and their associated values of σ_v for four head-helmet models can be observed at each moment. The maximum σ_v for the conventional head-helmet model was 33.6 kPa, and the values for the helmet with honeycomb fillers C5T4 and C5T5 were decreased to 28.4 kPa and 30.7 kPa, respectively. However, the maximum σ_v of 35.7 kPa was obtained for the helmet with honeycomb filler C5T6, which was of a lower protection performance than the conventional helmet in terms of the σ_v responses. According to the σ_v thresholds reported in literature [220], such as the value of 18 kPa for 50% probability of mild injury and 38 kPa for 50% probability of severe injury. It can be concluded that the conventional and three proposed novel helmets cannot prevent head injury completely, while the brain still of 50% probability of mild injury for the safest helmet with honeycomb filler C5T4. The σ_v-based injury indicator coincided with the ICP-based injury indicator. All these head responses indicated that there is still a significant need for helmet protection improvement. The helmet with honeycomb filler could be one possible solution to achieve this goal.
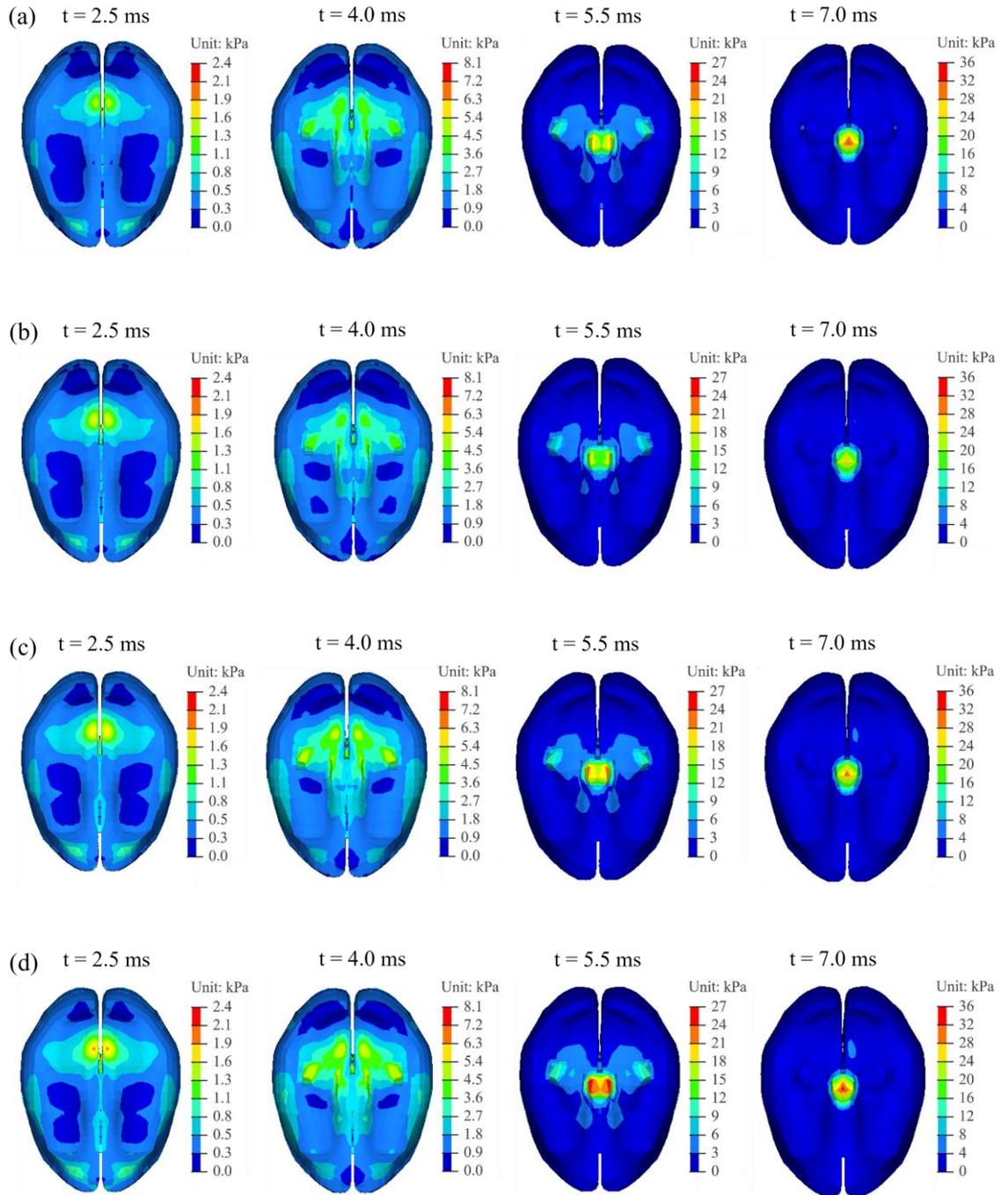
Figure 3.16. von Mises stresses of the brain for four THUMS head-helmet models, (a) helmet without honeycomb filler (Max σ_v = 33.6 kPa), (b) helmet with honeycomb filler C5T4 (Max σ_v = 28.4 kPa), (c) helmet with honeycomb filler C5T5 (Max σ_v = 30.7 kPa), (d) helmet with honeycomb filler C5T6 (Max σ_v = 35.7 kPa)

3.3.4 Analysis of honeycomb-filled helmet protection

To further investigate the effects of honeycomb filler on the protection of honeycomb-filled helmets under the front impact, both the kinematic-based injury predictors, (i.e. A_{max} and HIC) from the Hybrid III head-helmet models and the tissue-level injury predictors (i.e. ICP and σ_v) from the THUMS head-helmet models were discussed here. For facilitating comparison, the head response ratios between each of the three novel helmets (with honeycomb filler C5T4, or C5T5, or C5T6) and the conventional helmet (without filler) are illustrated in Figure 3.17, in which all head responses were normalised using the corresponding head responses associated with the conventional helmet. Clearly, four different smallest ratios (0.751, 0.639, 0.859 and 0.845 for A_{max}, HIC, ICP and σ_v, respectively) are from the novel helmet with honeycomb filler C5T4, indicating its greatest improvement in impact protection performance. The ratios for the novel helmet with honeycomb filler C5T5 are also lower than unity, and therefore, the protection performance of this helmet is better than the conventional helmet. As for the helmet with honeycomb filler C5T6, the ratios of kinematic-based predictors were lower than those of the helmet without filler. However, the tissue-level responses were higher than the conventional counterparts. Although the novel helmet with honeycomb filler C5T6 can reduce the levels of acceleration and HIC value, the negative influences on the tissue-level responses are observed. Overall, the configuration of honeycomb filler plays a significant role in helmet protection enhancement.
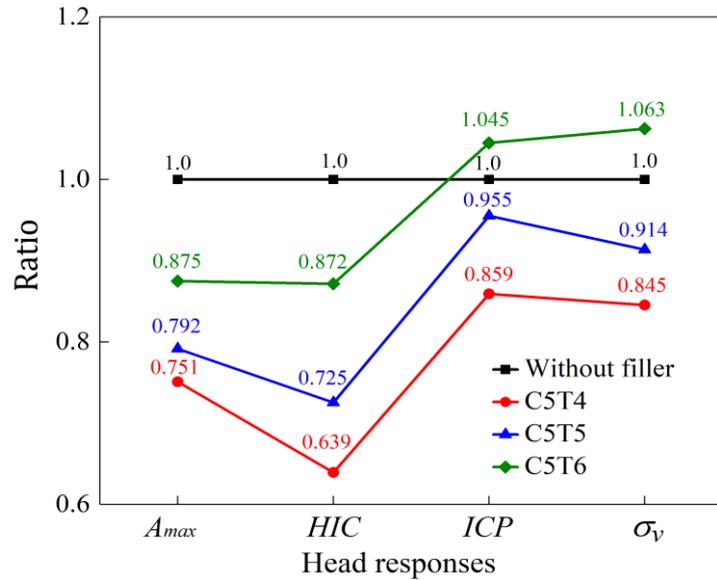
Figure 3.17. Comparison of the protection between conventional and novel helmets against head response ratios

3.4   Discrete design optimisation for helmet design

From the above study, it can be found that the protection performance of the novel helmet can be optimised by choosing different configurations of honeycomb fillers, which could be achieved using structural optimisation. The methodology of orthogonal array design for the discrete optimisation study has been widely reported in literature [221-225], which can be also introduced to efficiently seek the optimal design for the helmet.

3.4.1   Efficient optimisation method

3.4.1.1   *Full factorial design*

In an optimisation problem, the objective is to find the optimal combination of levels (or possible values) for each factor (or design variable). In general, full factorial design can be used to consider all possible combinations of all design variables with all design levels [225]. Suppose that there are n factors with l_1, l_2, …, l_n levels, respectively, then $l_1 \times l_2 \times ... \times l_n$ combinations should be conducted for the full factorial design.

The main drawback of the full factorial design is that very large amounts of experiments/simulations are required to be conducted when the numbers of the design factors and/or levels are large. For example, a full factorial design with $n = 7$ factors and $l_1 = l_2 = \ldots = l_n = 2$ levels needs to consider $2^7 (= 128)$ combinations.

3.4.1.2 *Orthogonal array design*

The orthogonal array design is a fractional factorial design which is a certain fractional subset of the full factorial set of designs, and the orthogonality (independence) among various factors and certain interactions can be maintained after careful selection of the orthogonal array [226, 227]. Thus, in comparison with the full factorial design, the orthogonal array can lead to a smaller but representative set of design combinations.

The orthogonal array design can be presented as $L_m(l^n)$, in which L represents the orthogonal array, l is the number of the levels, n is the number of the factors, m is the number of the rows (i.e. the number of design combinations). For example, the $L_8(2^7)$ can be used for orthogonal array design with $n = 7$ factors and $l_1 = l_2 = \ldots = l_n = 2$ levels, as presented in Table 3.4. This orthogonal array design only needs to consider 8 design combinations, far less than 128 combinations of the full factorial design.

The orthogonal array can be characterised by orthogonality. To facilitate understanding of orthogonality, the levels in Table 3.4 are converted from (1, 2) to (-1, 1), then the first two columns of designs can be represented using vectors $\mathbf{F_1} = (-1, -1, -1, -1, 1, 1, 1, 1)$ and $\mathbf{F_2} = (-1, -1, 1, 1, -1, -1, 1, 1)$, and thus $\mathbf{F_1}\mathbf{F_2}^\mathbf{T} = 0$ can be obtained to demonstrate the orthogonality of orthogonal array design. This orthogonality means that (i) the levels of a factor should appear the same times in the orthogonality array; and (ii) the ordered pairs formed by the rows restricted to any two columns are all the possible ordered pairs of the two-element set, i.e. (1, 1), (1, 2), (2, 1) and (2, 2).

Table 3.4. The $L_8(2^7)$ orthogonal array

Experiment No.	Factor						
	F_1	F_2	F_3	F_4	F_5	F_6	F_7
1	1	1	1	1	1	1	1
2	1	1	1	2	2	2	2
3	1	2	2	1	1	2	2
4	1	2	2	2	2	1	1
5	2	1	2	1	2	1	2
6	2	1	2	2	1	2	1
7	2	2	1	1	2	2	1
8	2	2	1	2	1	1	2

3.4.1.3   *Optimisation algorithm using orthogonal array design*

The flowchart of the procedures for the discrete optimisation algorithm is presented in Figure 3.18, whose detailed steps are illustrated as follows [222, 228].

Step 1: The optimisation problem definition. The optimisation objective function, discrete design variables and constraints are used to define the optimisation problem, which can be expressed as follows.

$$\begin{cases} \text{Find } \boldsymbol{x} \\ \text{minimize } R(\boldsymbol{x}) \\ \text{subject to } G_i(\boldsymbol{x}) \leq 0, \ i = 1,\dots,k \end{cases}, \tag{3.2}$$

where $\boldsymbol{x}$ is the discrete design variable, $R(\boldsymbol{x})$ is the optimisation objective function, $G_i(\boldsymbol{x})$ is the constrain function and k is the number of constraints.

Step 2: Orthogonal array method. An orthogonal array is determined based on the

optimisation problem. As shown in Table 3.5, the $L_9(3^3)$ was selected due to the numbers of both design variables (A, B, C) and levels (1, 2, 3) being three in the optimisation iteration (see Section 3.4.2), and nine calculations are needed for each iteration [227].

Step 3: Arrangement of the levels for design variables. The discrete values are selected to be three levels for each design variable in the initial design. In particular, one selected value is first assigned to the second level (i.e. Level 2) for the corresponding design variable; then neighbouring smaller values are assigned to the first level and the neighbouring larger one is assigned to the third level [227].

Step 4: Penalized objective function. The new objective function (R_{new}) is defined to consider the constraint violations as follows.

$$R_{new} = min\{R(\boldsymbol{x}) + P(\boldsymbol{x})\}, \tag{3.3}$$

$$P(\boldsymbol{x}) = \lambda * max(0, V_i), \tag{3.4}$$

in which $P(\boldsymbol{x})$ is the penalty function, λ denotes the scaling factor, V_i is the maximum violation of the *i*-th constraint [222]. The value of λ is set to be zero when the constraint condition is satisfied; otherwise, λ is set as a positive value at least ten times greater than the objective function to neglect the unsatisfied design in which the constraint fucntion cannot be satisfied [229].

Step 5: Selection of an optimum design. The analysis of mean (ANOM) method is used for obtaining an optimum level, as shown in Table 3.6, which becomes the new levels of design variables for the next iteration [226].

Step 6: Convergence criteria. The convergence criteria include (i) no new smaller R_{new}

is obtained in the next five iterations, or (ii) the maximum number of iterations is reached [222]. The optimisation step is terminated if one of the above two convergence criteria is met; otherwise, the optimisation algorithm returns to **Step 3** for a new iteration.
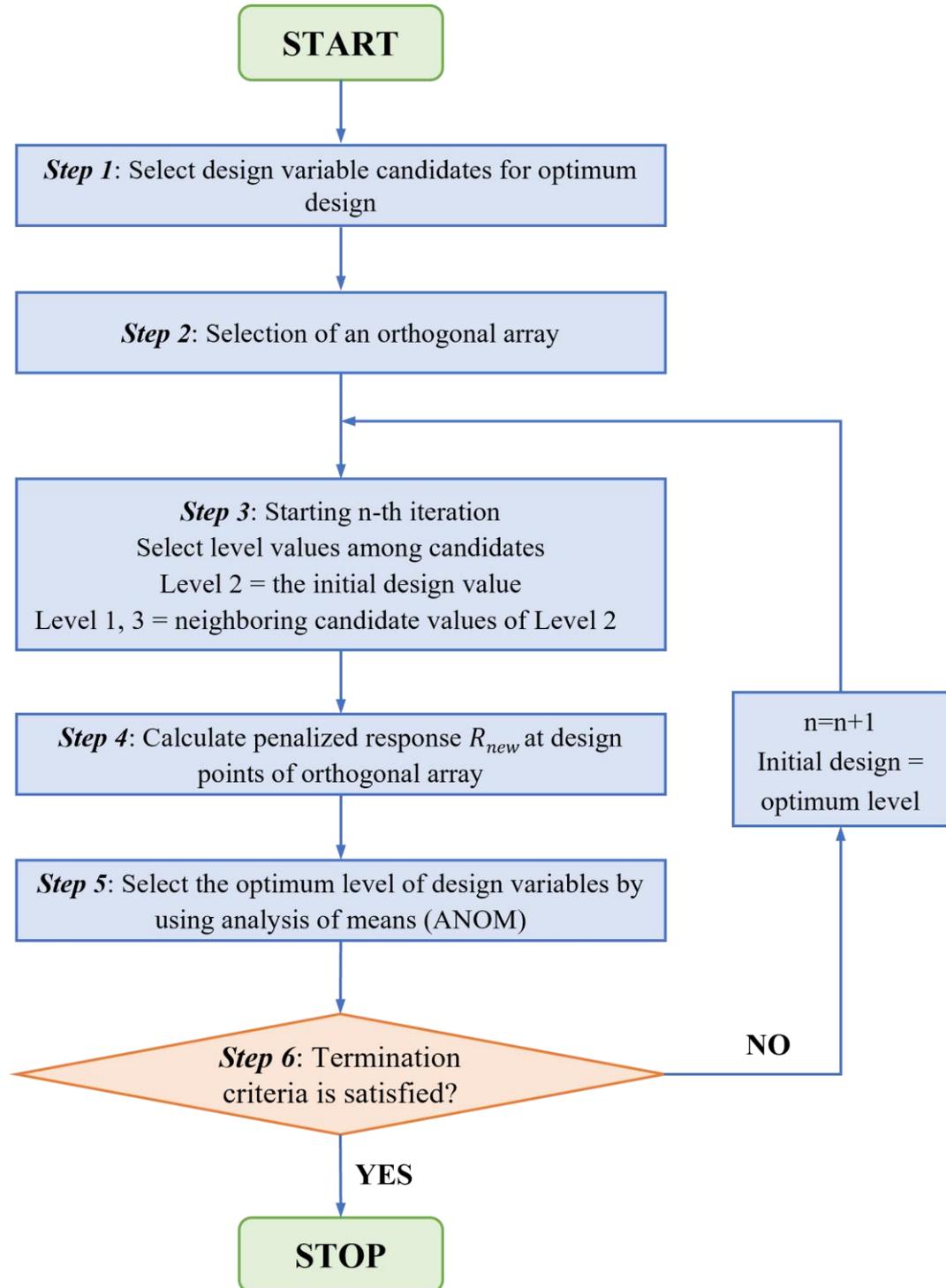
Figure 3.18. Flowchart of the discrete optimisation algorithm

Table 3.5. The $L_9(3^3)$ orthogonal array with the new objective function

Experiment No.	Levels of design variables			R_{new}
	A	B	C	
1	1	1	1	R_{new1}
2	1	2	2	R_{new2}
3	1	3	3	R_{new3}
4	2	1	2	R_{new4}
5	2	2	3	R_{new5}
6	2	3	1	R_{new6}
7	3	1	3	R_{new7}
8	3	2	1	R_{new8}
9	3	3	2	R_{new9}

Table 3.6. Mean of R_{new} corresponding to each level

Design variables	Levels of design variables		
	1	2	3
A	$(R_{new1}+R_{new2}+R_{new3})/3$	$(R_{new4}+R_{new5}+R_{new6})/3$	$(R_{new7}+R_{new8}+R_{new9})/3$
B	$(R_{new1}+R_{new4}+R_{new7})/3$	$(R_{new2}+R_{new5}+R_{new8})/3$	$(R_{new3}+R_{new6}+R_{new9})/3$
C	$(R_{new1}+R_{new6}+R_{new8})/3$	$(R_{new2}+R_{new4}+R_{new9})/3$	$(R_{new3}+R_{new5}+R_{new7})/3$

3.4.2   Description of the optimisation problem

Besides the honeycomb filler, EPS liner foam is also expected to dissipate impact energy to improve the novel helmet protection. Therefore, both the geometries of honeycomb filler and the density of EPS foam were considered here for the optimisation design. Specifically, eight levels (i.e. possible values) of side length and eight levels of the wall

thickness of the honeycomb cell as well as four levels of density of EPS foam were selected as the design variables to optimise the configuration of the novel helmet, as summarized in Table 3.7. The four stress-strain curves for EPS foams with different densities are illustrated in Figure 3.19 and the material properties for EPS foam of four different densities are listed in Table 3.8 [27].

Table 3.7. The discrete values of design variables for helmet optimisation design

Description	1	2	3	4	5	6	7	8
c (mm)	3.0	3.5	4.0	4.5	5.0	5.5	6.0	6.5
t (mm)	0.03	0.04	0.05	0.06	0.07	0.08	0.09	0.10
ρ (kg/m^3)	50	64	80	100	/	/	/	/
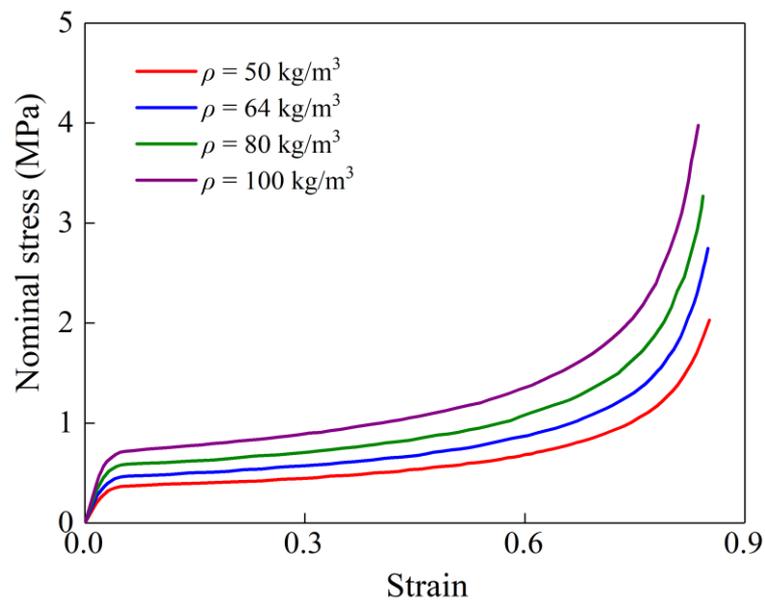
Figure 3.19. Nominal uniaxial compressive stress-strain curves for EPS foams with different densities (redrawn from [27])

Table 3.8. Material properties for EPS foams with different densities [27]

Density (kg/m³)	Young's modulus (MPa)	Poisson's ratio	Yield stress (kPa)
50	12.7	0.01	350
64	16.3	0.01	450
80	19.0	0.01	580
100	25.1	0.01	720

As mentioned in Section 3.3, both kinematic-based injury predictors (A_{max}, HIC) and tissue-level injury predictors (ICP, σ_v) for the helmeted head can be obtained to assess helmet protection. Among the above four head injury predictors, the kinematic-based predictors are based on head acceleration, which was proposed for skull fracture injury, while the tissue-level responses were linked to brain injury [87, 95]. To explore the optimal configuration for the novel helmet protection with regard to overall head injury predictors (A_{max}, HIC, ICP and σ_v), the weighting factor (w^α) was applied here to combine two different kinds of head injuries, i.e. both skull fracture and brain injury were considered for helmet optimisation. Noting that the weighting factor is changeable, which is related to the relative importance of each head injury predictor [205]. However, there are insufficient studies available to determine the exact relative importance of each type of head injury. It was assumed here that each head injury predictor is of equal importance for the overall head injuries, thus the weighting factor of each head injury predictor was set to be 0.25, i.e. $w^{Amax} = w^{HIC} = w^{ICP} = w^{\sigma_v} = 0.25$. More accurate values of the weighting factors could be adopted when they are available. As presented in Eq. (3.5), the weighting factor, as well as the ratios of head responses of the novel helmet and conventional helmet, were used here for facilitating the comparison, where the head responses ($A_{max} = 215.1$ g, $HIC = 1985$, $ICP = 228.8$ kPa, $\sigma_v = 33.6$ kPa) for conventional helmet without filler were obtained from Section 3.3. Furthermore,

according to the Standard ECE 22.05 [19], the maximum acceleration transmitted to the head should not exceed 275 g. Hence, the value of 275 g was considered here as an upper limit of A_{max}. The objective function and constraints of the optimisation problem are given by

$$\begin{cases} R(c,t,\rho) = \min\left\{ w^{A_{max}} * \dfrac{A_{max}(c,t,\rho)}{215.1} + w^{HIC} * \dfrac{HIC(c,t,\rho)}{1985} + w^{ICP} * \dfrac{ICP(c,t,\rho)}{228.8} + w^{\sigma_v} * \dfrac{\sigma_v(c,t,\rho)}{33.6} \right\} \\ s.t \begin{cases} A_{max}(c,t,\rho) \leq 275 \text{ g} \\ c \in (3.0, 3.5, 4.0, 4.5, 5.0, 5.5, 6.0, 6.5) \\ t \in (0.03, 0.04, 0.05, 0.06, 0.07, 0.08, 0.09, 0.10) \\ \rho \in (50, 64, 80, 100) \end{cases} \end{cases} \qquad (3.5)$$

The above-constrained optimisation problem can be transformed into an unconstrained optimisation problem by using the penalty function. The penalty function for the maximum acceleration is given by

$$P(c,t,\rho) = \lambda * \max[0, A_{max}(c,t,\rho) - 275], \qquad (3.6)$$

where the scaling factor λ was set to be 1000 to neglect the unsatisfied design [221]. The optimisation problem then is formulated as

$$\begin{cases} R_{new} = \min\{R(c,t,\rho) + P(c,t,\rho)\} \\ s.t \begin{cases} A_{max}(c,t,\rho) \leq 275 \text{ } g \\ c \in (3.0, 3.5, 4.0, 4.5, 5.0, 5.5, 6.0, 6.5) \\ t \in (0.03, 0.04, 0.05, 0.06, 0.07, 0.08, 0.09, 0.10) \\ \rho \in (50, 64, 80, 100) \end{cases} \end{cases} \qquad (3.7)$$

The helmet with honeycomb filler C5T5 (ρ = 80 kg/m³, c = 5.0 mm and t = 0.05 mm) was selected as the initial design of the optimisation. The details of the first iteration for the optimisation and the associated R_{new} were listed in Table 3.9.

Table 3.9. The discrete values of design variables in the first iteration

Simulation No.	Levels of design variables			A_{max} (g)	HIC	ICP (kPa)	σ_v (kPa)	R_{new}
	c (mm)	t (mm)	ρ (kg/m³)					
1	4.5	0.04	64	156.6	2009	203.8	30.59	0.885
2	4.5	0.05	80	163.7	1420	234.2	38.1	0.908
3	4.5	0.06	100	189.2	1764	270.3	36.9	1.012
4	5.0	0.04	80	161.5	1365	196.6	28.4	0.786
5	5.0	0.05	100	173.2	1541	226	34.3	0.897
6	5.0	0.06	64	189.5	1558	233	37.1	0.947
7	5.5	0.04	100	158.3	1209	195.7	27.5	0.755
8	5.5	0.05	64	158.9	1228	207.3	31.2	0.798
9	5.5	0.06	80	173.9	1783	231	37	0.954

According to the above results of R_{new}, ANOM method (Table 3.6) was used to determine the levels of the optimum in the first iteration, as presented in Table 3.10. Specifically, the minimum/optimal values of the mean of R_{new} for each design variable in the first iteration can be found from Table 3.10, such as 0.836 for c at the Level 3 (i.e. c = 5.5 mm, see Table 3.5 and Table 3.9), 0.809 for t at the Level 1 (i.e. t = 0.04 mm), and 0.877 for ρ at the Level 1 (i.e. ρ = 64 kg/m³). Thus, the levels of c = 5.5 mm, t = 0.04 mm and ρ = 64 kg/m³ in the first iteration were selected as three new initial Level 2 of each design variable for the next optimisation iteration, see Figure 3.18.

Table 3.10. Mean of R_{new} corresponding to each level in the first iteration

Design variable	Levels of design variables		
	1	2	3
c	0.935	0.877	**0.836**
t	**0.809**	0.868	0.971
ρ	**0.877**	0.883	0.888

3.4.3   Optimisation results

The optimisation iteration for the protection performance of the honeycomb-filled helmet is presented in Figure 3.20. It is shown that the R_{new} of the initial design was 0.847 and the value decreased to 0.570 after four optimisation iterations. Eventually, the optimisation stopped at the eighth iteration due to that R_{new} values were not improved in the following four iterations and the convergence criteria of the optimisation were met.
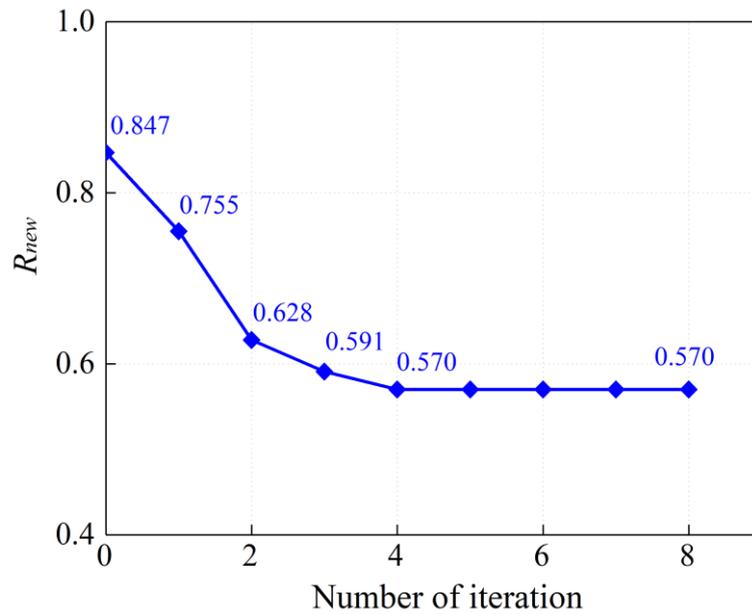
Figure 3.20. The iteration process of discrete optimisation for the novel helmet

The numerical results of the initial and optimum designs for the novel helmet are summarized in Table 3.11, in which the data of the conventional helmet and helmet C5T4 are included for comparison. In addition, all ratios of head responses for conventional helmet and three novel helmets are compared in Figure 3.21. It can be found that all head responses for the initial design of the novel helmet with honeycomb filler ($\rho = 80$ kg/m^3, $c = 5.0$ mm and $t = 0.05$ mm) were lower than those of the conventional helmet without honeycomb filler, indicating the impact protection of the initial design of novel helmet was improved from the conventional helmet. In comparison with the initial design of the novel helmet, the head responses for the helmet C5T4 were reduced. Furthermore, the

head responses for the optimum design of the novel helmet (ρ = 50 kg/m³, c = 6.0 mm and t = 0.03 mm) were significantly reduced comparing with those for all the above novel and conventional helmet designs. Therefore, the optimum helmet design is of the best protection performance under front impacts.

Table 3.11. Comparison of the protection performance of different helmet designs

Description	Weight (kg)	c (mm)	t (mm)	ρ (kg/m³)	A_{max} (g)	HIC	ICP (kPa)	σ_v (kPa)	R_{new}
Conventional helmet	1.672	/	/	80	215.1	1985	228.8	33.6	1
Helmet C5T4	1.662	5.0	0.04	80	161.5	1269	196.6	28.4	0.773
Initial design	1.666	5.0	0.05	80	170.3	1440	218.6	30.7	0.847
Optimum design	1.488	6.0	0.03	50	137.0	918	146.9	18.1	0.570
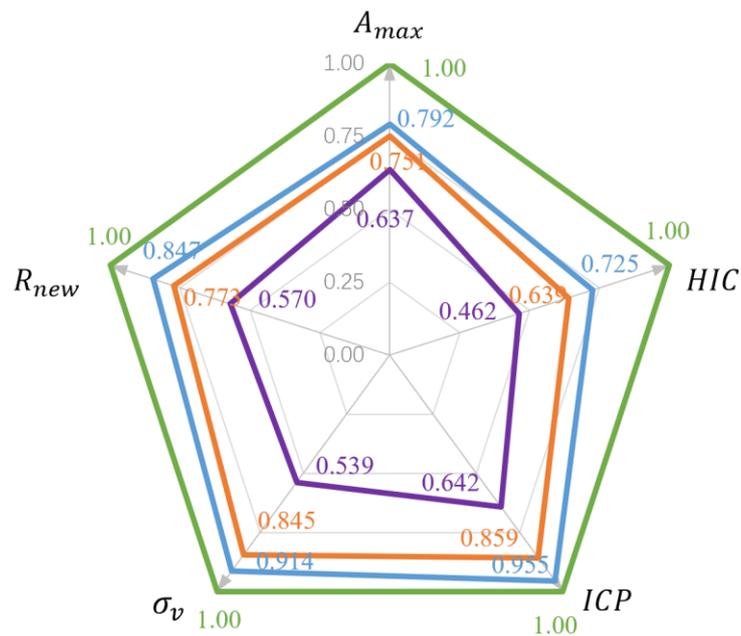
Figure 3.21. Comparison of the protection performance of different helmets in terms of five indicators (A_{max}, HIC, ICP, σ_v and R_{new})

3.5 Discussion

A full-face motorcycle helmet was modelled, and standard free drop impacts at the front position of the helmet were experimentally tested and numerically simulated. The numerical results show a good agreement with the experimental results, thus the accuracy of the helmet model can be validated. According to the requirements of Standard ECE 22.05 [19], the A_{max} transmitted to the helmeted headform should not exceed 275 g during the test, and the HIC should not exceed 2400. Both A_{max} and HIC results of the conventional helmet are smaller than their corresponding limits, indicating that the conventional helmet can pass the ECE 22.05 requirements. However, the threshold of HIC prescribed in Standard ECE 22.05 is very high, while the moderate head injury can be predicted for HIC = 1000, and serious head injury can be predicted for HIC = 1500 [150, 230]. In addition, based on the Standard FMVSS 208 [71], a HIC value of 1000 with a time interval no more than 36 ms is regarded as a threshold for head injury. As presented in Table 3.2, all HIC values were lower than the threshold of 2400 but much higher than the threshold of 1000, indicating that the standard helmet cannot completely prevent head injury in the drop test, and therefore, helmet protection needs to be improved to reduce the possibility and severity of head injury.

To improve helmet protection, a novel helmet design with a foam liner reinforced by a honeycomb filler was first proposed by Caserta et al. [42] and also reported by Kholoosi et al. [35, 207]. In their studies, impact accelerations transmitted to the helmeted headform were measured and the HIC values were calculated to assess the protection performance of the novel honeycomb-filled helmet; however, the tissue-level injury predictors were not used in previous studies. In this study, tissue-level injury predictors were measured by the THUMS head-helmet models to comprehensively assess the honeycomb-filled helmet protection performance.

In light of previous studies [96, 98, 117, 218, 231], researchers measured the impact accelerations from the helmeted Hybrid III headform, and then imposed the accelerations on the high biofidelity head models to predict tissue-level responses for the helmet protection assessment. The computational costs can be saved because the high biofidelity head models were not coupled with the helmet models. In this study, the high biofidelity THUMS head model was coupled with the helmet model to replicate more realistic helmeted head impact scenarios. To obtain the advantage of the high biofidelity head-helmet modelling and overcome the drawback of computational costs, an efficient orthogonal array design optimisation method presented in this study can be employed for the head-helmet models to efficiently find the optimal design of the helmet. For example, according to the previous full factorial design optimisation method [33], 8×8×4 (= 256) combinations of three design factors (i.e. foam density of helmet liner, side length and wall thickness of the honeycomb cell, see Table 3.7) need to be simulated to find the optimal design of honeycomb-filled helmet protection. In contrast, the optimal design can be found after four iterations (Figure 3.20) based on the efficient orthogonal array design optimisation method, as each iteration calculated nine combinations. Thus the computational costs can be largely reduced by using the efficient orthogonal array design optimisation method.

This chapter has some limitations. Firstly, only the honeycomb-filled helmet impact onto the flat anvil was investigated in this study, indicating that honeycomb fillers were prone to experience out-of-plane compression in such loading conditions. Whereas the mechanical behaviours of honeycombs are sensitive to loading directions, the impact attenuation capacities of honeycombs under in-plane or shear compression are much different [186]. Thus, it is suggested that the effects of the impact directions on the honeycomb-filled helmet also need to be considered. According to the helmet standards [19, 20], the kerbstone and hemispherical anvils are also recommended for a more

comprehensive assessment of the design of a honeycomb-filled helmet. Secondly, the σ_v thresholds used in this study are proposed based on the validated SUFEHM, indicating that these σ_v thresholds maybe not be fully applicable to the THUMS head model for the evaluation of head injury although the σ_v values obtained from different coupled THUMS head-helmet models can also be used as a reference to approximately compare the protection improvement of the helmet with different designs. Finally, the practical manufacturing process of the honeycomb-filled helmet was not considered in this study, which may lead to some difficult usage of honeycomb filler in helmet design, and the optimal results for the honeycomb-filled helmet design were not validated against the experimental results. Therefore, once this optimal helmet design is ready for practical application, the corresponding experimental tests need to be performed in advance.

3.6 Conclusions

In this chapter, experiments were used to validate the helmet model obtained using scanned geometries and reliable material parameters. The validated helmet model was coupled with the Hybrid III head model and the high biofidelity THUMS head model to establish coupled head-helmet models to assess the helmet impact protection in terms of head kinematics and tissue-level responses. With the reinforcement of honeycomb filler, the protection performance of the novel helmet can be significantly enhanced in comparison with the protective performance of the conventional helmet without honeycomb filler. To enhance the design efficiency for further improving honeycomb-filled helmet protection, the orthogonal array design optimisation was conducted to the optimum structural parameters of honeycomb and liner foam density for helmet protection. The optimum design for the novel helmet can be efficiently found and considerably improve helmet protection for preventing head injury during impacts. In comparison with the head responses (A_{max} = 215.1 g, HIC = 1985, ICP = 228.8 kPa

and $\sigma_v = 33.6$ kPa) for conventional helmet, the values of head responses ($A_{max} = 137$ g, $HIC = 918$, $ICP = 146.9$ kPa and $\sigma_v = 18.1$ kPa) for the optimum helmet design are significantly reduced, with their respective reductions of 36.3%, 53.8%, 35.8%, and 46.1%. It demonstrated that the orthogonal array design optimisation method based on coupled head-helmet modelling is an effective tool for the reliable and efficient design of the helmet.

4 Analytical Method for Functionally Graded Polymeric Foam

Publication Information

---

[*]Corresponding author.

4.1 Introduction

The previous **Chapter 3** employed the orthogonal array design optimisation method based on the head-helmet modelling to improve the computational efficiency of helmet optimisation. However, this efficient optimisation method cannot help to characterise and analyse the potential advanced impact-attenuating materials for helmet design. As mentioned in Section 2.3.1, the advanced materials can offer more design space to further upgrade helmet protection from the material level [12], and functionally graded polymeric foam (FGPF) can be introduced to the helmet liner to improve the impact-attenuating capacity of the helmet liner and also compensate excessive stiffness of the composite helmet shell [27, 43]. To help the material analysis and selection for helmet design, the numerical method can be adopted to characterise, design and optimise the FGPF [165]. However, the FE model development of FGPF demands considerable time [176, 184], and the experimental work on FGPF is also highly time-consuming [185]. As such, it is necessary to develop an analytical method to predict the mechanical characteristics of FGPF accurately and quickly, which can help to efficiently determine a reasonable FGPF configuration for helmet design improvement. However, there is still no effective constitutive model available for FGPF materials.

To fill the above knowledge gap, this chapter is aimed to develop an effective analytical model to predict the mechanical responses of FGPF under uniaxial compression loads. This chapter is organized as follows. Section 4.2 introduces the density gradient strategy for FGPF. Then, Section 4.3 identifies an analytical constitutive model for the uniform density EPS foam subjected to uniaxial compression. Uniaxial quasi-static and dynamic compression experiments are carried out on EPS foams to validate the proposed compressive constitutive model. Section 4.4 further develops an analytical model to predict the stress-strain relations of FGPF subjected to uniaxial compressive loads, based

on which the validated FE models are employed to compare the analytical prediction and numerical simulation. Then, the orthogonal array design optimisation method was utilized to obtain the optimal configurations of FGPF with higher crashworthy performance. A comprehensive discussion of the results and limitations of this chapter is presented in Section 4.5. Finally, the research findings are concluded in Section 4.6.

4.2 Functionally graded polymeric foam

The energy absorption characteristics of FGPF subjected to uniaxial compression are investigated in this chapter. The direction of the FGPF density gradient coincides with that of the axial compression load (or thickness direction), as shown in Figure 4.1. The variation of FGPF density is defined in the following power-law functions,

$$\rho_f(x) = \rho_{f1} + (\rho_{f2} - \rho_{f1})\left(\frac{x}{T}\right)^n, \ \rho_{f1} < \rho_{f2}, \tag{4.1}$$

where ρ_{f1} and ρ_{f2} are the densities at the top and bottom ends of FGPF, respectively; x is the distance from the top end; T is the thickness of FGPF; n is the gradient exponent that governs the variation of foam densities, which usually varies between 0.1 to 10 [176-179, 205, 232, 233], as shown in Figure 4.2. It is practically difficult to manufacture a continuous FGPF according to Eq. (4.1). An approximate version of the continuous FGPF is the discrete FGPF, which is divided into a number of layers along the direction of the density gradient with each layer being assumed as a homogeneous and isotropic uniform foam material. As shown in Figure 4.1, based on the above-mentioned assumption, FGPF can be regarded as a combination of many independent foam layers (i.e. L_1, L_2, … …, L_i, … …, L_{z-1}, L_z) along with the gradient direction, and each of them has a different uniform density.
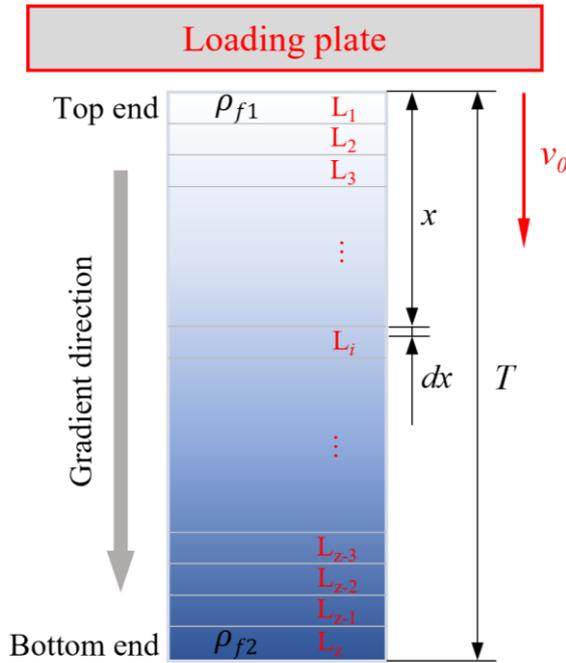
Figure 4.1. Schematic diagram of FGPF described by z foam layers with density varying along the gradient direction subjected to uniaxial compression
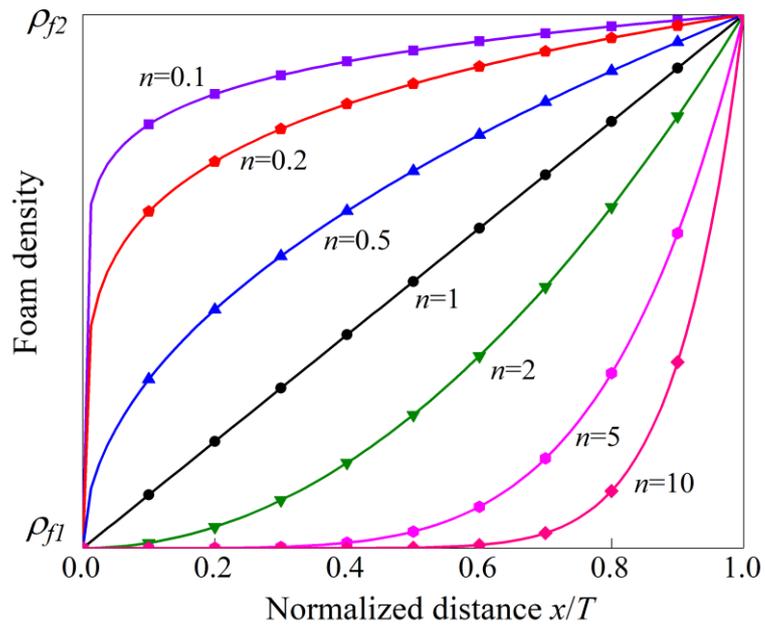
Figure 4.2. Variation in foam density versus normalized distance based on Eq. (4.1) for various n values between 0.1 and 10

4.3   Constitutive model

4.3.1   Constitutive model for uniform density polymeric foams

To determine the constitutive model for uniform density polymeric foams, the typical stress-strain curve of EPS foam under uniaxial compression is illustrated in Figure 4.3 where three phases of foam compression can be identified, i.e. initial linear elastic phase, plateau phase and densification phase. For the elastic phase, the stress increases linearly with the strain increasing to the yield strain (ε_y); then, the foam enters the plateau phase, in which the stress increases slightly; as the strain increases above the densification strain (ε_d), the foam enters the densification phase where the stress increased rapidly with strain. It should be noted that the transition between the three phases is over a small zone of strain, rather than instantaneously, due to the imperfection and non-homogeneity of the cellular foam. Assuming that the transition between the elastic phase and the plateau phase occurs over a zone of a strain of $2\Delta\varepsilon_y$, and the transition between the plateau phase and the densification phase occurs over a zone of a strain of $2\Delta\varepsilon_d$.
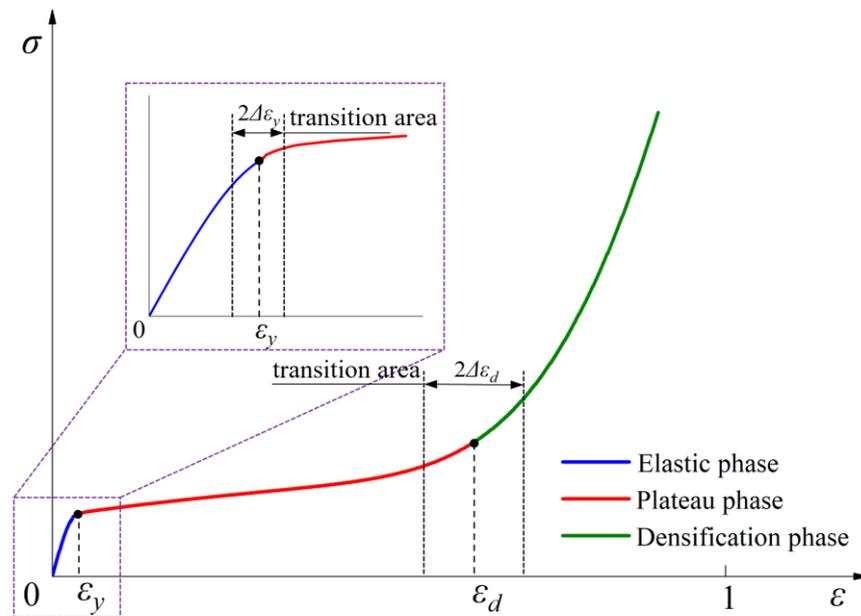
Figure 4.3. Typical stress-strain curve of EPS foam under uniaxial compression

According to [186], the Poisson's ratio of low-density polymeric foam is approximately zero, and the initial tangent modulus E_0 for the cellular EPS foam under uniaxial compression can be determined by

$$E_0 = A_0 E_s (\Phi_0)^2, \tag{4.2}$$

in which, the parameter, A_0 is a constant for the initial geometric stiffness, E_s is the tangent modulus of the solid matrix material of EPS foam, and Φ_0 is the initial relative density between EPS foam and its solid matrix material, expressed as

$$\Phi_0 = \frac{\rho_0}{\rho_s}, \tag{4.3}$$

where ρ_0 is the initial density of EPS foam, and ρ_s is the density of the matrix material of EPS foam.

For describing the characteristics of cellular foam under uniaxial compression, a constitutive model developed by Schraad and Harlow [187] is employed here. When EPS foam subjected to compression, both the geometric stiffness $A(\varepsilon)$ and the relative density $\Phi(\varepsilon)$ evolve with the compressive strain (ε). Therefore, Eq. (4.2) can be extended to describe the tangent modulus $E(\varepsilon)$ of EPS foam during compression, i.e.

$$E(\varepsilon) = A(\varepsilon) E_s [\Phi(\varepsilon)]^2, \tag{4.4}$$

where $\Phi(\varepsilon)$ is the current relative density given by

$$\Phi(\varepsilon) = \frac{\rho_0}{\rho_s} \frac{1}{1-\varepsilon}. \tag{4.5}$$

According to Eqs. (4.4) and (4.5), the compressive stress-strain relation of EPS foam can

be written as

$$\sigma(\varepsilon) = E(\varepsilon)\varepsilon = A(\varepsilon)E_s[\frac{\rho_0}{(1-\varepsilon)\rho_s}]^2\varepsilon, \tag{4.6}$$

in which $\sigma(\varepsilon)$ is the compression stress for EPS foam without consideration of the strain-rate effect.

As shown in Figure 4.3, three compressive phases and two transition zones for EPS foam subjected to compression can be observed. Based on the stress-strain characteristics of EPS foam, piecewise function is considered for the determination of the geometric stiffness $A(\varepsilon)$ in the constitutive model, i.e.

$$A(\varepsilon) = \begin{cases} A_0, & 0 \le \varepsilon < \varepsilon_y - \Delta\varepsilon_y \\ \frac{(A_0-A_1)\varepsilon-A_0(\varepsilon_y-\Delta\varepsilon_y)+A_1(\varepsilon_y+\Delta\varepsilon_y)}{2\Delta\varepsilon_y}, & \varepsilon_y - \Delta\varepsilon_y \le \varepsilon < \varepsilon_y + \Delta\varepsilon_y \\ A_1, & \varepsilon_y + \Delta\varepsilon_y \le \varepsilon < \varepsilon_d - \Delta\varepsilon_d, \\ \frac{(A_1-1)\varepsilon-A_1(\varepsilon_d-\Delta\varepsilon_d)+(\varepsilon_d+\Delta\varepsilon_d)}{2\Delta\varepsilon_d}, & \varepsilon_d - \Delta\varepsilon_d \le \varepsilon < \varepsilon_d + \Delta\varepsilon_d \\ 1, & \varepsilon_d + \Delta\varepsilon_d \le \varepsilon < 1, \end{cases} \tag{4.7}$$

where the A_0 and A_1 can be determined from Eqs. (4.2)-(4.5), given as

$$A_0 = \frac{E_0}{E_s(\Phi_0)^2} = \frac{E_0}{E_s}\left(\frac{\rho_s}{\rho_0}\right)^2, \tag{4.8}$$

$$A_1 = \frac{E_1}{E_s[\Phi(\varepsilon_y)]^2} = \frac{E_1}{E_s}\left(\frac{\rho_s}{\rho_0}\right)^2\left(1-\varepsilon_y\right)^2, \tag{4.9}$$

where E_1 is the tangent modulus of the plateau phase.

As described above, to determine the functions of the constitutive model of an EPS foam with a given density (ρ_0), these parameters, including E_s, ρ_s, $\Delta\varepsilon_y$, $\Delta\varepsilon_d$, ε_y, ε_d, E_0 and E_1, need to be determined, among them, the ε_y and E_1 are the calibrated parameters. For

the solid matrix material of EPS foam, both the tangent modulus (E_s = 3.3 GPa) and the density (ρ_s = 1050 kg/m^3) are constants in this study [234]. Regarding the transition zones, the values of $\Delta\varepsilon_y$ and $\Delta\varepsilon_d$ are set to be 0.01 and 0.03, respectively, to describe the gradual change of the compressive stress-strain magnitude in the transition zones. The onset strain of densification (ε_d) of the cellular foams is recommended in [186],

$$\varepsilon_d = 1 - 1.4 \left(\frac{\rho_0}{\rho_s}\right). \tag{4.10}$$

Because the initial tangent modulus (E_0) in the elastic phase exhibits approximately linear correlation with the initial density (ρ_0) of EPS foam [188, 235], the relationships between the initial tangent modulus (E_0) and the initial EPS foam density (ρ_0) can be determined on the basis of experimental data using liner fit method. The experimental data of EPS foams under uniaxial quasi-static compressions taken from the reported literature [165, 188, 236-243] and the testing results obtained in this chapter are employed here to determine the initial tangent modulus, as shown in Figure 4.4. The initial tangent modulus can be well described by the linear fit as

$$E_0 = 0.222\rho_0 - 0.281. \tag{4.11}$$

By definition, ε_y is the transition strain corresponding to the yield. Usually, the yield strain of EPS foam is less than 0.05 [186]. According to the literature [165, 188, 236-243] and the experimental data in Section 4.3.2, the yield strain (ε_y) of low-density EPS foam is in a small range of 0.02-0.04. The tangent modulus of the plateau phase (E_1) is estimated to be in the range of 0.05-0.40 according to experimental results [165, 188, 236-243], and the E_1 increases with the increase of the initial density of EPS foam. Noting that both ε_y and E_1 are used to calibrate the constitutive model, i.e. Eq. (4.6), using the reported data [165] and experimental results in Section 4.3.2, the calibrated

parameters for EPS foams with different densities are summarized in Table 4.1. Based on the results (Section 4.3.2 and Table 4.1) of the calibrated parameters, ε_y can be determined by

$$\varepsilon_y = \begin{cases} 0.025, & \rho_0 < 20 \\ 0.03, & \rho_0 \geq 20 \end{cases}, \tag{4.12}$$

where E_1 can be well described by a linear fit, as shown in Figure 4.5, which can be formulated as

$$E_1 = 0.0045\rho_0 + 0.0168. \tag{4.13}$$
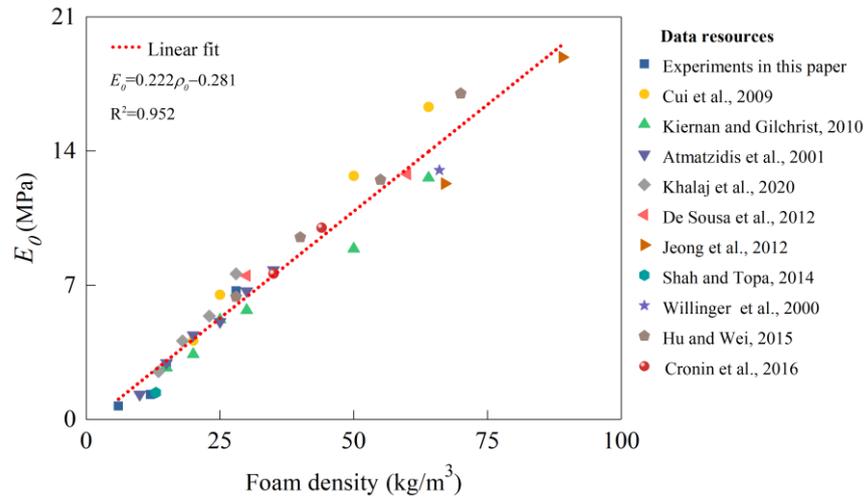
Figure 4.4. Correlation between initial tangent modulus and EPS foam density with a linear fit by Eq. (4.11)

Table 4.1. Calibrated parameters for the constitutive model of EPS foam

	EPS6	EPS12	EPS15	EPS20	EPS25	EPS28	EPS50	EPS64
ρ_0 (kg/m³)	6	12	15	20	25	28	50	64
E_1 (MPa)	0.05	0.07	0.08	0.09	0.13	0.16	0.25	0.30
ε_y	0.025	0.025	0.025	0.03	0.03	0.03	0.03	0.03

Note: Specimen label EPS6 denotes the EPS foam with a density of 6 kg/m³.
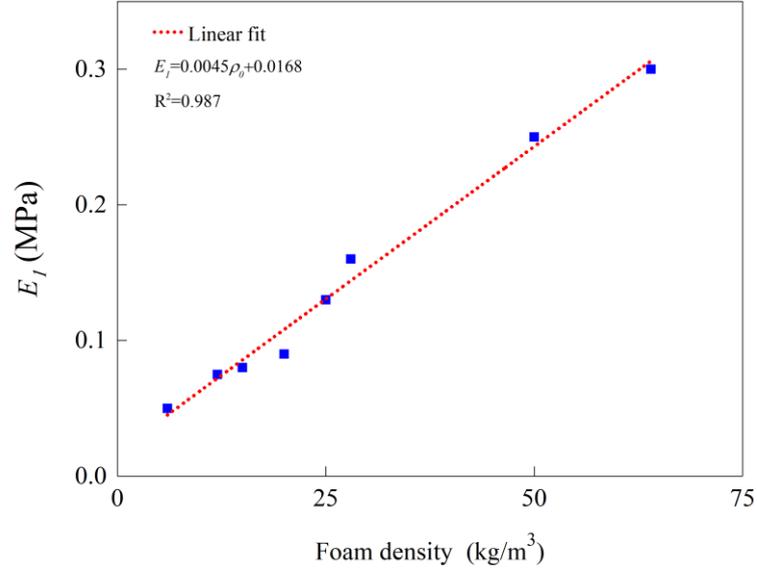
Figure 4.5. Correlation between tangent modulus of the plateau phase and EPS foam density with a linear fit by Eq. (4.13)

The strain-rate effects are further considered in the updated constitutive model using the compressive dynamic increase factor (DIF) [244], defined as

$$\sigma_d = DIF\sigma_s, \tag{4.14}$$

where σ_s represents a reference quasi-static rate-independent stress for EPS foam under compression, which can be obtained directly from Eq. (4.6); σ_d is the rate-dependent stress for EPS foam under compression. Noting that the DIF used in this chapter was obtained from the reported experimental studies on EPS foam with a density of 28 kg/m^3, as shown in Figure 4.6 [245]. The stresses at the compressive strains of 0.2 and 0.3 were employed to determine the DIF, which can be expressed as

$$DIF = \begin{cases} 1.2043 + 0.068\lg(\dot{\varepsilon}), & 0.001 \leq \dot{\varepsilon} \leq 112 \\ -1.4545 + 1.3641\lg(\dot{\varepsilon}), & \dot{\varepsilon} \geq 112 \end{cases}. \tag{4.15}$$

where the $\dot{\varepsilon}$ is the strain-rate. According to Eqs. (4.6) and (4.14), the compressive stress responses of EPS foam with the consideration of strain-rate effect can be expressed as

$$\sigma_d = A(\varepsilon)E_s\left[\frac{\rho_0}{(1-\varepsilon)\rho_s}\right]^2 \varepsilon DIF. \qquad (4.16)$$
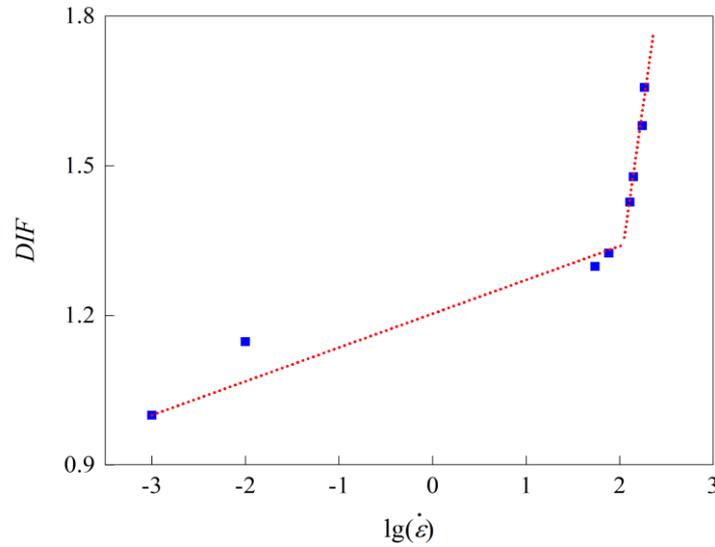
Figure 4.6. *DIF* versus logarithmic strain-rate relationship for EPS foam [245]

4.3.2 Experimental validation of the constitutive model

4.3.2.1 *Quasi-static compression test*

Experiments were carried out to calibrate the parameters, i.e. ε_y and E_1, in the constitutive model presented in Eq. (4.6) for EPS foams subjected to uniaxial quasi-static compression following Standard ASTM D1621-16 [246], as shown in Figure 4.7. Four densities of EPS specimens, including EPS6 (6 kg/m^3), EPS12 (12 kg/m^3), EPS15 (15 kg/m^3) and EPS28 (28 kg/m^3) with the same geometrical configurations of Length × Width × Depth = 60 mm × 60 mm × 50 mm, were selected here for the experiments. Quasi-static compression tests were performed using the universal testing machine Zwick/Roell Z010. The EPS specimens were compressed by the top platen at a constant crosshead speed of 0.05 mm/s, corresponding to a quasi-static strain-rate of 0.001 s^{-1}, and the maximum loading displacement was set to be 40 mm, corresponding to a strain of 0.8. The identical EPS specimens were tested three times to ensure the accuracy and repeatability of experimental results.
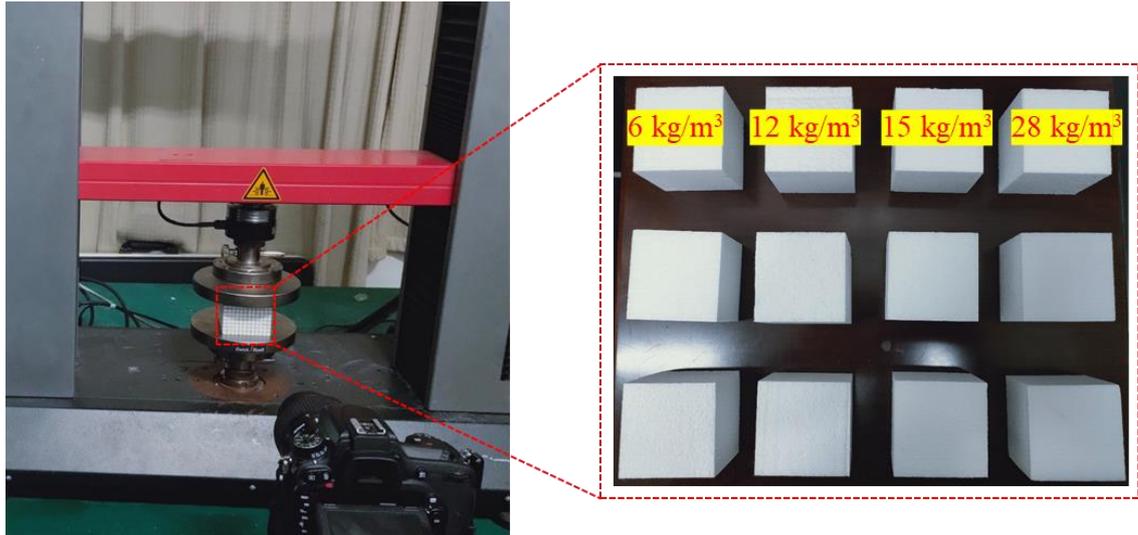
Figure 4.7. EPS specimens with four densities subjected to uniaxial quasi-static compressions

All experimental results for the EPS specimens under uniaxial quasi-static compressions are compared with the model predictions based on Eq. (4.6), as shown in Figure 4.8. According to the experimental results, excellent repeatability could be found for each density grade of EPS foam. It also can be observed that all model-predicted curves with the calibrated parameters, i.e. ε_y and E_1 listed in Table 4.1, almost coincided with their corresponding experimental results, which indicates the accuracy of the constitutive model for EPS foams. To achieve a more comprehensive calibration with a larger range of EPS foam densities, the constitutive model is further calibrated by four more uniaxial quasi-static compression experiments, which are reported in the reference [165]. As shown in Figure 4.9, the model predictions with the calibrated parameters for EPS foams under uniaxial quasi-static compressions show good agreement with the reported experimental results in [165]. In general, the constitutive model presented in Eq. (4.6) can well represent the compressive behaviours of EPS foam.
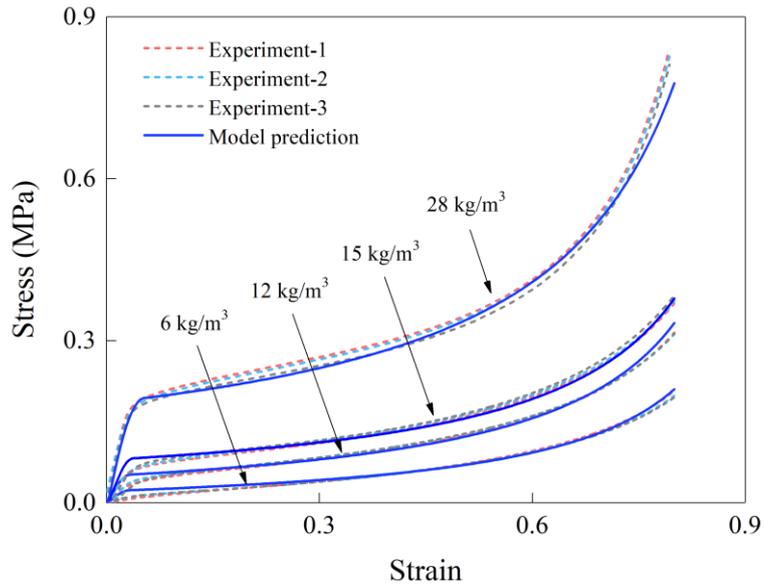
Figure 4.8. Comparison between the experimental results and constitutive model predictions in Eq. (4.6) for EPS foams with four densities under uniaxial quasi-static compressions
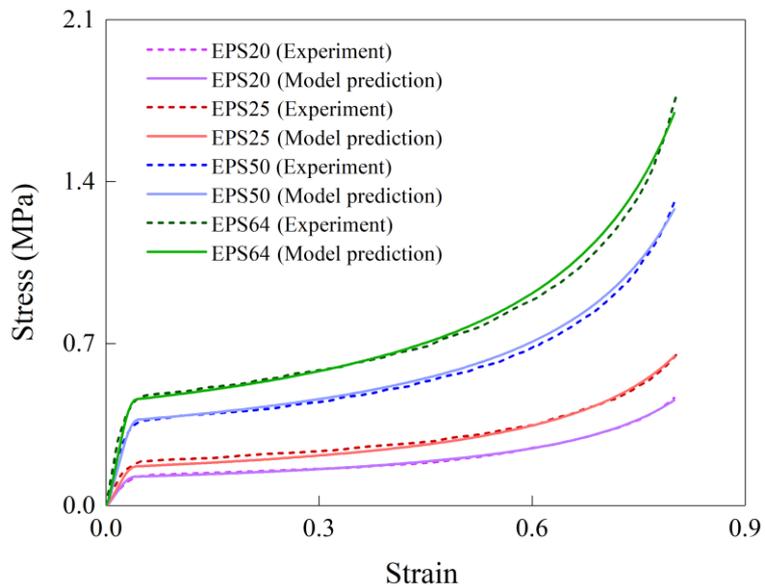
Figure 4.9. Comparison between the experimental data in Table 4.1 and analytical model predictions in Eq. (4.6) for EPS foams under uniaxial quasi-static compressions [165]

4.3.2.2   *Dynamic compression test*

To further validate the constitutive model for EPS foams subjected to high strain-rate compressions, the dynamic uniaxial compression tests were conducted using the drop tower impact system INSTRON 9250HV, as shown in Figure 4.10. The drop weight of

28.5 kg with an impact velocity of 4.2 m/s was adopted for the dynamic tests. The strain-rate applied here was idealised as a constant strain-rate, $\dot{\varepsilon} = 84$ s^{-1}, due to the reduction of impact velocity less than 10% when the compressive strain is less than 0.8. Three identical EPS specimens, with the geometries of Length × Width × Depth = 60 mm × 60 mm × 50 mm and a density of 28 kg/m^3, were selected here for the tests.

Figure 4.10. EPS specimens subjected to uniaxial dynamic compression

Three identical 28 kg/m^3 EPS specimens under uniaxial dynamic compression experiments and the dynamic compressive responses predicted by the constitutive model in Eq. (4.16) are compared in Figure 4.11. It can be found that the dynamic experimental results are of good repeatability and show good agreement with the model predictions. According to a range of experimental results in Figure 4.8, Figure 4.9 and Figure 4.11, the constitutive models presented in Eqs. (4.6) and (4.16) can well describe the responses of EPS foam subjected to uniaxial quasi-static and dynamic compressions. With the increase in foam density or compressive strain-rate, both the elastic phase and the initial tangent

modulus of EPS foam increase, leading to the improvement of the compression stress.
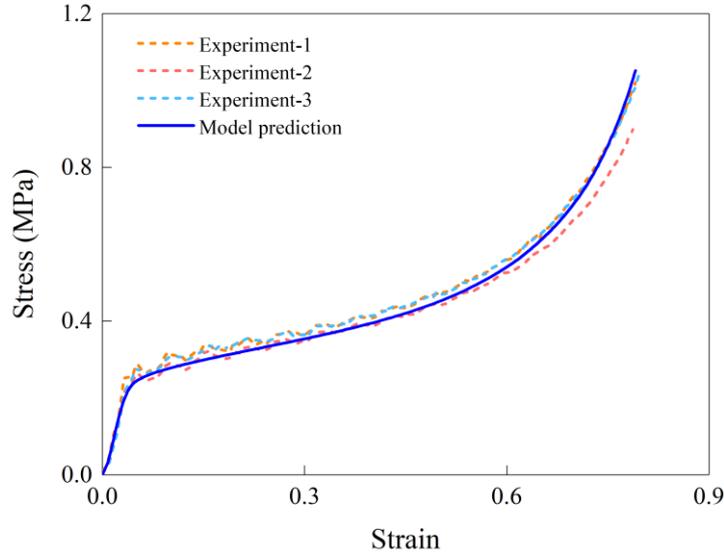
Figure 4.11. Rate-dependent constitutive model in Eq. (4.16) validated by the 28 kg/m^3 EPS specimens under uniaxial dynamic compression experiments

4.4   Analytical model and optimisation study for FGPF

4.4.1   Analytical model for FGPF under uniaxial compression

In this section, the analytical model was developed to predict the stress-strain response of FGPF under uniaxial compression. As shown in Figure 4.1, FGPF is a combination of multiple foam layers, such as L_1, L_2, ……, L_i, ……, L_{z-1}, L_z, in the gradient direction and each layer has a uniform density, the compressive constitutive model for the uniform density foam can be used in FGPF analytical model. Since the load-carrying capacity of EPS foam depends on the long plateau phase of EPS foam under compression, the stress-strain relation of each foam layer is idealised as a rigid-perfectly plastic-locking (R-PP-L) model [247], which neglects the plastic hardening in the plateau phase. The idealised R-PP-L model is illustrated in Figure 4.12, in which $\rho_f^{L_i}$ for each $i \in (1, \ldots \ldots, z)$ is the density of the corresponding foam layer of FGPF; $\sigma_y^{L_i}$ and $\varepsilon_d^{L_i}$ respectivley denote the yield stress and the onset strain of densification of the corresponding foam layer of L_i.

The methods to determine $\sigma_y^{L_i}$ and $\varepsilon_d^{L_i}$ will be given later in this section.
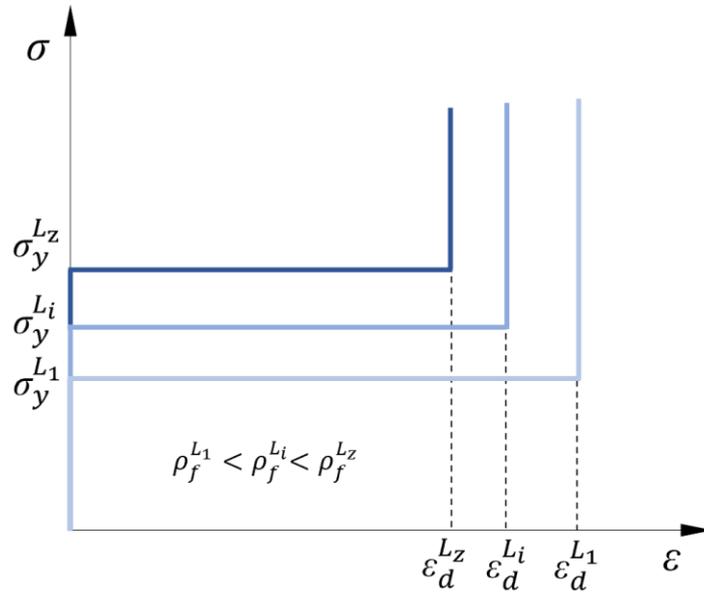
Figure 4.12. Idealised rigid-perfectly plastic-locking model for the independent foam layers with various densities, plateau stresses and onset strains of densification under uniaxial compression load

With the increment of the density of each foam layer (L_i), from the top end to the bottom end of FGPF, the onset strain of densification of the foam layer decreases and the corresponding yield stress increases, as shown in Figure 4.12. Therefore, FGPF subjected to the uniaxial compression load can deform from the top end to the bottom end of FGPF, which follows the layer-by-layer progressive compressive deformation model. More specifically, when the yield stress reaches $\sigma_y^{L_1}$, FGPF deformation is firstly occur in the topmost foam layer (L_1) of FGPF, and then the foam layer of L_1 is continually compressed to its densification phase ($\varepsilon_d^{L_1}$). With the the increase of the yield stress from $\sigma_y^{L_1}$ to $\sigma_y^{L_2}$, the second foam layer (L_2) of FGPF starts to deform till its densification phase ($\varepsilon_d^{L_2}$). The rest of FGPF foam layers are deformed layer-by-layer in the same manner with the continuation of the compression.

As assumed above, the stress-strain relations of FGPF (σ_F) can be determined by the current yield stress ($\sigma_y^{L_i}$) of each foam layer, viz.

$$\sigma_F = \sigma_y^{L_i}, \ \varepsilon_d^{L_{i-1}} \leq \varepsilon < \varepsilon_d^{L_i}, \tag{4.17}$$

where $\varepsilon_d^{L_0} = 0$ and $i \in (1, \ldots \ldots, z)$. Based on the model proposed by Gibson and Ashby [186], the yield stress of the i-th foam layer is

$$\sigma_y^{L_i} = 0.3\sigma_{yS} \left(\varphi \frac{\rho_f^{L_i}}{\rho_s} \right)^{\frac{3}{2}} + 0.4\sigma_{yS} \left[(1 - \varphi) \frac{\rho_f^{L_i}}{\rho_s} \right], \tag{4.18}$$

in which, the $\rho_f^{L_i} = \rho_f(x)$ is the density of the i-th foam layer; the volume fraction of the solid contained in the cell edges $\varphi = 0.9$ and the yield stress of the matrix material of the polymeric foam $\sigma_{yS} = 135$ MPa [234]. The experimental results presented in Figure 4.8 and Figure 4.9 were used to compare the corresponding model prediction from Eq. (4.18), as shown in Figure 4.13. In addition, the absorbed energy (W)

$$W = \int_0^\varepsilon \sigma_F(\varepsilon)d\varepsilon, \tag{4.19}$$

which was calculated and compared with experimental results in presented Figure 4.8 and Figure 4.9, as shown in Figure 4.14 and Table 4.2. It could be found from Table 4.2 that the maximum relative difference of the energy absorption between Eq. (4.18) and experimental measurement is 22.9% for the very low-density foam EPS6. For other EPS foams with a larger density, the relative differences of energy absorption are less than 13.1%. Therefore, Eq. (4.18) can be used to describe the compressive yield stress for each layer of EPS foam.
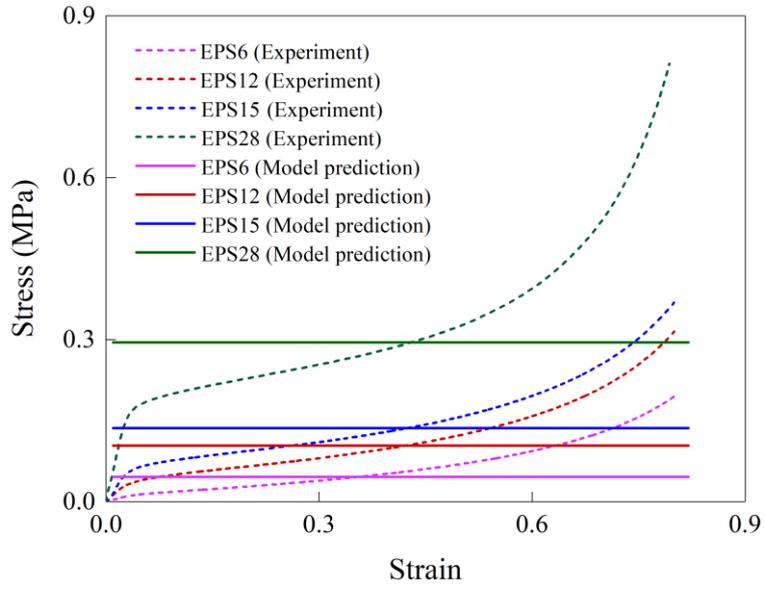
(a)
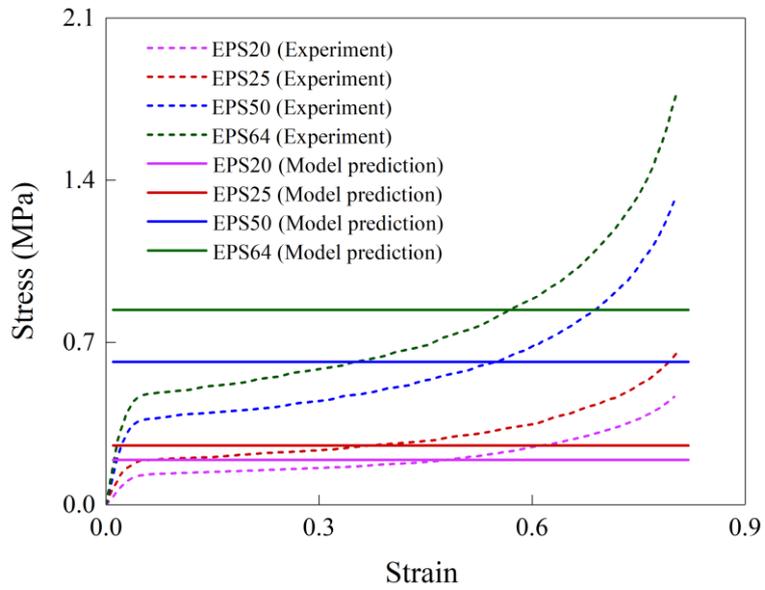
(b)

Figure 4.13. Comparison between the experimental results in Table 4.1 and the predictions in Eq. (4.18) for EPS foam compression yield stress, (a) compare with the experimental results selected from Figure 4.8, (b) compare with the experimental results selected from Figure 4.9
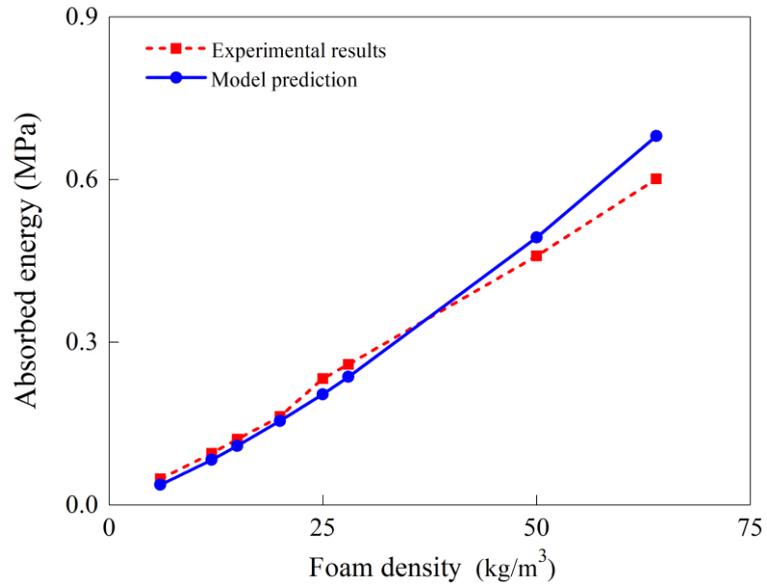
Figure 4.14. The absorbed energies for both the experimental results presented in Figure 4.8 and Figure 4.9 and the model prediction in Eq. (4.18)

Table 4.2. Comparison of the absorbed energies for both the experimental results and the prediction in Eq. (4.18) for EPS foams

	EPS6	EPS12	EPS15	EPS20	EPS25	EPS28	EPS50	EPS64
Experiment (MPa)	0.048	0.095	0.121	0.163	0.233	0.259	0.459	0.601
Model prediction (MPa)	0.037	0.083	0.109	0.155	0.204	0.236	0.493	0.680
Absolute Error (%)	-22.9	-12.6	-9.9	-4.9	-12.4	-8.9	7.4	13.1

According to Eqs. (4.1) and (4.10), the onset strain of densification for the independent foam layers can be obtained from

$$\varepsilon_d^{L_i} = 1 - 1.4\left(\frac{\rho_f^{L_i}}{\rho_s}\right). \tag{4.20}$$

The overall strain of FGPF is defined as

$$\varepsilon_F = \frac{\Delta_F}{T}, \tag{4.21}$$

where Δ_F is the overall compressive displacement for FGPF, which can be calculated by integrating the compressed strain for each foam layer, i.e.

$$\Delta_F = \int_0^x \varepsilon_d^{L_i} dx. \tag{4.22}$$

Substitution of Eqs. (4.1) and (4.20) into Eq. (4.22),

$$\Delta_F = \int_0^x \left\{ 1 - 1.4 \left[\frac{\rho_{f1} + (\rho_{f2} - \rho_{f1})\left(\frac{x}{T}\right)^n}{\rho_s} \right] \right\} dx = \left(1 - 1.4 \frac{\rho_{f1}}{\rho_s} \right) x - 1.4 \frac{(\rho_{f2} - \rho_{f1})}{(n+1)\rho_s T^n} x^{n+1}. \tag{4.23}$$

According to Eqs. (4.21) and (4.23), the relation between the overall strain (ε_F) and the distance from the top end (x) of FGPF can be determined by

$$-1.4 \frac{(\rho_{f2} - \rho_{f1})}{(n+1)\rho_s T^n} x^{n+1} + \left(1 - 1.4 \frac{\rho_{f1}}{\rho_s} \right) x - T\varepsilon_F = 0. \tag{4.24}$$

As shown in Figure 4.2, the typical gradient exponent value of n varies between 0.1 to 10, each specific value of n can result in one specific equation, and Eq. (4.24) can be quadratic, cubic, quartic, or other high-order equations. The solution of Eq. (4.24) can be obtained once the value of n is given. To facilitate the understanding of the following development of the analytical model, the specific gradient exponent, $n = 1$, was selected here as an example. When $n = 1$, Eq. (4.24) can be rewritten as

$$-0.7 \frac{(\rho_{f2} - \rho_{f1})}{\rho_s T} x^2 + \left(1 - 1.4 \frac{\rho_{f1}}{\rho_s} \right) x - T\varepsilon_F = 0. \tag{4.25}$$

Then, the solution of Eq. (4.25) can be determined as

$$x = \frac{\rho_s - 1.4\rho_{f1} - \sqrt{(\rho_s - 1.4\rho_{f1})^2 - 2.8(\rho_{f2} - \rho_{f1})\rho_s \varepsilon_F}}{1.4(\rho_{f2} - \rho_{f1})/T}. \tag{4.26}$$

According to Eqs. (4.1), (4.17), (4.18) and (4.26), the stress-strain relation of FGPF under uniaxial compression can be obtained as

$$\sigma_F(\varepsilon_F) = 0.1546\sigma_{yS} \left[1 - \frac{1}{\rho_s}\sqrt{(\rho_s - 1.4\rho_{f1})^2 - 2.8(\rho_{f2} - \rho_{f1})\rho_s \varepsilon_F} \right]^{3/2} +$$

$$0.0286\sigma_{yS} \left[1 - \frac{1}{\rho_s}\sqrt{(\rho_s - 1.4\rho_{f1})^2 - 2.8(\rho_{f2} - \rho_{f1})\rho_s \varepsilon_F} \right]. \tag{4.27}$$

When the *DIF* is taken into consideration in Eq. (4.27), the rate-dependent stress-strain relations $\sigma_F^d(\varepsilon_F)$ can be given by

$$\sigma_F^d(\varepsilon_F) = 0.155\sigma_{yS} \left[1 - \frac{1}{\rho_s}\sqrt{(\rho_s - 1.4\rho_{f1})^2 - 2.8(\rho_{f2} - \rho_{f1})\rho_s \varepsilon_F} \right]^{3/2} DIF +$$

$$0.029\sigma_{yS} \left[1 - \frac{1}{\rho_s}\sqrt{(\rho_s - 1.4\rho_{f1})^2 - 2.8(\rho_{f2} - \rho_{f1})\rho_s \varepsilon_F} \right] DIF. \tag{4.28}$$

It should be noted that the analytical models of FGPF subjected to uniaxial compression loading were derived from the quasi-static to low-speed dynamic uniaxial compressions, in which the compaction shock does not happen [248]. Therefore, the proposed analytical models are only applicable under the loading conditions of low to moderate strain-rates ($10^{-3} \sim 10^2$ s^{-1}) [249].

4.4.2   FE modelling validation of the analytical model

4.4.2.1   FGPF FE model description

To validate the analytical model of FGPF subjected to uniaxial compression loads, the finite element model of FGFP was developed using commercial FE code LS-DYNA 971. FGPF considered herein is a square column with the geometrical configuration, Length × Width × Depth = 60 mm × 60 mm × 50 mm, which is the same as the uniform density EPS

specimens. As illustrated in Figure 4.15, the FGPF column is placed on a fixed rigid platen and compressed by the upper rigid platens at a constant impact velocity. Both the moving and fixed platens were simulated using the rigid material model *MAT_20: RIGID and the Belytschko-Tsay shell element. The material properties of rigid platens were listed as follows, density = 7850 kg/m^3, Young's modulus = 210 GPa, Poisson's ratio = 0.33. FGPF column is divided into 20 layers along the direction of density gradient where each layer of FGPF is assumed as a homogeneous and isotropic uniform density EPS foam. The material model *MAT_57: LOW_DENSITY_ FOAM and constant stress solid element were adopted to simulate the highly compressible EPS foam [250]. The material properties for each layer of FGPF with a given foam density can be determined from Section 4.3.1. As shown in Figure 4.16, mesh sizes of 2.5mm and 1.25 mm were selected for the shell and solid elements, respectively, based on the convergence analysis. The 'SURFACE_TO_SURFACE' contact was defined with the static and kinetic coefficients of friction of 0.02 for modelling the interfaces between FGPF and two rigid platens [251].
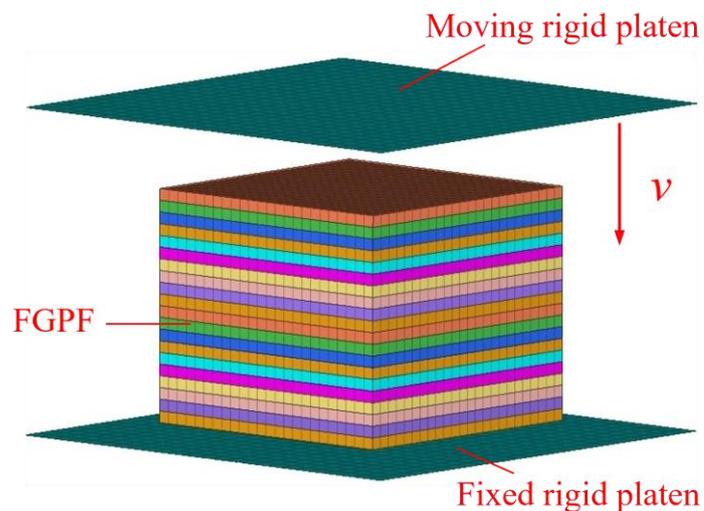
Figure 4.15. FGPF model subjected to axial compression simulation
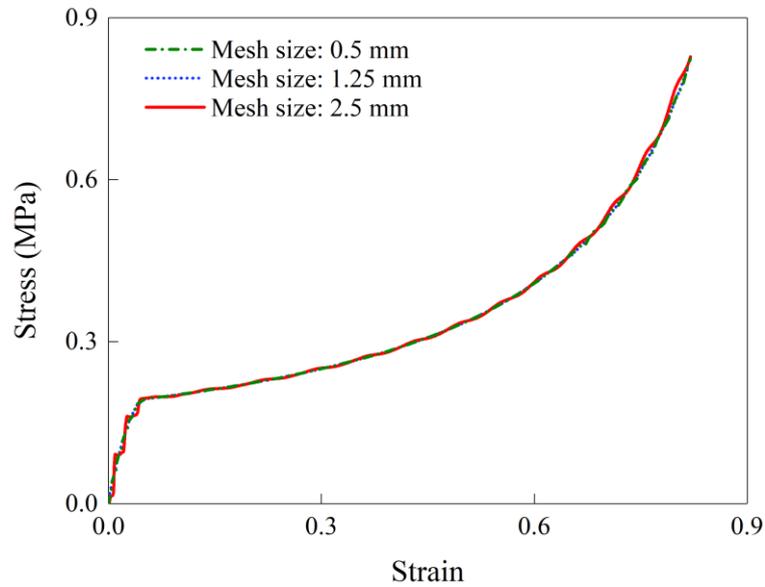
Figure 4.16. Convergence analysis on mesh sizes

4.4.2.2   *Validation of the FE model*

It can be found from Eq. (4.1) that FGPF will be changed into a uniform density foam when the gradient exponent $n = 0$, and the uniform density foam could be regarded as a special case of FGPF. Therefore, it is reasonable to validate the FE model of FGPF by using the uniform density foam under uniaxial compression experiments. The experimental results of 28 kg/m^3 EPS foam presented in Figure 4.8 and Figure 4.11 are used to validate the FGPF FE model. As shown in Figure 4.17, the experimental and numerical deformation histories for the 28 kg/m^3 EPS foam subjected to uniaxial quasi-static compression were presented with a compressive strain increment of 0.2. Furthermore, the experimental and numerical stress-strain curves for quasi-static and dynamic compressions are compared in Figure 4.18. All experimental results are in good agreement with the numerical results, demonstrating the validity of the FGPF FE model.
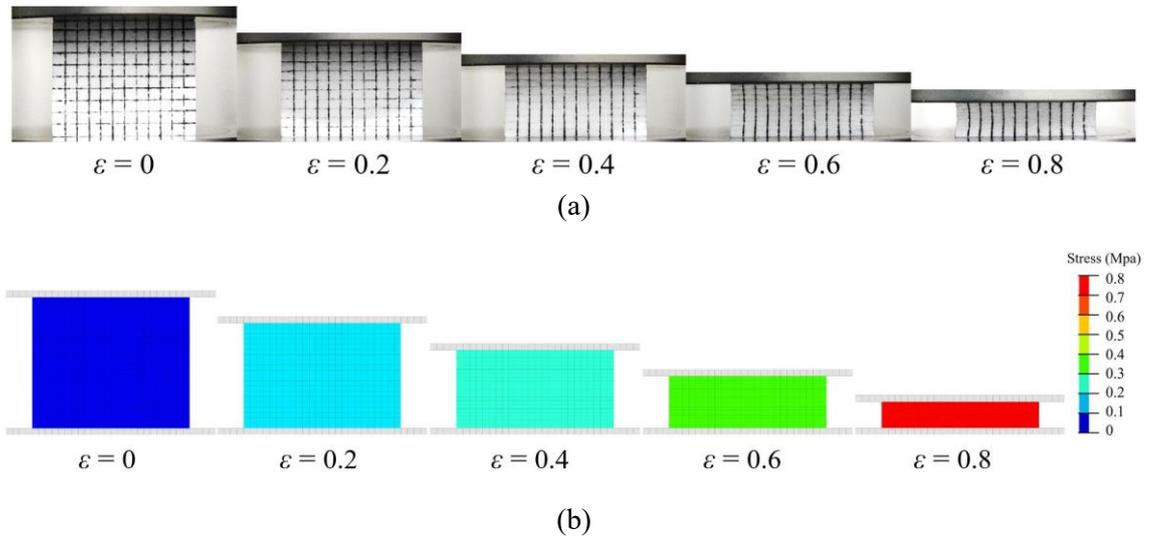
Figure 4.17. Comparison of experimental and numerical deformation histories for 28 kg/m³ EPS foam under uniaxial quasi-static compression, (a) experimental results, (b) numerical results
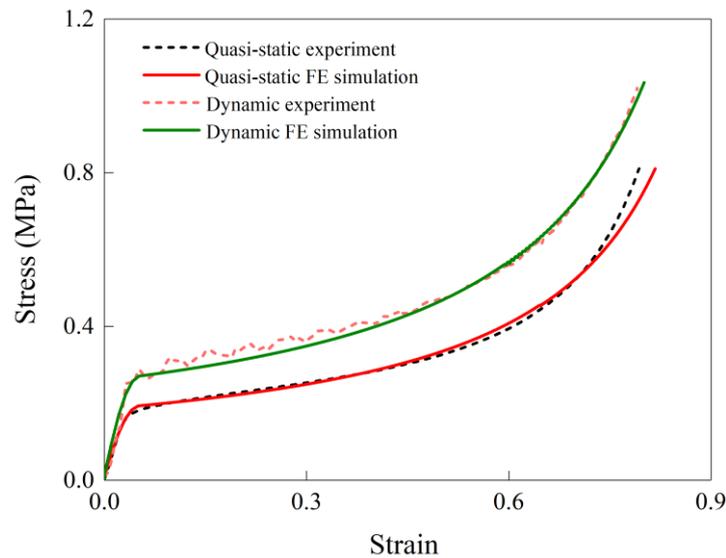
Figure 4.18. Finite element model for FGPF validated by quasi-static and dynamic uniaxial compression experiments

4.4.2.3   *Validation of FGPF analytical model using FE models*

According to Eqs. (4.27) and (4.28), the rate-independent and rate-dependent compressive responses of FGPF can be predicted once the densities at the top and bottom end of FGPF are determined. The analytical model predictions for the compressive stress-strain responses of a specific FGPF ($n = 1$, $\rho_{f1} = 10$ kg/m³ and $\rho_{f2} = 110$ kg/m³) subjected to quasi-static and dynamic loads ($\dot{\varepsilon} = 0.001$ s⁻¹ and 100 s⁻¹) and their

corresponding FE simulations are compared in Figure 4.19(a), and the absorbed energies of FGPF are plotted in Figure 4.19(b). It can be found from Figure 4.13 that there are noticeable differences between FE numerical results and analytical predictions, caused mainly by using an idealised R-PP-L model for each foam layer in the analytical model. In general, the analytical model in Eqs. (4.27) and (4.28) can give reasonable predictions of the compressive stress-strain relations of FGPF under uniaxial compression loads.
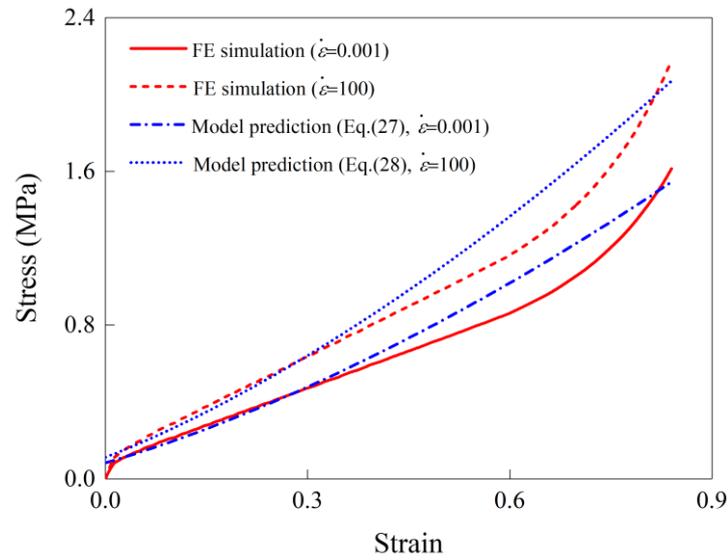
(a)
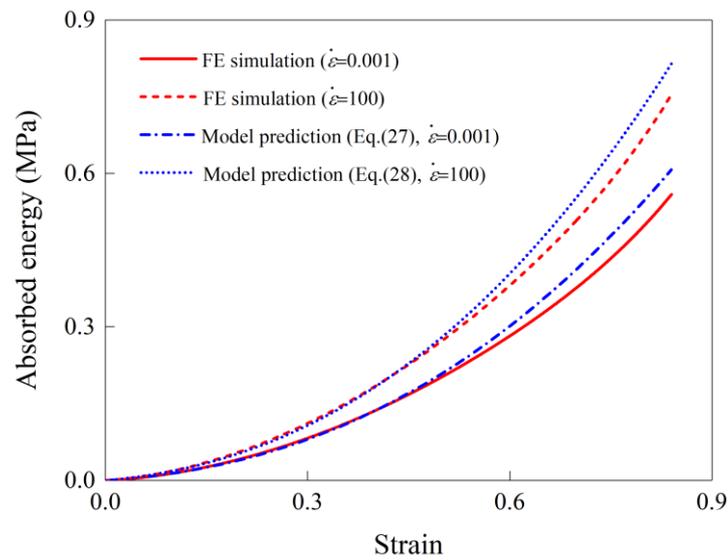
(b)

Figure 4.19. Comparison between the FE simulations and analytical model predictions of FGPF under compression loads, (a) compressive stress responses, (b) absorbed energy responses

4.4.3   Design Optimisation for FGPF under uniaxial compression

FGPF can be widely used as an energy-absorbing structure due to its excellent and designable impact attenuation and energy-absorbing capacities, and optimisation studies are usually conducted to achieve the best crashworthy performance for energy-absorbing structures [165, 180]. Since the compressive responses of FGPF can be determined by three parameters, i.e. the gradient exponent (n) and foam densities at the top and bottom ends (ρ_{f1} and ρ_{f2}), the optimal configuration of FGPF under uniaxial compression is studied here using an orthogonal array design optimisation method (see Section 3.4.1) and the validated FE model presented in Figure 4.15.

For achieving the optimal configuration for the crashworthiness of FGPF, the gradient exponent and foam densities at the top end and bottom end were adopted as the three discrete design variables for FGPF. Each design variable has seven levels, as listed in Table 4.3. Specific energy absorption (SEA), which is defined as the energy absorption per unit mass of the structure, is usually considered the most common and critical criterion for structural crashworthiness. Therefore, the SEA defined by

$$SEA = \frac{\int_0^d F(x)dx}{m}, \tag{4.29}$$

is chosen as the design objective for optimisation, where d is the structural deflection, $F(x)$ is the impact-resistant force and m is the mass of FGPF. The optimisation problem for FGPF can be defined as

$$\begin{cases} R = \text{Maxmize: } SEA\big(n, \rho_{f1}, \rho_{f2}\big) \\ \text{s.t.} \begin{cases} n \in (0.1, 0.2, 0.5, 1, 2, 5, 10) \\ \rho_{f1} \in (10, 15, 20, 25, 30, 35, 40) \\ \rho_{f2} \in (80, 85, 90, 95, 100, 105, 110) \end{cases} \end{cases} \tag{4.30}$$

Table 4.3. The discrete values of design variables for FGPF

Description	1	2	3	4	5	6	7
n	0.1	0.2	0.5	1	2	5	10
ρ_{f1} (kg/m³)	10	15	20	25	30	35	40
ρ_{f2} (kg/m³)	80	85	90	95	100	105	110

Based on Table 3.5 and Table 4.3, the levels for design variables and the results in the first iteration are obtained and presented in Table 4.4. According to the results of SEA, ANOM method (Table 3.6) was employed to find the optimum design in the first iteration, as shown in Table 4.5. Specifically, the maximum/optimal values of the mean of SEA for each design variable in the first iteration can be found from Table 4.5, such as 8.58 for n at the Level 1 (i.e. $n = 0.5$, see Table 3.5 and Table 4.4), 8.52 for ρ_{f1} at the Level 3 (i.e. $\rho_{f1} = 30$ kg/m³), and 8.48 for ρ_{f2} at the Level 1 (i.e. $\rho_{f2} = 90$ kg/m³). Thus, the levels ($n = 0.5$, $\rho_{f1} = 30$ kg/m³ and $\rho_{f2} = 90$ kg/m³) were assigned to the new second level of each design variable for the second optimisation iteration, see Figure 3.18.

Table 4.4. The discrete values of design variables in the first iteration

No.	Levels of design variables			m (g)	SEA (J/g)
	n	ρ_{f1} (kg/m³)	ρ_{f2} (kg/m³)		
1	0.5	20	90	12.01	8.55
2	0.5	25	95	12.91	8.58
3	0.5	30	100	13.81	8.61
4	1	20	95	10.35	8.36
5	1	25	100	11.25	8.40
6	1	30	90	10.80	8.53
7	2	20	100	8.40	8.09
8	2	25	90	8.40	8.35
9	2	30	95	9.30	8.42

Table 4.5. Mean of *SEA* corresponding to each level in the first iteration

Design variables	Levels of design variables		
	1	2	3
n	**8.58**	8.43	8.29
ρ_{f1}	8.34	8.44	**8.52**
ρ_{f2}	**8.48**	8.46	8.37

The convergence history of *SEA* for the FGPF optimisation is shown in Figure 4.20. The details of initial and optimum designs for FGPF under uniaxial compression are summarized in Table 4.6. It can be found that the *SEA* increases from 8.03 J/g to 8.79 J/g after three optimisation iterations, representing a 9.46% increase from the initial design of FGPF. The optimisation convergence criterion is satisfied at the seventh iteration, as shown in Figure 4.20.
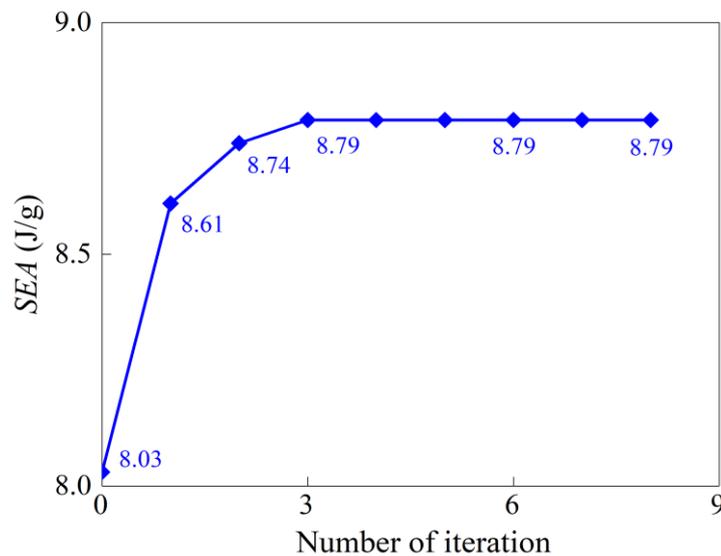
Figure 4.20. The iteration process of discrete optimisation for FGPF

Table 4.6. Comparison of the initial and optimum designs for FGPF

Description	n	ρ_{f1} (kg/m³)	ρ_{f2} (kg/m³)	m (g)	*SEA* (J/g)
Initial design	1	10	110	10.80	8.03
Optimum design	0.1	35	85	14.49	8.79

4.5 Discussion

This chapter first develops the analytical model to characterise the compression behaviours of FGPF under uniaxial quasi-static and dynamic loading conditions. In reported literature [165, 183, 252-254], the more general functionally graded foam (FGF) materials can be defined by a power-law function, which can be governed by five parameters, i.e. x, T, n, ρ_{f1} and ρ_{f2}, as presented in Eq. (4.1). To characterise the compression behaviours of FGF, the FE simulation was employed in previous studies [165, 183, 252-254] by considering the continuous FGF as a combination of numerous discrete UDF layers with different densities. In this study, the continuous characteristics of FGPF were considered in the analytical model by using the integrating method, as presented in Eqs (4.22) and (4.23). The proposed analytical model also allows us to determine the compression behaviours of FGPF using only three key parameters, i.e. n, ρ_{f1} and ρ_{f2}, as presented in Eqs. (4.27) and (4.28).

To achieve the optimal configuration for the crashworthiness of FGPF, the optimisation study was also carried out in this study. After several optimisation iterations, the SEA of FGPF has increased by 9.46%, which is not a large improvement from the aspect of energy-absorbing capacity of potential advanced material for the helmet liner foam. However, the helmet protection performance is not fully determined by the improvement of the energy-absorbing capacity of the liner foam. As mentioned in Section 2.3.2, the use of FGPF can offer more designable space to compensate the negative effect of the excessive stiffness of the advanced composite helmet shell to improve helmet protection [12, 199]. Furthermore, according to the helmet standards [19, 20, 22], the performance of helmet protection should be evaluated by helmeted headform responses, rather than by the energy-absorbing capacity of the helmet.

According to a study on the dynamic behaviours of FGF material under ball impacts

reported by Zhang and Zhang [180], although the energy absorption for the optimal FGF design did not experience a significant increase, the peak impact force transmitted to the ball can be considerably decreased and the impact duration can also be prolonged. In comparison with the uniform density foam, FGF with a linear decreasing density gradient can lead to a smaller deformation depth (Figure 4.21), which can provide more surviving or buffer space for protected objects [180]. It implies that FGF with a decreasing density gradient design can offer better protectability to the protected objects. This finding is in line with the studies reported by Cui et al. [27, 165], who found that the efficiency of material usage can be improved by using a FGF with a higher inner liner density and a lower outer liner density. They also concluded that a reasonable design of FGF for the helmet liner can help in reducing the peak linear acceleration transmitted to the headform.
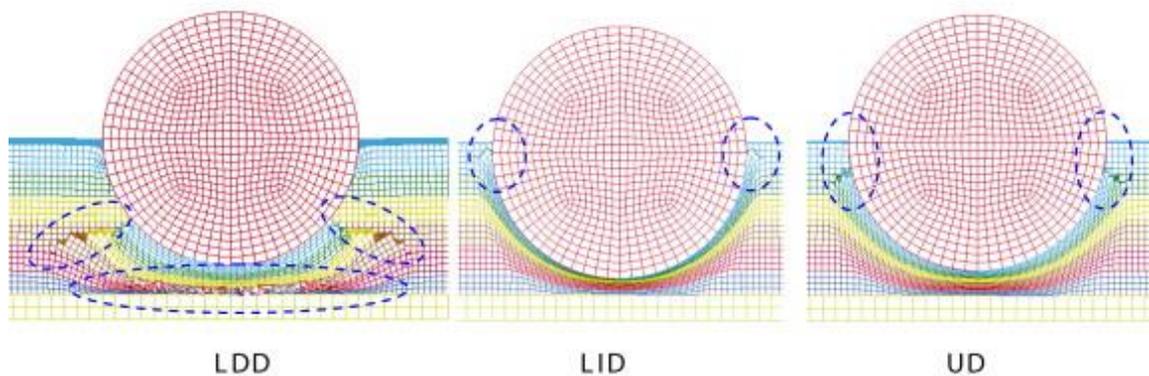
Figure 4.21. The rigid ball striker impacts the FGF materials with linear decreasing density (LDD), linear increasing density (LID) and uniform density (UD) gradients [180]

Based on the above analysis, although the energy-absorbing capacity of FGPF cannot be largely improved, the protection performance of a helmet with a reasonable FGFP design can be significantly improved by prolonging the impact duration and reducing the impact load/acceleration transmitted to the human head. In addition, FGPF with a decreasing gradient is recommended for the helmet liner, in which the foam density decreases from the inner surface (contact to head) to the outer surface (contact to helmet outer shell). The

analytical model proposed in this chapter can provide a quick prediction of the compression behaviours of FGPF for the helmet liner design, whereas the detailed recommendation of FGPF parameters for the helmet liner cannot be provided before a further systematic study.

This study has some limitations. Firstly, the developed analytical models for FGPF under compression loads were only validated against the corresponding numerical simulations, whereas the experimental validation is still lacking. Secondly, since this thesis aims to improve helmet design to reduce head injury in accidents, it is significant to further explore the practical usage of FGPF in the helmet liner. Thus, the high biofidelity head models are recommended to couple with FGPF to study the influences of FGFP on the head impact responses. Furthermore, based on the head-helmet modelling method presented in **Chapter 3**, FGPF can be also directly introduced to the helmet liner to find the optimal FGPF configuration for the improvement of helmet design. Finally, the temperature effect on the mechanical characteristics of FGPF needs to be considered, since the helmet may be used over a wide range of temperatures and FGPF design must assure helmet protection performance in the temperature range of the applications.

4.6   Conclusions

In this chapter, the compressive constitutive model for uniform-density EPS foam was developed and calibrated by experimental data. The constitutive model can well represent the behaviours of polymeric foam under uniaxial compression loads. Based on the idealised rigid-perfectly plastic-locking model, an analytical model was established to predict the responses of FGPF under uniaxial compressions. In this method, three parameters including gradient exponent and foam densities at the top and bottom ends of FGPF can determine the analytical model for the compressive response of FGPF. The

FGPF analytical model with a specific gradient exponent, $n = 1$, was selected in this chapter as an example. The analytical model prediction of a specific FGPF ($n = 1$, $\rho_{f1} = 10 \, \text{kg/m}^3$ and $\rho_{f2} = 110 \, \text{kg/m}^3$) was obtained and validated by the numerical simulations. The comparisons between analytical predictions and numerical results demonstrated that the proposed analytical model could effectively predict the compressive responses of FGPF. The analytical model is limited to low to moderate strain-rates when no compaction shock occurs. Based on the discrete optimisation study, SEA of FGPF was increased by 9.46%. The proposed analytical method can be exploited to further investigate the compressive responses of other functionally graded foam materials. This analytical model can also quickly predict the compressive responses and impact characteristics of FGPF, which can help to improve the efficient design of helmet protection from the material level.

5 Head Responses Subjected to Acceleration Loads

Publication Information

Title   Head responses subjected to frontal translational acceleration loads

Author   Shunfeng Li, Q.M. Li[*]

Journal   International Journal of Mechanical Sciences

Status   Published (DOI: 10.1016/j.ijmecsci.2022.107598)

Year   2022

---

[*]Corresponding author.

5.1 Introduction

The previous two chapters provide two different methodologies to improve the reliable and efficient design of helmet protection. However, in accidents, the helmeted head cannot be protected perfectly, and head injury can still happen during the excessive impact load/acceleration transmitted to the head [12]. As mentioned in Section 2.2.3, the helmeted head accelerations can be inputted to the high biofidelity head models to study the helmet design against head tissue-level responses. A deeper understanding of head injury mechanisms can support the further effective evolution of helmet design [13]. Thus, as mentioned in Section 2.2.2, numerical studies [95, 144-146, 148] have applied the impact accelerations to the high biofidelity head models to investigate the effects of acceleration loading configurations (e.g. loading curve shapes, peak magnitude and impact duration) on head impact responses and its injury mechanisms, in order to further support head injury prevention and helmet design development. However, the interactive influences of acceleration loading configurations on the head responses still have not been fully revealed, which can partially limit the development of helmet design.

This chapter is aimed to provide a quantitative numerical method to investigate the interactive effects of the peak magnitude and impact duration of frontal translational accelerations with different loading curve shapes on head responses in terms of the tissue-level injury predictors, such as intracranial pressure (ICP), von Mises stress (σ_v) and maximum principal strain (ε_p). Furthermore, the correlations between the HIC and tissue-level predictors are studied. After the introductory section, Section 5.2 designs a series of translational accelerations for modelling different head frontal impact scenarios using the THUMS head model. Section 5.3 conducts the numerical simulations to quantify the effects of different acceleration loading configurations on head responses, and compares the correlations between the HIC and tissue-level predictors. Section 5.4

provides a comprehensive discussion of the results and limitations of this chapter. Finally, Section 5.5 summarizes the main findings of this study and draws conclusions.

5.2 Methods

In this section, the THUMS 50th percentile male head model (Version 4) was introduced to investigate head responses under different frontal translational acceleration loads, which were defined using loading curve shape, impact duration and peak magnitude. The acceleration loading configurations for analysing the correlation between the *HIC* and tissue-level injury predictors were designed.

5.2.1 Finite element head model

As shown in Figure 5.1, the THUMS head model includes the detailed anatomical features of the head, such as scalp, skull, cerebrospinal fluid, cerebrum, cerebellum, falx, etc. The head bony parts, such as the skull, facial bone, and mandible, were modelled using the elasto-visco-plastic material model *MAT_81: PLASTICITY_WITH_DAMAGE available in commercial FE code LS-DYNA 971. The viscoelastic material model *MAT_6: VISCOELASTIC was used to simulate the cerebrospinal fluid, while another viscoelastic material model *MAT_61: KELVIN-MAXWELL_VISCOELASTIC was applied to simulate the brain tissues. Both shell and solid elements were adopted to develop this head model, which consists of 256,948 elements with mesh sizes ranging from 1.2 mm to 5 mm [125]. The validation of this model was accomplished by replicating different head cadaver impact experiments reported in [255], which demonstrates that the THUMS head model is capable to predict head impact responses, and therefore, it is used in this study.
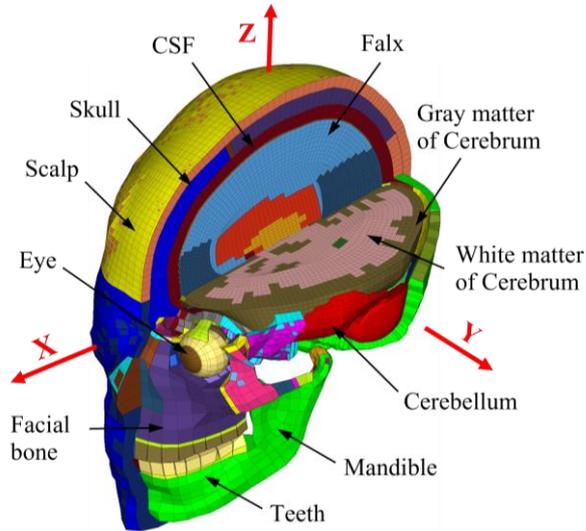
Figure 5.1. The high biofidelity THUMS head model

5.2.2 Simulation matrix for loading configurations

As shown in Figure 5.2, peak acceleration data and their corresponding impact duration for the head impact accidents were obtained from open literature [29, 96, 97, 117, 143, 231, 256-258]. Based on these published data, six peak magnitudes (100, 150, 200, 250, 300 and 350 g) and six impact durations (6, 8, 10, 12, 14 and 16 ms) were determined for the acceleration loads to cover the most likely range of head impact accidents.
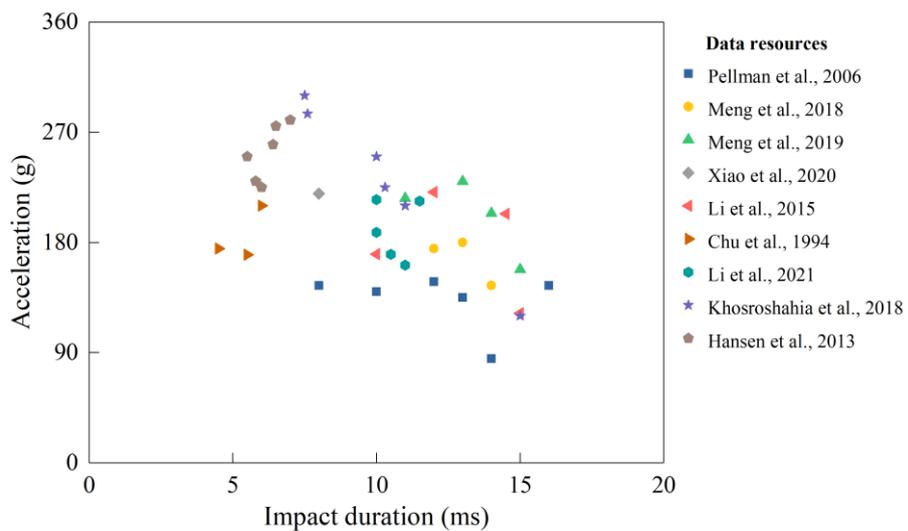
Figure 5.2. Acceleration transmitted to the head during impacts [29, 96, 97, 117, 143, 231, 256-258]

To focus more on the loading curve shape and minimize the influences from the other factors of acceleration loads, the accelerations from real-world head impact accidents are usually idealised as some typical equivalent loading curve shapes [85, 90], such as two examples shown in Figure 5.3. As presented in Figure 5.4, six typical equivalent shapes for acceleration loads, such as equivalent square shape (ESS), equivalent positive triangular shape (EPTS), equivalent negative triangular shape (ENTS), equivalent isosceles triangular shape (EITS), equivalent half-sine shape (EHSS) and equivalent haversine shape (EHVS), were considered here to investigate the effects of loading curve shape on head impact responses. These equivalent shapes can be formulated as follows,

for ESS load,

$$A(t) = A_{max}, (0 \leq t \leq T_d), \tag{5.1}$$

for EPTS load,

$$A(t) = \frac{A_{max}}{T_d} t, (0 \leq t \leq T_d), \tag{5.2}$$

for ENTS load,

$$A(t) = A_{max} - \frac{A_{max}}{T_d} t, (0 \leq t \leq T_d), \tag{5.3}$$

for EITS load,

$$A(t) = \begin{cases} \frac{2A_{max}}{T_d} t, & \left(0 \leq t \leq \frac{T_d}{2}\right) \\ 2A_{max} - \frac{2A_{max}}{T_d} t, & \left(\frac{T_d}{2} < t \leq T_d\right) \end{cases}, \tag{5.4}$$

for EHSS load,

$$A(t) = A_{max} \sin(\frac{\pi}{T_d} t), (0 \leq t \leq T_d), \tag{5.5}$$

for EHVS load,

$$A(t) = \frac{A_{max}}{2} \left(1 - \cos\frac{2\pi}{T_d} t \right), (0 \leq t \leq T_d), \tag{5.6}$$

where the acceleration-time history $A(t)$ can be determined by the parameters of peak magnitude A_{max} and impact duration T_d. $A(t) = 0$ when t is outside the specified time duration.
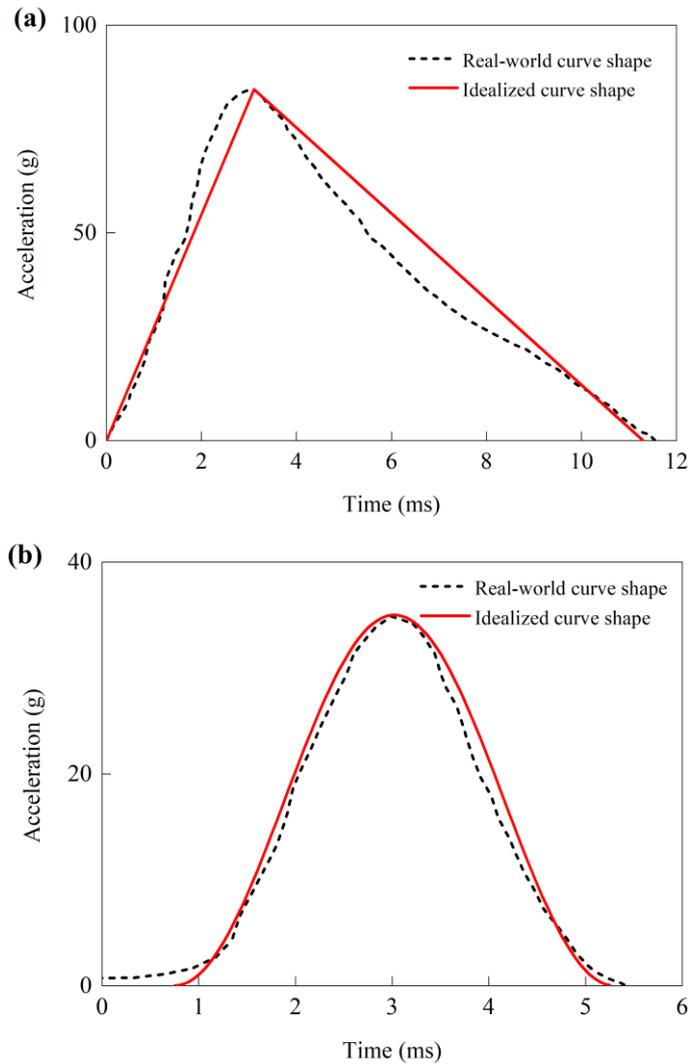
Figure 5.3. Two loading curve shapes idealised from acceleration-time histories in real-world head impact scenarios, (a) head responses from the test C288-T1 in Hardy's study [85], (b) head responses from the test C380-T2 in Hardy's study [85]
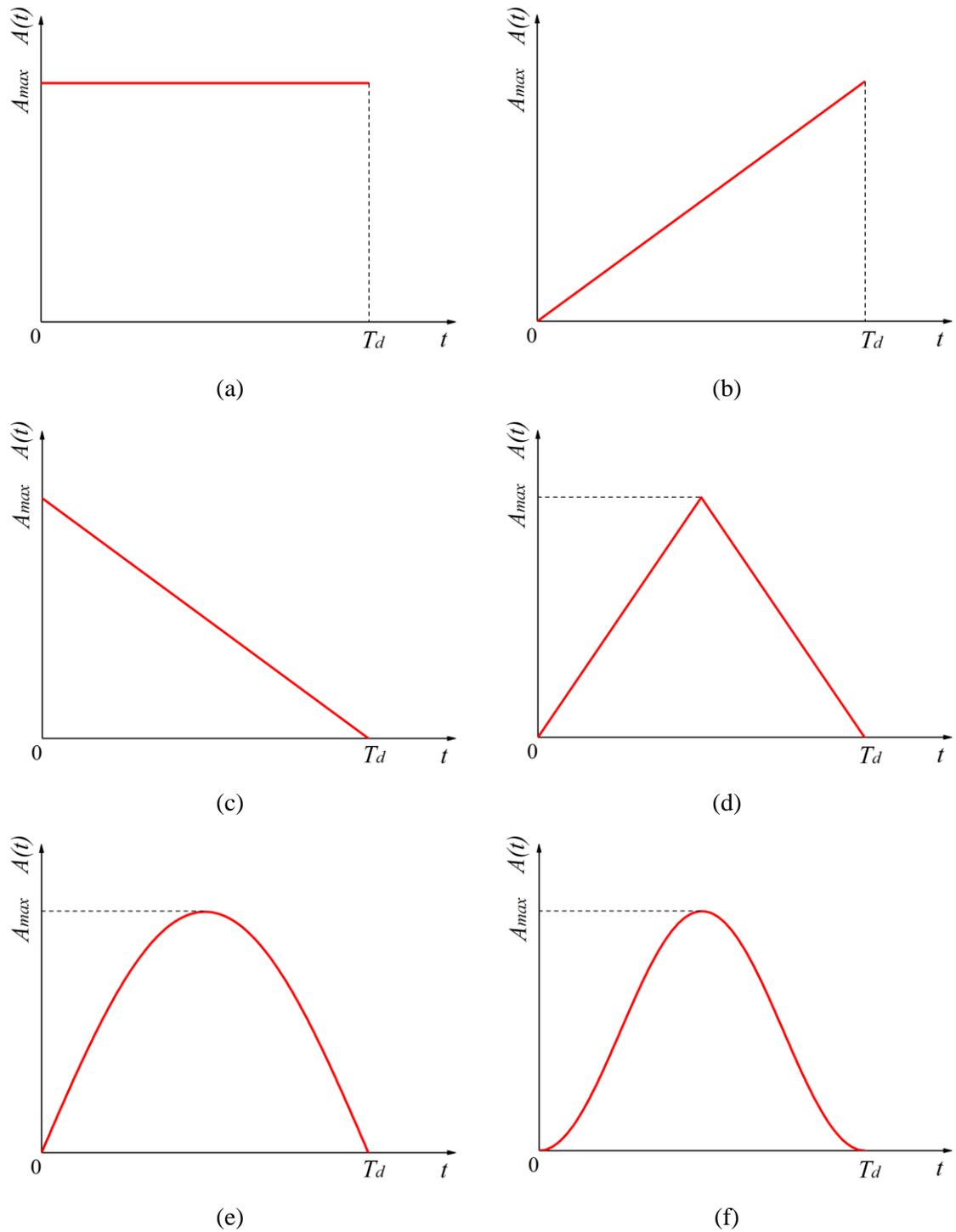
Figure 5.4. Six typical equivalent shapes for the translational acceleration loads applied to head model simulations, (a) ESS, (b) EPTS, (c) ENTS, (d) EITS, (e) EHSS, (f) EHVS

A simulation matrix was designed to combine all the above variables for modelling the head impact responses under extensive different translational acceleration loads, as shown in Figure 5.5. It can be seen from the figure that six loading curve shapes (ESS,

EPTS, ENTS, EITS, EHSS and EHVS) were adopted here and each acceleration loading curve shape can be assigned to six peak magnitudes (100, 150, 200, 250, 300 and 350 g) and six impact durations (6, 8, 10, 12, 14 and 16 ms). As such, 36 cases were applied to each of the six acceleration loading curve shapes, and a total of 216 loading conditions were arranged in this simulation matrix. A label method is used to facilitate the analysis, e.g. 'ESS-6-100' represents the equivalent square shape acceleration load applied to the head model with 6 ms impact duration and 100 g peak magnitude.
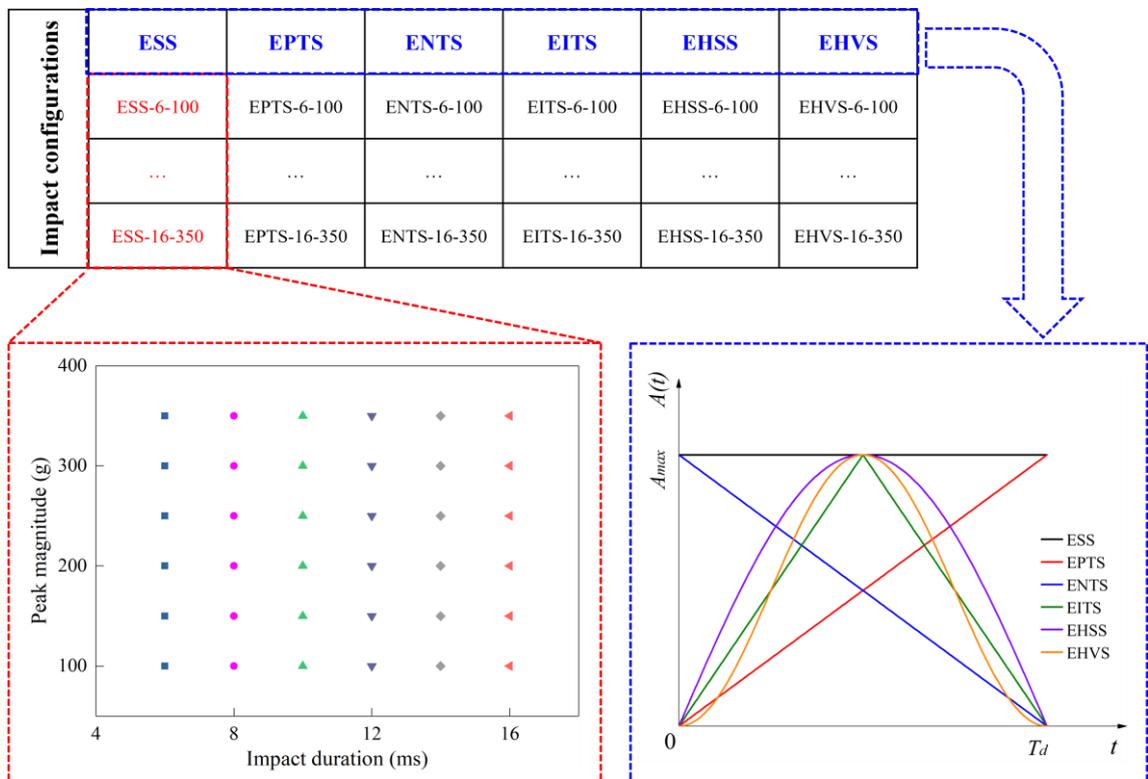
Figure 5.5. The simulation matrix of different acceleration loading configurations, including loading curve shape, impact duration and peak magnitude, applied to the head model

These translational acceleration loads (Figure 5.5) were imposed on the centre of gravity of the head model in the frontal direction to parametrically study the head responses under frontal impacts. Because the overall aim of this research is 'to provide the methodologies to support the reliable and efficient design of helmet' (Section 1.3), the simplest and mostly-studied loading condition, i.e. the translation acceleration loading,

is considered in this chapter. For the translational acceleration, only the most used kinematics-based injury predictor, HIC, needs to be employed in the following section to correlate the tissue-level injury predictors. However, if the more complex rotation acceleration is selected in this study, many other kinematics-based injury predictors, e.g. $GAMBIT$, HIP and $BrIC$, need to be considered for reasonable correlation analysis with the tissue-level injury predictors. It implies that the present quantitative study for rotational acceleration would demand far too many computational resources. Meanwhile, the research on the head response and injury due to translational acceleration is more mature than that due to rotational acceleration. This study intents to select a simple but typical translational acceleration to efficiently exemplify the application of this quantitative numerical method to explore the head impact responses. Then, this quantitative numerical method can also apply to rotational accelerations. Thus, only the frontal direction translational acceleration was considered in this study.

5.2.3   Simulations for the correlation analysis

Based upon the findings presented in the following Section 5.3.1, three typical loading curve shapes, including ESS, ENTS and EHSS, were adopted for the acceleration loads to further explore the correlation between the HIC and tissue-level predictors. The HIC function is given in Eq. (2.3). According to Standard FMVSS 208 [71], the calculated HIC shall not exceed 1000 for the time interval no more than 36 ms to prevent severe head injury occurrence. In addition, the HIC should be lower than 2400 to meet the helmeted head protection requirement prescribed in Standard ECE 22.05 [19]. As presented in Figure 5.6, the acceleration loads with two HIC thresholds (1000 and 2400) and six impact durations (6, 8, 10, 12, 14 and 16 ms) for three loading curve shapes (ESS, ENTS and EHSS) were applied to head model simulations. Each HIC value was calculated by six impact durations and their corresponding peak magnitudes. Interestingly, peak magnitudes for the loading curse shape of ESS with a HIC

threshold of 2400 are very close to the values for the EHSS cases with a *HIC* threshold of 1000, as displayed in Figure 5.6(a). In addition, the EHSS cases for the seven typical simulation points in Figure 5.6(a) were illustrated in Figure 5.6(b) for an easier understanding of the acceleration loading configurations. A total of 36 translational acceleration loading cases were designed for this correlation analysis.
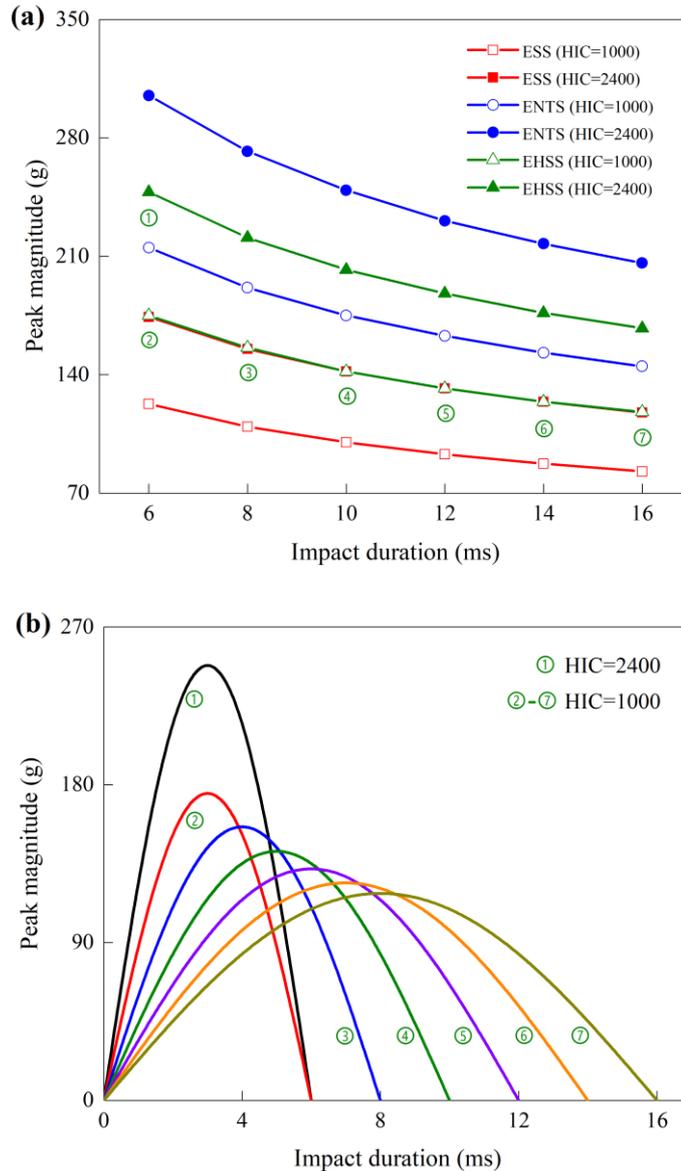
Figure 5.6. Translational acceleration loading configurations, (a) acceleration loads with two different *HIC* thresholds and six different impact durations for three loading curve shapes, (b) illustration of the EHSS cases for seven typical acceleration loading configurations in (a)

5.3   Numerical results

In Section 5.3.1, the tissue-level injury predictors, i.e. ICP, σ_v and ε_p, were obtained from the head models to investigate the interactive effects of different acceleration loading configurations on head responses. In addition, the correlation analysis between HIC and tissue-level injury predictors was further presented in Section 5.3.2.

5.3.1   Effects of different acceleration configurations

5.3.1.1   Effects of loading curve shape

The effects of loading curve shape on head responses were analysed in this section. In this regard, the numerical results of head responses for six loading curve shapes are compared in Figure 5.7. The typical contour plots of ICP histories for six head model simulations, such as ESS-6-100, EPTS-6-100, ENTS-6-100, EITS-6-100, EHSS-6-100 and EHVS-6-10, are shown in Figure 5.8. These ICP results showed the apparent gradient characteristics and agreed well with other reported experiments [81] and simulations [104], which further demonstrated the accuracy and effectiveness of the THUMS head model subjected to translational acceleration loads. Moreover, typical σ_v and ε_p time histories for the head model simulations with six loading curve shapes were presented in Figure 5.9. The peak values of tissue-level responses for these six head model simulations are summarized in Table 5.1. More detailed numerical results for the head responses are displayed in **Appendix A**.
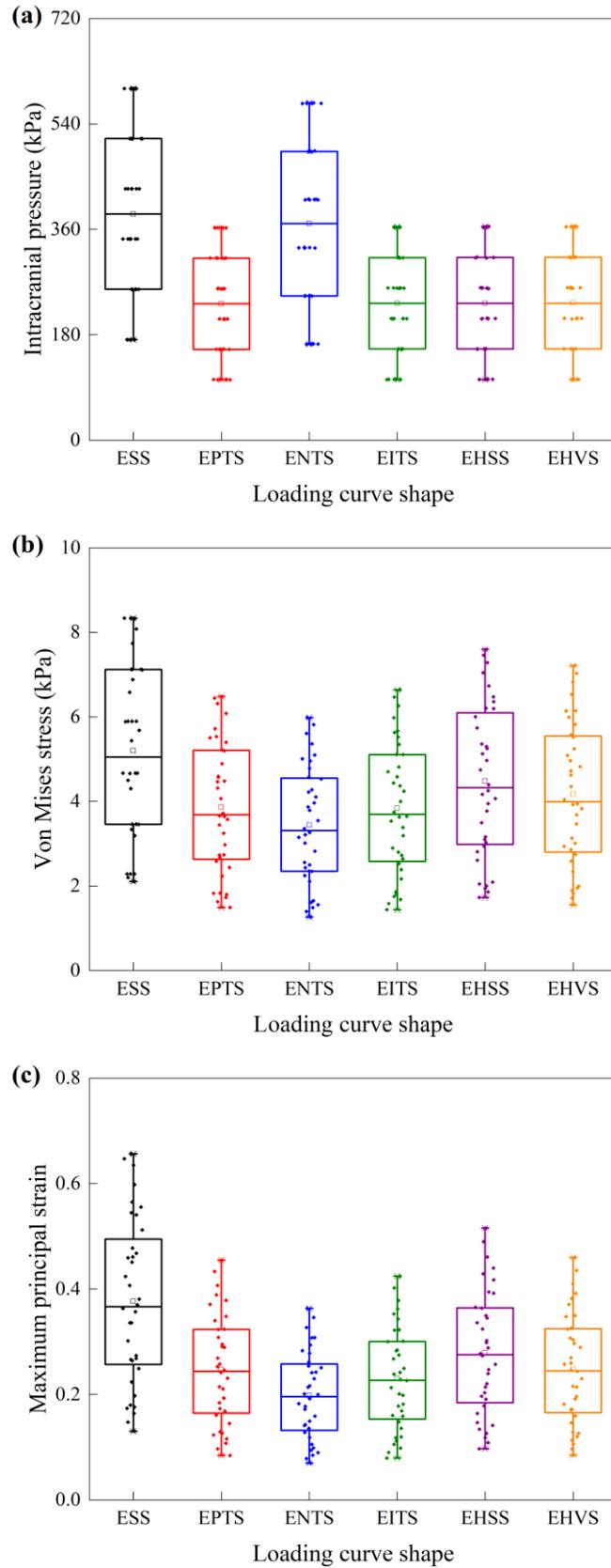
Figure 5.7. The effects of loading curve shape on head responses, (a) intracranial pressure, (b) von Mises stress, (c) maximum principal strain

| | t = 1 ms | t = 2 ms | t = 3 ms | t = 4 ms | t = 5 ms | t = 6 ms |

(a)

(b)

(c)

(d)

(e)

(f)

-120 -88 -55 -22 11 44 77 109 142 175 (kPa)
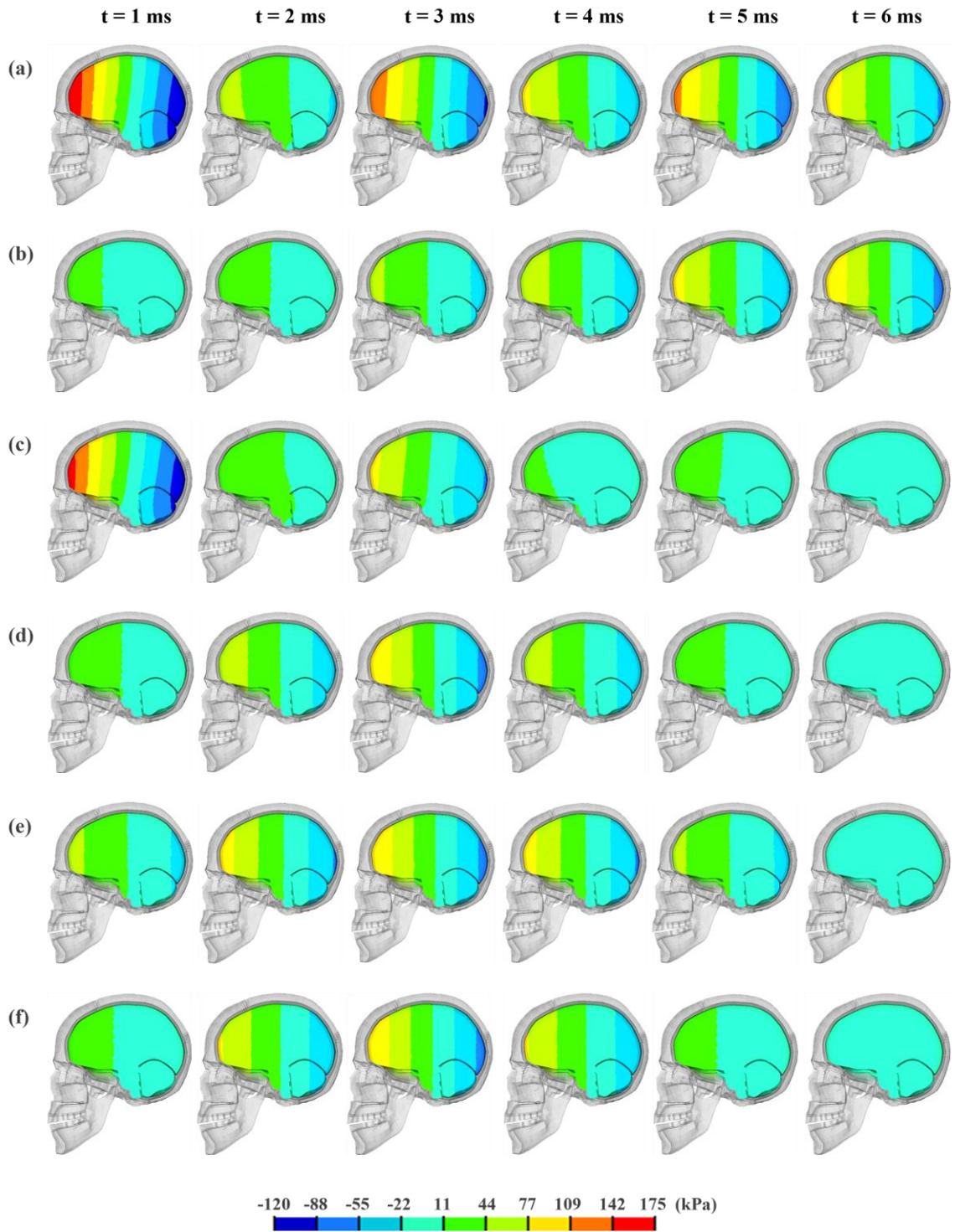
Figure 5.8. Typical *ICP* histories for the head model simulations with six different loading curve shapes, (a) ESS-6-100, (b) EPTS-6-100, (c) ENTS-6-100, (d) EITS-6-100, (e) EHSS-6-100, (f) EHVS-6-100
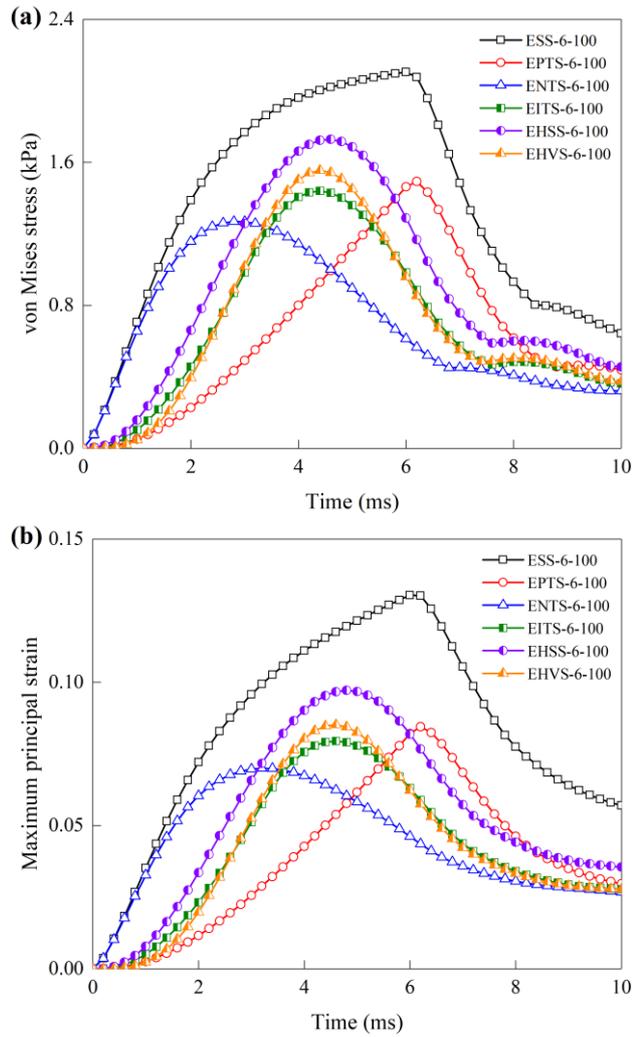
Figure 5.9. Typical σ_v and ε_p histories for the head model simulations with six loading curve shapes, (a) von Mises stress, (b) maximum principal strain

Table 5.1. Head responses when subjected to different acceleration loads

Acceleration loads	ICP (kPa)	σ_v (kPa)	ε_p
ESS-6-100	172	2.11	0.130
EPTS-6-100	104	1.49	0.084
ENTS-6-100	164	1.27	0.070
EITS-6-100	104	1.44	0.079
EHSS-6-100	104	1.73	0.097
EHVS-6-100	104	1.55	0.085

For the ICP responses in the cases of the same peak magnitude and impact duration loading conditions, as shown in Figure 5.7(a), the greatest ICP values can be easily identified in the head model simulation with the loading curve shape of ESS. The ICP values for the loading curve shape of ENTS are slightly lower than that of ESS cases, e.g. max ICP = 164 kPa for the ENTS-6-100 and max ICP = 172 kPa for the ESS-6-100 presented in Table 5.1. Almost the same ICP values were observed for the other four loading curve shapes of EPTS, EITS, EHSS and EHVS, e.g. max ICP = 104 kPa, which are much lower than the ICP values from corresponding ESS and ENTS cases. Furthermore, as presented in Figure 5.8, the maximum ICP values throughout the loading histories for both ESS and ENTS cases were identified at the initial loading stage, and the maximum ICP values were obtained at the impact time of 1 ms; while the maximum ICP values for the other four loading curve shapes were found at the impact time of 3 ms, which is the middle stage of loading histories.

As for the influences of loading curve shape on the σ_v and ε_p responses, common change trends can be found in these two types of tissue-level predictors, as presented in Figure 5.7 and Figure 5.9. As the head model was subjected to identical peak magnitude and impact duration loading conditions, the largest values for σ_v and ε_p can be found in head model simulations with the loading curve shape of ESS, while those lowest values were observed in ENTS counterparts, e.g. max σ_v = 2.11 kPa and max ε_p = 0.13 for ESS-6-100; max σ_v = 1.27 kPa and max ε_p = 0.07 for ENTS-6-100 presented in Table 5.1. Meanwhile, the σ_v and ε_p for EHSS cases were much higher than those values from the other three loading curve shapes of EPTS, EITS and EHVS, e.g. max σ_v = 1.73 kPa and max ε_p = 0.097 for EHSS-6-100; max σ_v = 1.49 kPa and max ε_p = 0.084 for EPTS-6-100 presented in Table 5.1.

5.3.1.2   *Effects of peak magnitude and impact duration*

The effects of peak magnitudes and impact duration on head responses were studied in this section. The numerical data for the peak values of ICP, σ_v and ε_p under loading conditions with different peak magnitudes and impact durations are quantitatively presented in Figure 5.10, Figure 5.11 and Figure 5.12, respectively.

As shown in Figure 5.10, the ICP responses increased with the increment of peak magnitude, whereas the impact duration does not influence the ICP responses, and almost the same ICP values can be found from the head model simulations with the same peak magnitude and loading curve shape. In addition, the head model simulations with the loading curve shapes of ESS and ENTS showed significantly larger ICP ranges than those for the loading curve shapes of EPTS, EITS, EHSS and EHVS. For instance, the ranges of ICP for the ESS and ENTS cases were 172 kPa ~ 600 kPa and 164 kPa ~ 576 kPa, respectively, and very similar ICP results ranged from 104 kPa to 365 kPa can be found for the other four loading curve shapes, see Figure 5.7(a). In general, both the peak magnitude and loading curve shape of the accelerations can influence the ICP responses, which was further investigated by correlation analysis in Section 5.3.1.3.

Regarding the σ_v and ε_p results presented in Figure 5.11 and Figure 5.12, both σ_v and ε_p responses increased with the increment of peak magnitude and impact duration. In comparison with impact duration, peak magnitude can lead to a more significant change of σ_v responses, especially for the ESS cases. It is observed from Figure 5.11(a) that the impact durations larger than 10 ms in the ESS cases almost do not influence σ_v responses, which increase with the increase of peak magnitude. Comparing with the σ_v and ε_p responses in the six loading curve shapes, it was found that the ESS cases can lead to significantly higher σ_v and ε_p, while the lowest σ_v and ε_p responses were identified

for the ENTS cases. For the same peak magnitude and impact duration of translational acceleration loads applied to the head model simulations, both σ_v and ε_p responses are following an order of ESS>EHSS>EHVS>EPTS>EITS>ENTS.

To evaluate head injury under impacts, tissue-level predictors obtained from head models are usually used to compare to their corresponding injury thresholds. For example, the ICP threshold values of 173 kPa and 235 kPa were employed to predict the occurrence of moderate and serious head injuries, respectively [219]. For the σ_v thresholds, the value of 18 kPa and 38 kPa were used for 50% risk of mild and severe head injury, respectively [220]; while the ε_p threshold values of 0.18 and 0.28 were often selected respectively for 50% and 80% probability of mild brain injury [259]. As presented in Figure 5.7, the ICP results range from 104 kPa to 600 kPa, and the ε_p results range from 0.07 to 0.65, and the σ_v results range from 1.27 kPa to 8.33 kPa. It was found that both ICP and ε_p responses can be higher than their corresponding injury thresholds, and thus the ICP-induced and ε_p-induced head injuries can be predicted for the head model subjected to the frontal translational acceleration loads; whereas all σ_v responses were much lower than their thresholds, indicating that the σ_v-induced head injury would not be likely to occur under the frontal translational acceleration loads. As the tissue-level predictors can be associated with head injury mechanisms. In this regard, the ICP is usually linked to brain contusion [55, 219], while both the σ_v and ε_p responses usually have been suggested as the mechanisms of concussion and diffuse axonal injury (DAI) [32, 55, 220, 259, 260]. Therefore, the above findings suggested that the frontal translational acceleration loads transmitted to the head are more likely to lead to ICP-induced brain contusion. Concussion and DAI can also be predicted by the ε_p responses but not predicted by σ_v injury thresholds.
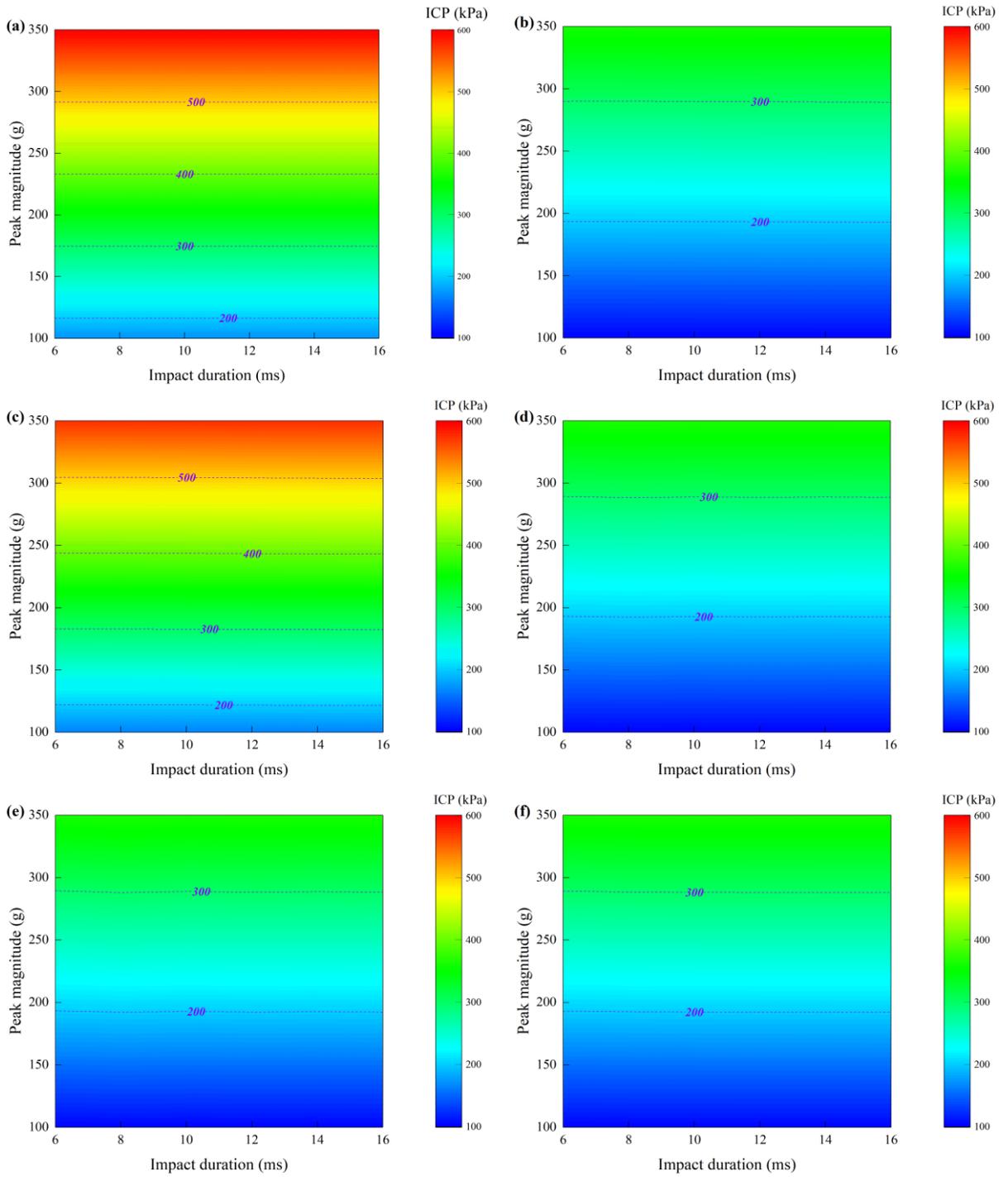
Figure 5.10. The effects of peak magnitude and impact duration on the peak *ICP* with six different loading curve shapes, (a) ESS, (b) EPTS, (c) ENTS, (d) EITS, (e) EHSS, (f) EHVS
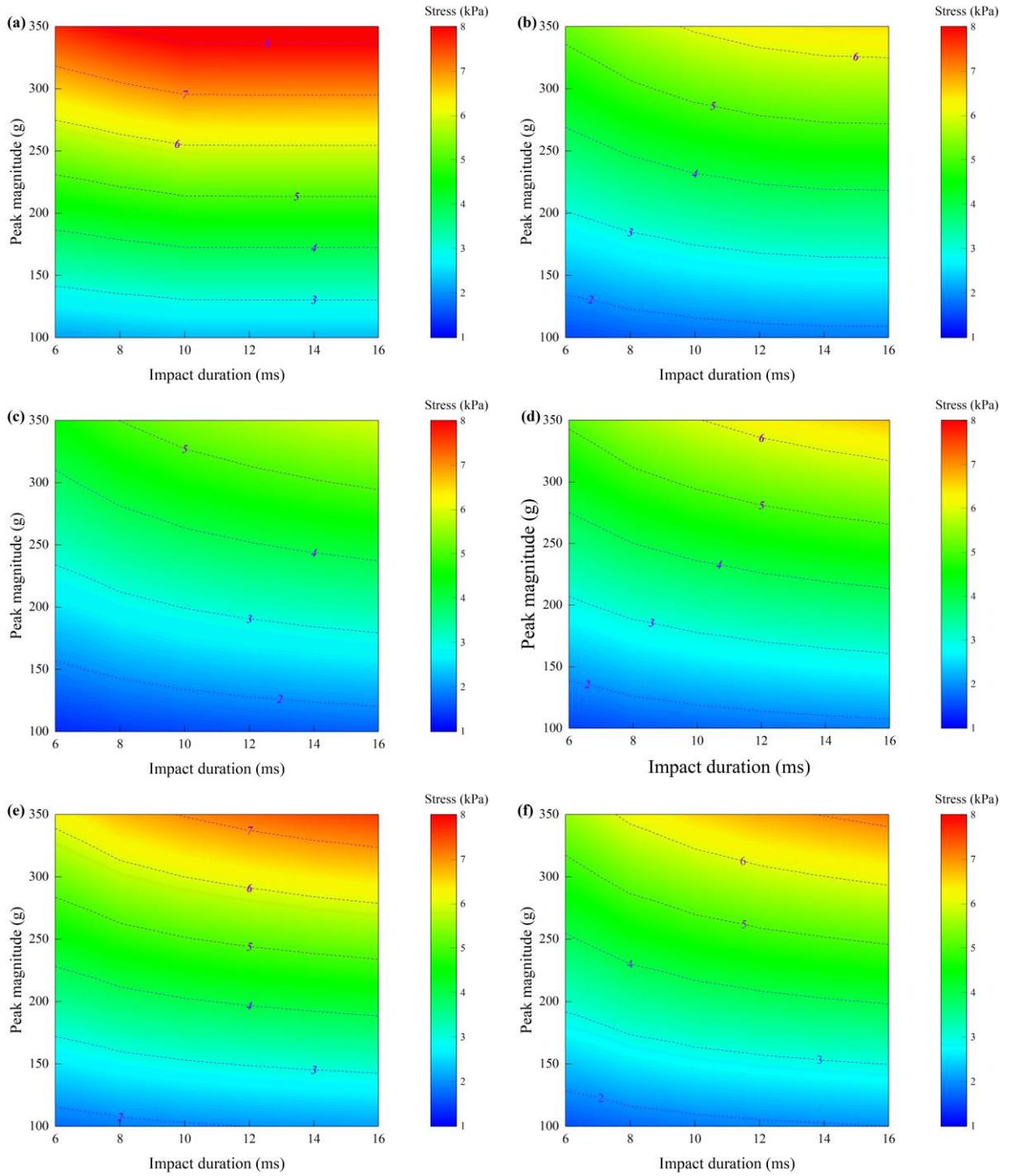
Figure 5.11. The effects of peak magnitude and impact duration on the peak σ_v with six different loading curve shapes, (a) ESS, (b) EPTS, (c) ENTS, (d) EITS, (e) EHSS, (f) EHVS
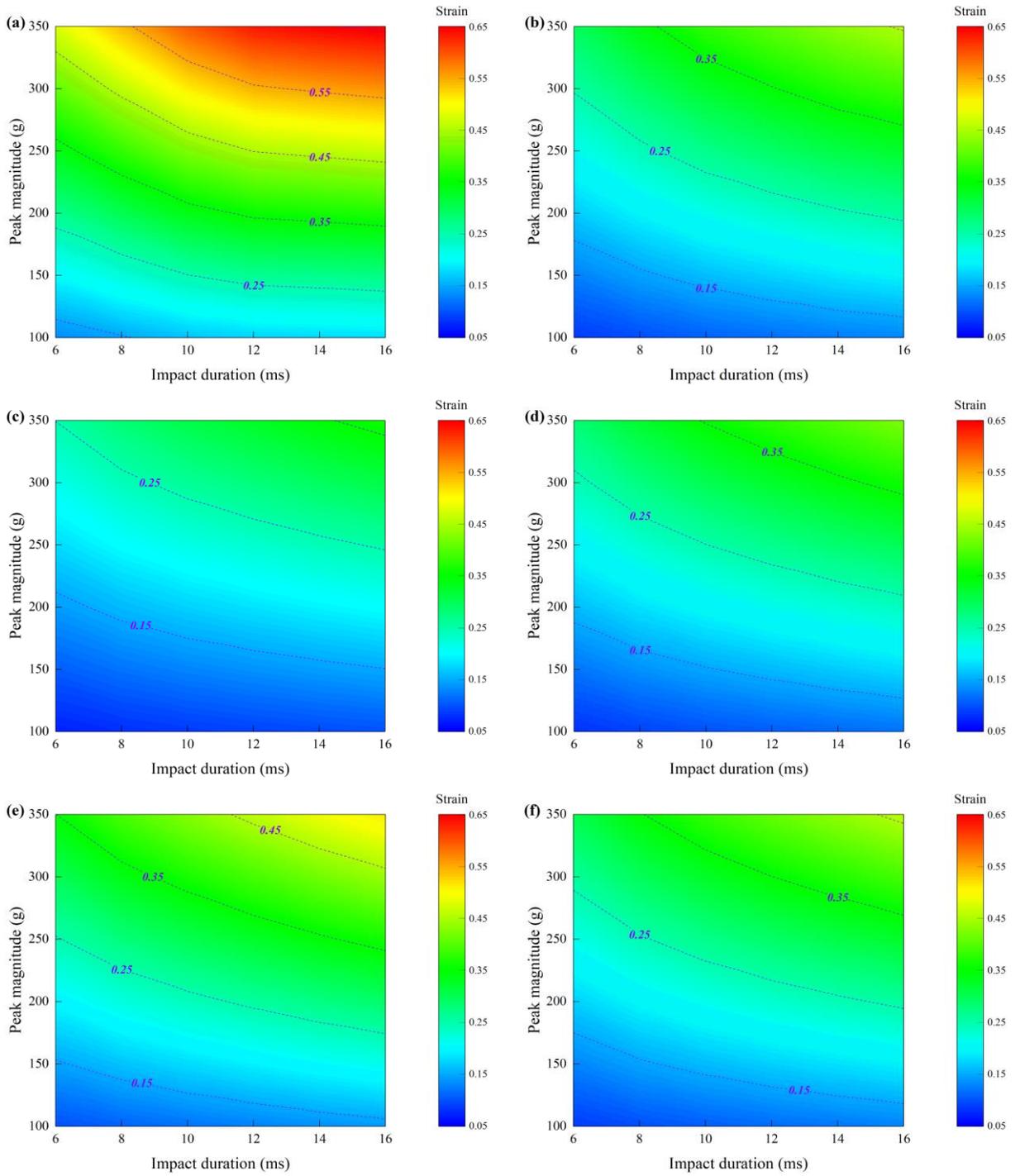
Figure 5.12. The effects of peak magnitude and impact duration on the peak ε_p with six different loading curve shapes, (a) ESS, (b) EPTS, (c) ENTS, (d) EITS, (e) EHSS, (f) EHVS

5.3.1.3   *Correlation analysis of ICP responses*

As shown in Figure 5.10, the peak ICP responses were influenced by peak magnitude and loading curve shape, the correlation analysis was thus carried out to study the relationship between the ICP responses and peak magnitude with six different loading curve shapes. As presented in Figure 5.13, strong linear relations could be found between the ICP responses and peak magnitude (A_{max}). It could be found that with the same peak magnitudes, the highest ICP values can be found in the ESS cases while the second highest ICP values were seen in the ENTS cases, almost the same ICP values can be observed for the other four different loading curve shapes. Meanwhile, the maximum slope of these ICP linear relationships can be found in the ESS cases while the second largest slope can be found in ENTS cases, which indicates that the ICP responses are more sensitive to the ESS and ENTS cases. The relations for six loading curve shapes are displayed as follows,

for ESS load,

$$ICP = 1.714A_{max} + 0.620, (R^2 = 0.99), \qquad (5.7a)$$

for EPTS load,

$$ICP = 1.037A_{max} - 0.178, (R^2 = 0.99), \qquad (5.7b)$$

for ENTS load,

$$ICP = 1.645A_{max} - 0.282, (R^2 = 0.99), \qquad (5.7c)$$

for EITS load,

$$ICP = 1.040A_{max} - 0.315, (R^2 = 0.99), \qquad (5.7d)$$

for EHSS load,

$$ICP = 1.041A_{max} - 0.242, (R^2 = 0.99), \qquad (5.7e)$$

for EHVS load,

$$ICP = 1.042A_{max} - 0.336, (R^2 = 0.99). \qquad (5.7f)$$

These linear relationships of the *ICP* responses to peak magnitude can be demonstrated by the experimental data of head cadaver impacts reported by Nahum [81] and Hardy [85], and the experimental linear *ICP* results to peak magnitude are also provided in Figure 5.13. Finally, based on these relations, the *ICP* responses aroused from the frontal translational acceleration loads to the head can be well predicted using the peak magnitudes.
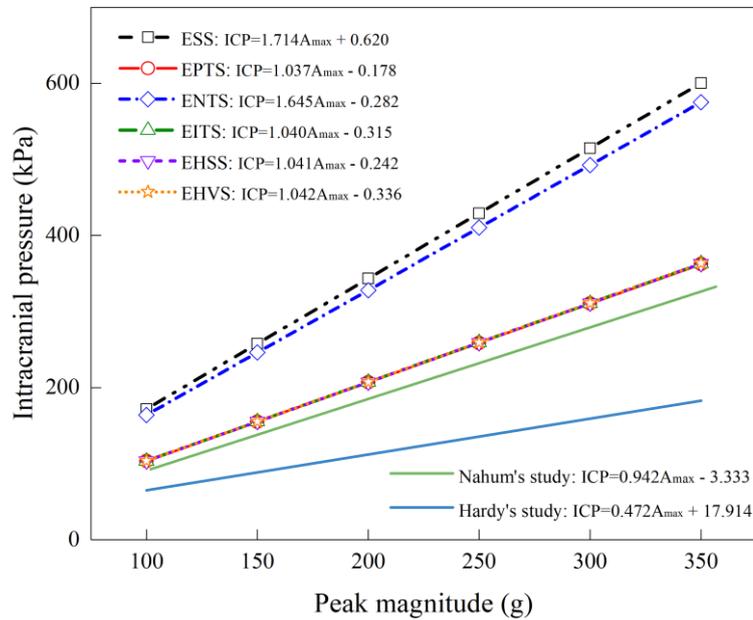
Figure 5.13. Correlation analysis between *ICP* responses and peak magnitudes (Nahum's experimental results obtained from [81] and Hardy's experimental results obtained from references [85])

5.3.2 Correlation between *HIC* and tissue-level injury predictors

The head models subjected to the frontal translational acceleration loads with two *HIC* thresholds (1000 and 2400) and six impact durations (6, 8, 10, 12, 14 and 16 ms) for three representative loading curve shapes (ESS, ENTS and EHSS) were carried out to study the correlation between the *HIC* and tissue-level predictors. The peak responses of *ICP*, σ_v and ε_p for the head model simulations are presented in Figure 5.14.

As compared in Figure 5.14(a), the loading curve shape of ENTS can result in significantly higher *ICP* responses than those produced by the other two counterparts of ESS and EHSS. As such, the highest *ICP* responses in a range of 340 kPa ~ 500 kPa can be found in the ENTS cases with a *HIC* threshold of 2400 for six different impact durations. Even the *ICP* responses ranged from 240 kPa ~ 353 kPa in the ENTS cases with the *HIC* threshold of 1000 are much higher than those for the corresponding ESS and EHSS cases with the *HIC* threshold of 2400. It was also found that the lowest *ICP* responses in a range of 121 kPa ~ 180 kPa (or 172 kPa ~ 256 kPa) can be found in the EHSS cases with a *HIC* threshold of 1000 (or 2400) for six different impact durations, indicating that the *ICP* responses in the ENTS cases were almost twice as much as the *ICP* values in corresponding EHSS cases.

Regarding the σ_v results shown in Figure 5.14(b), the loading curve shape of EHSS can lead to the largest σ_v responses (3.54 kPa ~ 4.36 kPa) among three loading shapes with a *HIC* threshold of 2400 at six different impact durations, while the corresponding values 3.46 kPa ~ 3.94 kPa and 2.69 kPa ~ 3.72 kPa are for the ENTS and ESS cases, respectively. In addition, different decreasing rates with loading duration can be found for different loading curve shapes. The ESS cases have the largest decreasing rate, and the EHSS cases show a slightly smaller decreasing rate than the ESS cases, whereas the ENTS cases experience a much flatter reduction than the ESS and EHSS cases. Therefore,

the σ_v differences between the EHSS and ENTS cases become smaller with the increment of impact duration (e.g. σ_v = 3.54 kPa and 3.46 kPa for the EHSS and ENTS cases, respectively, at an impact duration of 16 ms), which indicates that the ENTS cases may cause the higher σ_v than the EHSS counterparts for the loading configurations with longer impact duration. The different decreasing rates for the ESS and EHSS cases also increase the gap between their von Mises stresses.

As for the ε_p results displayed in Figure 5.14 (c), the largest ε_p (0.168 ~ 0.172 and 0.240 ~ 0.245 for the HIC thresholds of 1000 and 2400, respectively) can be found in the EHSS cases, while the smallest values (0.144 ~ 0.152 and 0.207 ~ 0.218 for the HIC thresholds of 1000 and 2400, respectively) are presented in the ENTS cases. Only slight changes in ε_p can be observed for the EHSS and ENTS cases with the increase of impact duration for each HIC threshold; while the ε_p value in the ESS case undergoes a steady rise to its peak values (e.g. ε_p = 0.164 and 0.235 for the HIC threshold of 1000 and 2400, respectively) at impact duration of 10 ms and then continues to drop quickly to the minimum (e.g. ε_p = 0.148 and 0.213 for the HIC threshold of 1000 and 2400, respectively) at impact duration of 16 ms.
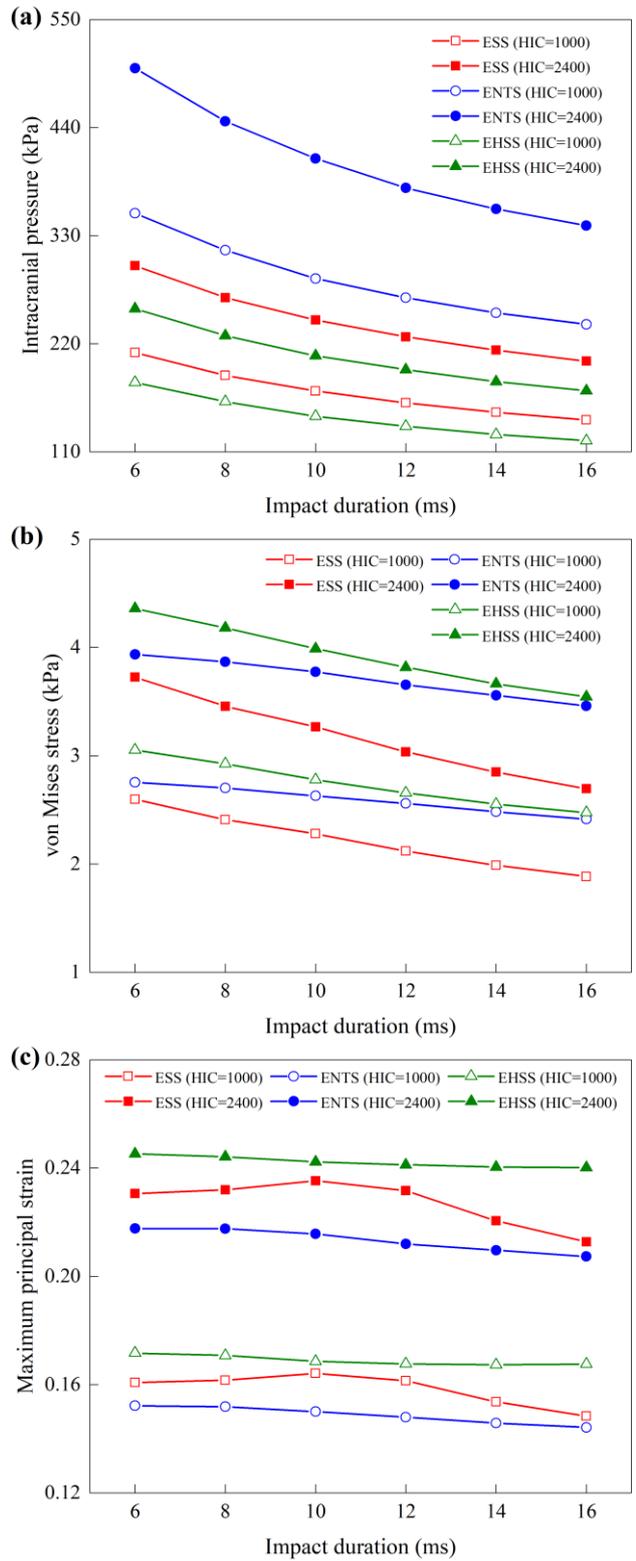
Figure 5.14. Peak responses for the head models subjected to the translational acceleration loads with two *HIC* thresholds for three representative loading curve shapes with six impact durations, (a) intracranial pressure, (b) von Mises stress, (c) maximum principal strain

The comparison between the HIC and tissue-level predictors' thresholds, i.e. HIC = 1000 and 2400, ICP = 173 kPa and 235 kPa, as well as ε_p = 0.18 and 0.28, for the head models subjected to the translational acceleration loads with three loading curve shapes are presented in Figure 5.15 and Figure 5.16. Noting that σ_v thresholds, i.e. σ_v = 18 kPa and 38 kPa, were not considered here because the σ_v values obtained from the head models are much lower than the thresholds, as shown in Figure 5.11.

The HIC and ICP thresholds for head injury prediction are compared in Figure 5.15. Three different loading curve shapes can lead to significantly different HIC and ICP injury boundaries. The HIC and ICP injury boundaries are not generally consistent, since the ICP responses are only influenced by peak magnitude regardless of impact duration, whereas both peak magnitude and impact duration can influence the HIC results. This implies that they may not be based on the same head injury mechanisms. If they represent different injury mechanisms, both the lower bound of the HIC and ICP injury thresholds should be considered to predict head injury.

As shown in Figure 5.16, all ε_p no-injury boundaries are higher than the corresponding HIC boundaries. However, it is found that the profiles of ε_p no-injury boundary are consistent with the HIC boundary for all three loading curve shapes, indicating they may represent similar injury mechanisms in a head frontal acceleration loading condition. As shown in Figure 5.12, both peak magnitude and impact duration influence the ε_p responses, while the HIC values are determined by the impact duration and acceleration-time history according to Eq. (2.3). These comparisons indicate that the HIC is correlated well to the ε_p for the head model subjected to the frontal translational acceleration loads.
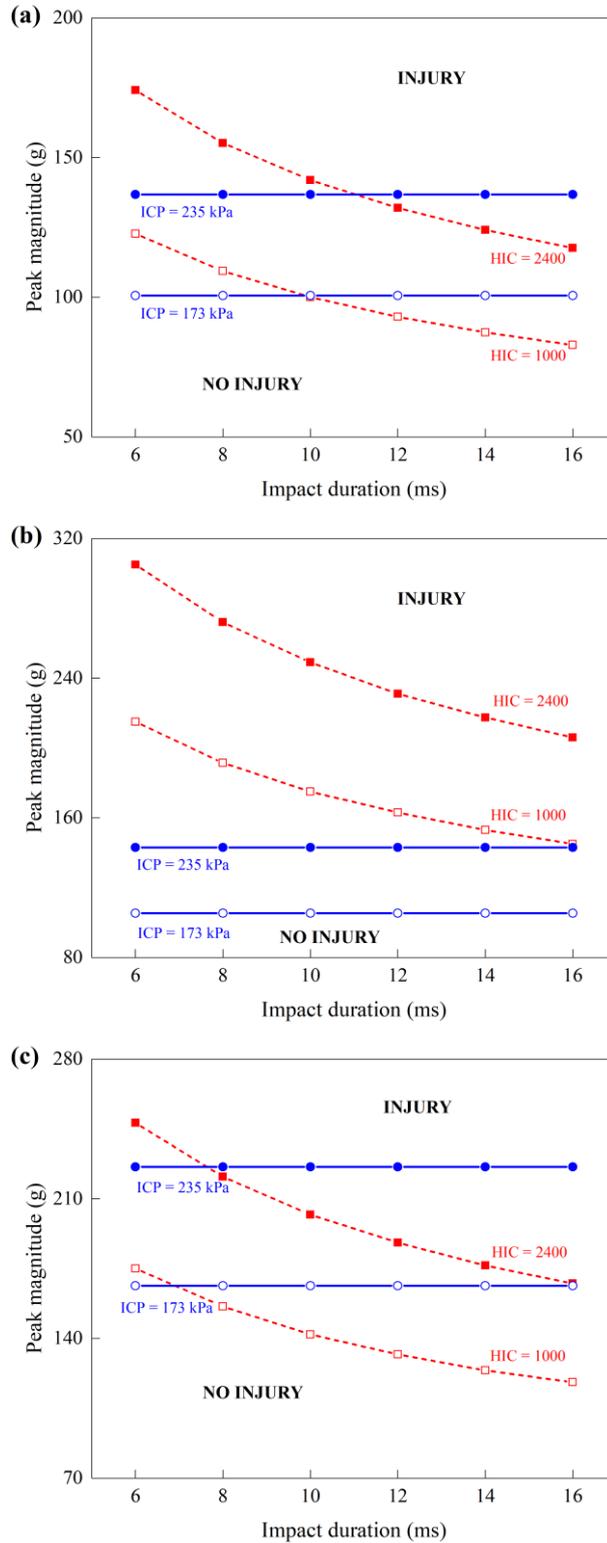
Figure 5.15. Comparison between the *HIC* and *ICP* thresholds for the head models under the frontal translational acceleration loads with three loading curve shapes, (a) ESS cases, (b) ENTS cases, (c) EHSS cases

(a)

(b)

(c)
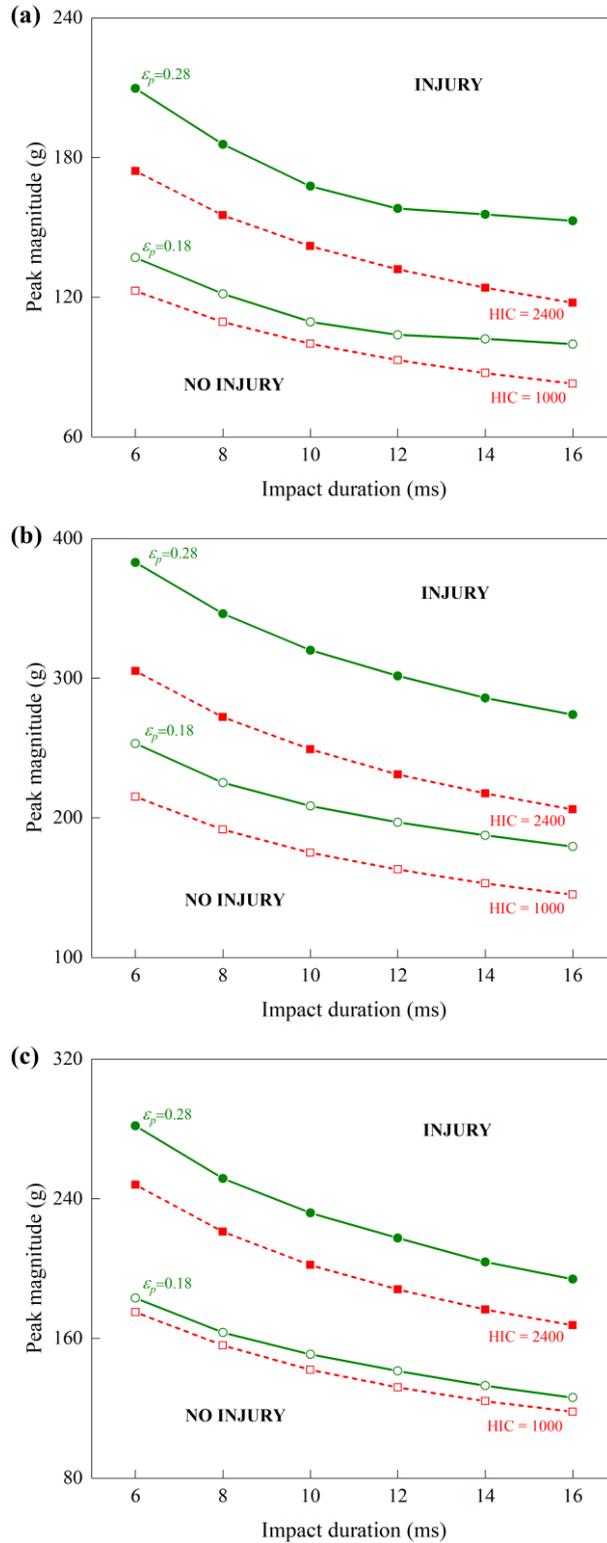
Figure 5.16. Comparison between the HIC and ε_p thresholds for the head models under the frontal translational acceleration loads with three loading curve shapes, (a) ESS cases, (b) ENTS cases, (c) EHSS cases

5.4 Discussion

In this chapter, the interactive influences of the peak magnitude and impact duration of frontal translational accelerations with different loading curve shapes on head responses were investigated quantitatively using the THUMS head model. Similar profiles can be found between σ_v and ε_p output curves (Figure 5.9) for each frontal translational acceleration load. The order of maximum σ_v and ε_p responses for six loading curve shapes is ESS>EHSS>EHVS>EPTS>EITS>ENTS when imposing a translational acceleration load with the same impact duration and peak magnitude. It indicates the significant influence of loading curve shapes on the σ_v and ε_p responses. These findings are consistent with Post et al.'s observation [144], which reported the similar profiles of σ_v and ε_p output curves to the linear acceleration loads. They compared two acceleration loading curves A and B with the same impact duration and peak magnitude, and found that the loading curve A with a longer rising time to peak magnitude leads to a higher maximum value of σ_v and ε_p responses. In comparison with the study presented in this chapter, loading curve A is similar to the EPTS while the loading curve B is similar to the ENTS; the maximum σ_v and ε_p responses obtained from EPTS case are higher than the ENTS counterpart, which is consistent with the results obtained in [144].

This study found that peak σ_v and ε_p responses can increase with the increase of both peak magnitude and impact duration (Figure 5.11 and Figure 5.12), indicating that longer duration and larger magnitude could cause a higher risk of head injury. This relationship is similar to the well-known Wayne State Tolerance Curve (Figure 2.8), which reported that both higher magnitude with shorter duration and lower magnitude with longer duration can cause head injury [67]. This finding can be also supported by many previous studies [85, 120, 145, 261, 262]. For example, Hardy et al. [85] conducted

human cadaver head impact tests and found that the maximum ε_p responses can increase with the increment of impact duration. In this study, the quantitative effects of peak magnitude and impact duration on maximum σ_v and ε_p responses were further determined, which can provide a rapid estimation of the tissue-level responses according to the given translational acceleration loading configurations.

When the frontal translational acceleration loads with the same impact duration and peak magnitude are applied, the order of maximum ICP responses for six loading curve shapes is ESS>ENTS>EPTS=EITS=EHSS=EHVS (Figure 5.7), which implies that the maximum ICP responses are not completely determined by the loading curve shapes. Further, according to the comparison between Figure 5.4 and Figure 5.8, the maximum ICP values for each loading curve shape can be found around the time of their peak magnitudes. This finding is in line with the works presented in **Chapter 3** (Figure 3.12 and Figure 3.15) as well as the study reported by Zheng et al. [38], who performed different helmeted head drop tests and found that the maximum ICP responses are always achieved around the time of peak magnitude of head acceleration. In addition, the maximum ICP response is influenced by the peak magnitude but not affected by the impact duration (Figure 5.10), which can be demonstrated by the experimental studies reported by Nahum et al. [81] and Hardy et al. [85]. The linear correlations between peak magnitudes and ICP responses have an average R^2 of 0.99 for six different loading curve shapes, and these relationships can be used to predict the maximum ICP response by peak magnitude of frontal translational acceleration.

Since pure translational acceleration loads were applied to the head model, the effects of rotational motions were excluded from this study. Thus, kinematic-based injury predictors, like brain injury criterion ($BrIC$) and peak rotational velocity (PRV), associated with the rotational motions of the head are beyond the scope of this study,

and therefore, are not considered in this thesis [75]. Only the most used kinematic-based predictor, HIC, which is based on the resultant translational acceleration, was employed for the correlation analysis with the tissue-level injury predictors. It was found that the HIC can be correlated well to the ε_p responses for the head model subjected to the frontal translational acceleration loads. The correlation between the HIC and ε_p was confirmed earlier by Kleiven [32, 95] who analysed the effect of acceleration durations on head responses using the KTHFEHM. This study further considers the interactive effects of both impact duration and peak magnitude of translational acceleration on head responses, which can provide more quantitative data as supplementary evidence for the correlation between the HIC and ε_p responses.

Several important limitations of this study need to be noted. Firstly, this study only focuses on frontal translational accelerations to give a quantitative understanding of how the frontal translational acceleration loading configurations contribute to head impact responses. Rotational acceleration is also commonly observed in head impact accidents and is the key cause of head injuries, such as concussion, DAI and SDH [95, 146, 263, 264]. However, the effects of rotation acceleration on head impact responses were not considered here. Further, the impact direction has significant influences on head responses [120], whereas only the frontal direction was explored in this chapter. Thus, it is suggested that the effects of the rotational acceleration configurations on head responses should be carried out in future studies, and the impact direction also needs to be further considered. Secondly, the thresholds used here are not developed using the THUMS head model. In this study, it was assumed that these thresholds can be applied to the THUMS numerical study, which needs to be further verified. In addition, the thresholds for the HIC and tissue-level predictors may not represent the same severity of head injury, leading to the uncertainty of quantitative correlation between the HIC and tissue-level predictors. Finally, higher frequency oscillation is neglected in the idealised

acceleration curves considered in this study. However, acceleration-time histories in a crushing event contain higher frequency components, which can influence structural damage [265]. Therefore, this study should be further extended to understand the influence of the higher frequency components on head injury.

5.5 Conclusions

In this chapter, a quantitative numerical analysis was conducted to provide further insight into the relationship between frontal translational acceleration loading configurations and head responses. The interactive effects of loading curve shape, impact duration and peak magnitude on the tissue-level responses were analysed, and the relationships between the HIC and tissue-level responses were further explored. The numerical results show that the head responses are significantly affected by translational acceleration loading configurations. Both the σ_v and ε_p responses increase with impact duration and peak magnitude, whereas the ICP responses increase with peak magnitude but are independent of impact duration. Linear relationships between the ICP responses and peak magnitudes are determined for six acceleration loading curves. Among the six representative acceleration loading curves, the ESS loading curve leads to the largest head responses. Based on the thresholds of head injury, the ICP-induced and ε_p-induced head injuries are observed from the head model simulations. However, the σ_v-induced head injury cannot be predicted due to the σ_v values measured from head models are much lower than their corresponding thresholds. Comparing the thresholds for the HIC and tissue-level injury predictors, it is found that the HIC has a good correlation with the ε_p responses, while significant differences in injury boundaries can be found between the HIC and ICP responses. Therefore, both the HIC and ε_p responses are recommended together with the ICP injury threshold to cover different injury mechanisms to improve the accuracy of head

injury prediction. This quantitative study on head responses under the frontal translational acceleration loads can provide a rapid estimation of the tissue-level responses with the given loading configurations. A better understanding of the relationship between translational accelerations and head responses can also support the effective development of helmet design.

6 Conclusions and Future Works

6.1 Conclusions

Continuous studies have been reported to improve helmet design to achieve better protection performance to prevent head injury during impact accidents, however, little attention has been paid to the efficiency and reliability design for the helmet from the material level. After a literature review on the related studies of helmet design, some research gaps are identified, such as inefficient full factorial optimisation method based on simplified head-helmet modelling, no analytical method model available for the quick characterisation and analysis of potential advanced impact-attenuating material for helmet design, and the need of a deeper understanding of head injury mechanisms to support the effective helmet evolution. Based on identified research gaps, this thesis aims to investigate the methodologies from three main underpinning aspects that can improve the reliable and efficient design of helmet against head injury. According to the undertaken studies, the conclusions are drawn as follows.

6.1.1 Head-helmet coupled modelling with optimisation

This chapter aims to develop an efficient optimisation methodology based on coupled head-helmet modelling for the efficient and reliable design of a novel helmet against head kinematic-based and tissue-level injury predictors. A representative full-face motorcycle helmet FE model was established and validated by the standard drop tests. Based on the validated helmet model, the Hybrid III head-helmet model and THUMS head-helmet

model were developed to measure the head kinematics and tissue-level responses, respectively. This head-helmet modelling method can be used to replace the time-consuming, expensive and inflexible experimental helmet design, and meanwhile output a wide range of mechanical response signals at any position. Thus, a novel honeycomb-filled helmet design was investigated using head-helmet modelling to illustrate the optimisation methodology. It was found that a reasonable design of aluminium honeycomb filler can improve the performance of helmet protection in terms of head kinematics and tissue-level responses. Furthermore, an orthogonal array design optimisation method based on head-helmet modelling was developed to efficiently find the optimal helmet design. This chapter provides an efficient orthogonal array design optimisation method based on the high biofidelity head-helmet modelling, which can be used to increase the computational efficiency by calculating the representative design combinations and improve the reliability of helmet design by considering both head kinematics and the advanced tissue-level injury predictors.

6.1.2 Analytical method for functionally graded polymeric foam

This chapter aims to provide a possible analytical solution to quickly characterise the mechanical responses of the potential advanced impact-attenuating material (i.e. FGPF), to improve the efficiency of material selection and analysis for helmet design. The FGPF is made from EPS foam, which is the most common helmet liner foam, was selected as a representative foam in this chapter. The constitutive model for uniform-density EPS foam under uniaxial compression was developed and then validated by the uniaxial quasi-static and dynamic compression experiments. Based on the assumption that FGPF is a combination of numerous independent uniform-density EPS foam layers, the idealised rigid-perfectly plastic-locking model was adopted to develop an analytical model for predicting the stress-strain correlations of FGPF under uniaxial compressive loads. Then, the FGPF FE model was established to validate the proposed analytical model. It was

demonstrated that the analytical model can be applied to quickly and accurately predict the compressive responses of FGPF under the loading conditions of low to moderate strain-rates. This chapter also showed that FGPF can be designed using the orthogonal array design optimisation method to maximise its crashworthiness performance. The proposed analytical method and the optimisation procedure could be also used for other functionally graded foam materials.

6.1.3 Head responses subjected to acceleration loads

This chapter aims to provide a quantitative numerical method to investigate the interactive effects of different frontal translational acceleration loading configurations on head responses, and to further explore the head injury mechanisms under impact loads to support the effective improvement of helmet design. A series of frontal translational accelerations defined by impact duration and peak magnitude with different loading curve shapes were applied to the THUMS head model to replicate different head impact responses in accidents. The influences of frontal translational acceleration loading configurations on the tissue-level injury predictors (i.e. ICP, σ_v and ε_p) were studied. Based on the thresholds for tissue-level injury predictors, it was found that both ICP-induced and ε_p-induced head injuries may occur whereas the σ_v-induced head injury is less likely to occur. The correlations between HIC and tissue-level responses were also analysed, and a good correlation was found between HIC and the ε_p responses for the head model under the frontal translational acceleration loads. This chapter exemplifies a quantitative numerical method that can provide a rapid estimation of head impact responses based on the frontal translational acceleration loads, which can further support effective helmet design with a deeper understanding of head injury mechanisms.

6.2 Future works

The findings presented in this thesis collectively provide some new insights into head impact injury and helmet protection performance in accidents. Despite the studies of these important aspects, some parts of this research still require a more thorough investigation. The following topics are recommended for future investigation.

1. This thesis only investigated the protection performance of honeycomb-filled helmets subjected to frontally impact onto the flat anvil, whereas the mechanical behaviours of honeycomb filler can be significantly influenced by the different loading conditions, including impact direction, impact velocity, the shape of impact anvil, etc. Thus, the honeycomb-filled helmet impacted frontally and obliquely onto different standard anvils (e.g. kerbstone and hemispherical anvils) with different loading velocities can be further studied, and the head rotational motion also needs to be considered in future.

2. The compression characteristics of FGPF can be predicted using the proposed analytical model, which can improve the efficiency of material selection and analysis for helmet design. Since the FGPF design must assure helmet performance over a wide of temperatures, the temperature effects on the mechanical characteristics of FGPF are worthy of future study. In addition, future work could introduce FGPF to a new helmet liner design based on the head-helmet FE modelling, and then the efficient orthogonal array design optimisation method could be employed to find the feasibly optimised FGPF configuration to further improve the helmet impact protection.

3. In the present study on head impact responses under different acceleration loading conditions, only the frontal translational acceleration loads were discussed, whereas the rotational acceleration loads have not been considered. However, rotational

accelerations also frequently occur in real-world head impact accidents and lead to severe head injury; meanwhile, the head responses are also sensitive to the impact direction. Thus, future studies can be carried out to investigate the influences of rotational motion on head injury and its combined effects with translational motion on head injury. The effects of impact direction on head injury are also recommended.

References

[1]   WHO. Global status report on road safety 2018: Summary. World Health Organization; 2018.

[2]   Wang F, Wang Z, Hu L, Xu H, Yu C, Li F. Evaluation of head injury criteria for injury prediction effectiveness: computational reconstruction of real-world vulnerable road user impact accidents. Frontiers in bioengineering and biotechnology. 2021;9:1-16.

[3]   Maas A, Menon D. A few facts about TBI. CENTER-TBI website. Available at: https://www.center-tbi.eu/. (accessed on 18 January 2022).

[4]   Centers for Disease C, Prevention. Report to congress on traumatic brain injury in the United States: epidemiology and rehabilitation. National Center for Injury Prevention and Control. 2015;2:1-72.

[5]   Wu X, Hu J, Zhuo L, Fu C, Hui G, Wang Y, Yang W, Teng L, Lu S, Xu G. Epidemiology of traumatic brain injury in eastern China, 2004: a prospective large case study. Journal of Trauma and Acute Care Surgery. 2008;64:1313-9.

[6]   Maas AIR, Menon DK, Adelson PD, Andelic N, Bell MJ, Belli A, Bragge P, Brazinova A, Büki A, Chesnut RM, Citerio G, Coburn M, Cooper DJ, Crowder AT, et al. Traumatic brain injury: integrated approaches to improve prevention, clinical care, and research. The Lancet Neurology. 2017;16:987-1048.

[7]   Hyder AA, Wunderlich CA, Puvanachandra P, Gururaj G, Kobusingye OC. The impact of traumatic brain injuries: a global perspective. NeuroRehabilitation. 2007;22:341-53.

[8]   Murphy A. Reported road casualties in Great Britain: 2019 annual report. Department of Transport. 2020.

[9]   Baker CE, Martin P, Wilson MH, Ghajari M, Sharp DJ. The relationship between road traffic collision dynamics and traumatic brain injury pathology. Brain Communications. 2022;4:1-20.

[10]   Liu BC, Ivers R, Norton R, Boufous S, Blows S, Lo SK. Helmets for preventing injury in motorcycle riders. Cochrane database of systematic reviews. 2008.

[11]   MSF, Motorcycle Safety Foundation, 2002. What you should know about motorcycle helmets. Cycle Safety Information, California, USA, Available at: https://www.msf-usa.org/downloads/helmet_CSI.pdf. (accessed on 18 January 2022).

[12]   Fernandes FA, Alves de Sousa RJ. Motorcycle helmets – A state of the art review. Accident Analysis and Prevention. 2013;56:1-21.

[13] Newman J. The biomechanics of head trauma and the development of the modern helmet. How far have we really come. Proceedings of the IRCOBI Conference 2005. p. 1-6.

[14] Kanesalingam S, Nayak R. Review of literature: motorcycle helmet. Singapore: Springer Singapore; 2020. p. 7-61.

[15] Kongwat S, Nueanim T, Hasegawa H. FE analysis of motorcycle helmet performance under severe accidents. Applied Sciences. 2022;12:5676.

[16] Shuaeib FM, Hamouda AMS, Radin Umar RS, Hamdan MM, Hashmi MSJ. Motorcycle helmet: Part I. Biomechanics and computational issues. Journal of Materials Processing Technology. 2002;123:406-21.

[17] Ghajari M, Peldschus S, Galvanetto U, Iannucci L. Effects of the presence of the body in helmet oblique impacts. Accident Analysis and Prevention. 2013;50:263-71.

[18] Gao W, Wang J, He X, Feng YT, Chen S, Wang C. Modeling the mechanical behavior of a helmeted headform impacted with a laminated windshield with consideration of composite failure. Composite Structures. 2022;279:114787.

[19] ECE 22.05. Uniform provision concerning the approval of protective helmets and their visors for driver and passengers of motor cycles and mopeds. Geneva: UN Economic Commission for Europe; 2002.

[20] FMVSS 218. Federal Motor Vehicle Safety Standard (FMVSS) 218 – Laboratory procedure for motorcycle helmet testing. Washington, DC: National Highway Traffic Safety Administration, Department of Transportation, U.S.; 1984.

[21] BS 6658:1985. Specification for protective helmets for vehicle users. British Standard Institution, London; 1985.

[22] SNELL M2020. Standard for protective headgear for use with motorcycles and other motorized vehicles. Snell Memorial Foundation, Inc.; 2020.

[23] Morlock S, Schenk A, Klepser A, Schmidt A. Using 3D scanning for improved helmet design. 2016. p. 190-200.

[24] Caserta G. The use of honeycomb in the design of innovative helmets: Imperial College London, 2012.

[25] Tinard V, Deck C, Willinger R. New methodology for improvement of helmet performances during impacts with regards to biomechanical criteria. Materials & Design. 2012;37:79-88.

[26] Fernandes F, Alves de Sousa R, Ptak M, Migueis G. Helmet design based on the optimization of biocomposite energy-absorbing liners under multi-impact loading. Applied Sciences. 2019;9:735.

[27] Cui L, Forero Rueda MA, Gilchrist MD. Optimisation of energy absorbing liner for equestrian helmets. Part II: Functionally graded foam liner. Materials & Design. 2009;30:3414-9.

[28] Abayazid FF, Carpanen D, Ghajari M. New viscoelastic circular cell honeycombs for

controlling shear and compressive responses in oblique impacts. International Journal of Mechanical Sciences. 2022;222:107262.

[29] Khosroshahi SF, Tsampas SA, Galvanetto U. Feasibility study on the use of a hierarchical lattice architecture for helmet liners. Materials Today Communications. 2018;14:312-23.

[30] Deck C, Willinger R, Baumgartner D. Helmet optimisation based on head-helmet modelling. WIT Transactions on The Built Environment. 2003;67:319–28.

[31] Deck C, Willinger Rm. Multi-directional optimisation against biomechanical criteria of a head–helmet coupling. International Journal of Crashworthiness. 2006;11:561-72.

[32] Kleiven S. Predictors for traumatic brain injuries evaluated through accident reconstructions. Stapp Car Crash J. 2007;51:81-114.

[33] Farajzadeh Khosroshahi S, Galvanetto U, Ghajari M. Optimization of the chin bar of a composite-shell helmet to mitigate the upper neck force. Applied Composite Materials. 2016;24:931-44.

[34] Shuaeib FM, Hamouda AMS, Wong SV, Umar RSR, Ahmed MMHM. A new motorcycle helmet liner material: The finite element simulation and design of experiment optimization. Materials & Design. 2007;28:182-95.

[35] Kholoosi F, Galehdari SA. Design, optimisation and analysis of a helmet made with graded honeycomb structure under impact load. International Journal of Crashworthiness. 2019;24:645-55.

[36] Forero Rueda MA, Cui L, Gilchrist MD. Optimisation of energy absorbing liner for equestrian helmets. Part I: Layered foam liner. Materials & Design. 2009;30:3405-13.

[37] Clough EC, Plaisted TA, Eckel ZC, Cante K, Hundley JM, Schaedler TA. Elastomeric microlattice impact attenuators. Matter. 2019;1:1519-31.

[38] Zheng G, Zhang X, Li S, Pang T, Li Q, Sun G. Correlation between kinematics and biomechanics of helmeted head under different impact conditions. Composite Structures. 2022;291:115514.

[39] Trotta A, Clark JM, McGoldrick A, Gilchrist MD, Annaidh AN. Biofidelic finite element modelling of brain trauma: Importance of the scalp in simulating head impact. International Journal of Mechanical Sciences. 2020;173:105448.

[40] Whyte T, Gibson T, Milthorpe B, Stanford G. Head injury and effective motorcycle helmets. 23rd Enhanced Safety of Vehicles Conference, Seoul, Korea 2013. p. 27-30.

[41] Caroline D, Rémy W. Head injury prediction tool for protective systems optimisation. 7th European LS-DYNA Conference 2009. p. 14-5.

[42] Caserta GD, Iannucci L, Galvanetto U. Shock absorption performance of a motorbike helmet with honeycomb reinforced liner. Composite Structures. 2011;93:2748-59.

[43] Mills NJ. Polymer foams handbook: engineering and biomechanics applications and design guide. 1st ed. Oxford: Butterworth Heinemann, 2007.

[44] Moore KL, Dalley AF. Clinically oriented anatomy: Wolters kluwer india Pvt Ltd, 2018.

[45] Antranik org. Protection for the Brain: Meninges, CSF, Blood-Brain Barrier. Available at: https://antranik.org/protection-for-the-brain-meninges-csf-blood-brain-barrier/. (accessed on 18 January 2022).

[46] Encyclopædia Britannica, Inc. Lateral (left) and frontal (right) views of the human skull. Available at: https://www.britannica.com/science/human-skeleton/Axial-and-visceral-skeleton. (accessed on 18 January 2022).

[47] Saladin KS. The brain and cranial nerves. Human Anatomy International Edition ed. 2007:414-51.

[48] Bilston LE. An introduction to the biomechanics of the nervous system. In: Bilston LE, editor. Neural Tissue Biomechanics. Berlin, Heidelberg: Springer; 2011. p. 1-9.

[49] Saladin KS, Miller L. Anatomy & physiology: WCB/McGraw-Hill New York, 1998.

[50] Simms C, Wood D. Injury mechanisms and injury criteria. Pedestrian and Cyclist Impact: A Biomechanical Perspective. 2009:75-97.

[51] Schmitt K-U, Niederer PF, Cronin DS, Muser MH, Walz F. Trauma biomechanics: an introduction to injury biomechanics. Berlin: Springer, 2014.

[52] Gennarelli TA. The pathobiology of traumatic brain injury. The Neuroscientist. 1997;3:73-81.

[53] Davis AE. Mechanisms of traumatic brain injury: biomechanical, structural and cellular considerations. Critical care nursing quarterly. 2000;23:1-13.

[54] Fan L, Honggeng L, Zhi X, Ronggui L, Zhiteng Z, Haiyun Z, Lihai R. A review on injury mechanism of intracerebral hemorrhage in vehicle accidents. Current Pharmaceutical Design. 2017;23:2177-92.

[55] Fernandes FAO, Sousa RJAd. Head injury predictors in sports trauma – A state-of-the-art review. Proceedings of the Institution of Mechanical Engineers, Part H: Journal of Engineering in Medicine. 2015;229:592-608.

[56] Melvin JW, Yoganandan N. Biomechanics of brain injury: a historical perspective. Accidental injury: Springer; 2015. p. 221-45.

[57] King AI. The biomechanics of impact injury : biomechanical response, mechanisms of injury, human tolerance and simulation. 1st ed. Cham: Springer International Publishing, 2018.

[58] Kleiven S. Why most traumatic brain injuries are not caused by linear acceleration but skull fractures are. Frontiers in bioengineering and biotechnology. 2013;1:1-5.

[59] Some types of head trauma. Available at: https://radiologyassistant.nl/neuroradiology/hemorrhage/traumatic-intracranial-haemorrhage. (accessed on 18 June 2022).

[60] Levin HS, Li X, McCauley SR, Hanten G, Wilde EA, Swank P. Neuropsychological outcome of mTBI: a principal component analysis approach. Journal of Neurotrauma.

2013;30:625-32.

[61] Ommaya AK, Gennarelli TA. Cerebral concussion and traumatic unconsciousness: correlation of experimental and clinical observations on blunt head injuries. Brain. 1974;97:633-54.

[62] Tse KM, Lim SP, Tan VBC, Lee HP. A review of head injury and finite element head models. American Journal of Engineering, Technology and Society. 2014;1:28-52.

[63] Ommaya AK, Thibault L, Bandak FA. Mechanisms of impact head injury. International Journal of Impact Engineering. 1994;15:535-60.

[64] Yanagida Y, Fujiwara S, Mizoi Y. Differences in the intracranial pressure caused by a 'blow'and/or a 'fall'—an experimental study using physical models of the head and neck. Forensic Science International. 1989;41:135-45.

[65] Levadnyi I, Awrejcewicz J, Zhang Y, Goethel MF, Gu Y. Finite element analysis of impact for helmeted and non-helmeted head. Journal of medical and biological engineering. 2018;38:587-95.

[66] Gabler LF, Crandall JR, Panzer MB. Assessment of kinematic bain injury metrics for pedicting strain responses in diverse automotive impact conditions. Annals of Biomedical Engineering. 2016;44:3705-18.

[67] Gurdjian ES, Roberts VL, Thomas LM. Tolerance curves of acceleration and intracranial pressure and protective index in experimental head injury. Journal of Trauma and Acute Care Surgery. 1966;6:600-4.

[68] Gadd CW. Use of a weighted-impulse criterion for estimating injury hazard. SAE technical paper; 1966. p. 164-74.

[69] Cory CZ, Jones MD, James DS, Leadbeatter S, Nokes LDM. The potential and limitations of utilising head impact injury models to assess the likelihood of significant head injury in infants after a fall. Forensic Science International. 2001;123:89-106.

[70] Hutchinson J, Kaiser MJ, Lankarani HM. The Head Injury Criterion (HIC) functional. Applied Mathematics and Computation. 1998;96:1-16.

[71] FMVSS 208. Federal Motor Vehicle Safety Standard (FMVSS) 208 – Occupant crash protection. Washington, DC: National Highway Traffic Safety Administration, Department of Transportation, U.S.; 1972.

[72] Newman JA. A generalized acceleration model for brain injury threshold (GAMBIT). International IRCOBI Conference 1986.

[73] Newman JA, Shewchenko N. A proposed new biomechanical head injury assessment function-the maximum power index. SAE Technical Paper; 2000.

[74] Sanchez EJ, Gabler LF, McGhee JS, Olszko AV, Chancey VC, Crandall JR, Panzer MB. Evaluation of head and brain injury risk functions using sub-injurious human volunteer data. Journal of Neurotrauma. 2017;34:2410-24.

[75] Takhounts EG, Craig MJ, Moorhouse K, McFadden J, Hasija V. Development of Brain

Injury Criteria (BrIC). The Stapp Association; 2013. p. 243-66.

[76]   Dixit P, Liu GR. A review on recent development of finite element models for head injury simulations. Archives of Computational Methods in Engineering. 2017;24:979-1031.

[77]   Kleiven S. Influence of impact direction on the human head in prediction of subdural hematoma. Journal of Neurotrauma. 2003;20:365-79.

[78]   Atlan LS, Smith C, Margulies SS. Improved prediction of direction-dependent, acute axonal injury in piglets. Journal of neuroscience research. 2018;96:536-44.

[79]   Lissner HR, Lebow M, Evans FG. Experimental studies on the relation between acceleration and intracranial pressure changes in man. Surgery, gynecology & obstetrics. 1960;111:329-38.

[80]   Nahum AM, Smith RW. An experimental model for closed head impact injury. SAE Transactions. 1976:2638-51.

[81]   Nahum AM, Smith R, Ward CC. Intracranial pressure dynamics during head impact. Proceedings of the 21st Stapp Car Crash Conference: SAE Technical Paper; 1977. p. 338-66.

[82]   Khalil TB, Viano DC, Smith DL. Experimental analysis of the vibrational characteristics of the human skull. Journal of Sound and Vibration. 1979;63:351-76.

[83]   Trosseille X, Tarriere C, Lavaste F, Guillon F, Domont A. Development of a FEM of the human head according to a specific test protocol. SAE Transactions. 1992;101:1801-19.

[84]   Hardy WN, Foster CD, Mason MJ, Yang KH, King AI, Tashman S. Investigation of head injury mechanisms using neutral density technology and high-speed biplanar X-ray. Stapp Car Crash J. 2001;45:337-68.

[85]   Hardy WN, Mason MJ, Foster CD, Shah CS, Kopacz JM, Yang KH, King AI, Bishop J, Bey M, Anderst W, Tashman S. A study of the response of the human cadaver head to impact. Stapp Car Crash J. 2007;51:17-80.

[86]   Gadd CW. Use of a weighted-impulse criterion for estimating injury hazard. SAE technical paper; 1966 p. 660739.

[87]   Versace J. A review of the severity index. SAE Technical Paper; 1971.

[88]   Chou CC, Nyquist GW. Analytical studies of the Head Injury Criterion (HIC). SAE Transactions. 1974:398-410.

[89]   Zhou Q, Thomas MP, Stibich AM. An analytical study of system variables for meeting FMVSS 201 head impact requirements. ASME Applied Mechanics Division Publications. 1998;229:131-9.

[90]   Wu J, Beaudet B. Optimization of head impact waveform to minimize HIC. Detroit, Michigan: SAE Technical Paper; 2007. p. 2007-01-0759.

[91]   Yang C, Li QM. Further assessment of deceleration-time histories for occupant injury and the damage of protected object in a crash stop. International Journal of Impact Engineering. 2019;130:184-91.

[92]   Yang KH. Basic finite element method as applied to injury biomechanics. Amsterdam: Academic Press, 2017.

[93]   Yang B, Tse KM, Chen N, Tan LB, Zheng QQ, Yang HM, Hu M, Pan G, Lee HP. Development of a finite element head model for the study of impact head injury. Biomed Research International. 2014;2014:408278.

[94]   Fernandes FAO, Tchepel D, Alves de Sousa RJ, Ptak M. Development and validation of a new finite element human head model. Engineering Computations. 2018;35:477-96.

[95]   Kleiven S. Evaluation of head injury criteria using a finite element model validated against experiments on localized brain motion, intracerebral acceleration, and intracranial pressure. International Journal of Crashworthiness. 2006;11:65-79.

[96]   Meng S, Cernicchi A, Kleiven S, Halldin P. The biomechanical differences of shock absorption test methods in the US and European helmet standards. International Journal of Crashworthiness. 2019;24:399-412.

[97]   Xiao Z, Wang L, Zhang Y, Yang C. A study on motorcyclist head reponses during impact against front end of vehicle. International Journal of Crashworthiness. 2020:1-13.

[98]   Yu X, Logan I, de Pedro Sarasola I, Dasaratha A, Ghajari M. The protective performance of modern motorcycle helmets under oblique impacts. Annals of Biomedical Engineering. 2022:1-15.

[99]   Madhukar A, Ostoja-Starzewski M. Finite element methods in human head impact simulations: a review. Annals of Biomedical Engineering. 2019;47:1832-54.

[100]   Ruan JS, Khalil TB, King AI. Finite element modeling of direct head impact. SAE Technical Paper; 1993. p. 69-81.

[101]   Zhou C, Khalil TB, King AI. A new model comparing impact responses of the homogeneous and inhomogeneous human brain. SAE Transactions. 1995:2999-3015.

[102]   Zhang L, Yang KH, Dwarampudi R, Omori K, Li T, Chang K, Hardy WN, Khalil TB, King AI. Recent advances in brain injury research: a new human head model development and validation. SAE Technical Paper; 2001. p. 1-25.

[103]   Viano DC, Casson IR, Pellman EJ, Zhang L, King AI, Yang KH. Concussion in professional football: brain responses by finite element analysis: part 9. Neurosurgery. 2005;57:891-916.

[104]   Mao H, Zhang L, Jiang B, Genthikatti VV, Jin X, Zhu F, Makwana R, Gill A, Jandir G, Singh A, Yang KH. Development of a finite element human head model partially validated with thirty five experimental cases. Journal of Biomechanical Engineering. 2013;135:111002.

[105]   Mao H, Gao H, Cao L, Genthikatti VV, Yang KH. Development of high-quality hexahedral human brain meshes using feature-based multi-block approach. Computer Methods in Biomechanics and Biomedical Engineering. 2013;16:271-9.

[106]   Ji S, Ghadyani H, Bolander RP, Beckwith JG, Ford JC, McAllister TW, Flashman LA,

Paulsen KD, Ernstrom K, Jain S, Raman R, Zhang L, Greenwald RM. Parametric comparisons of intracranial mechanical responses from three validated finite element models of the human head. Annals of Biomedical Engineering. 2014;42:11-24.

[107] Fredriksson R, Zhang L, Boström O, Yang K. Influence of impact speed on head and brain injury outcome in vulnerable road user impacts to the car hood. SAE Technical Paper; 2007.

[108] Gabler LF, Crandall JR, Panzer MB. Development of a second-order system for rapid estimation of maximum brain strain. Annals of Biomedical Engineering. 2019;47:1971-81.

[109] Sahoo D, Deck C, Yoganandan N, Willinger R. Anisotropic composite human skull model and skull fracture validation against temporo-parietal skull fracture. Journal of the Mechanical Behavior of Biomedical Materials. 2013;28:340-53.

[110] Kang HS, Willinger R, Diaw BM, Chinn B. Validation of a 3D anatomic human head model and replication of head impact in motorcycle accident by finite element modeling. SAE Technical Paper; 1997. p. 329-38.

[111] Bourdet N, Deck C, Serre T, Perrin C, Llari M, Willinger R. In-depth real-world bicycle accident reconstructions. International Journal of Crashworthiness. 2013;19:222-32.

[112] Tinard V, Deck C, Meyer F, Bourdet N, Willinger R. Influence of pedestrian head surrogate and boundary conditions on head injury risk prediction. International Journal of Crashworthiness. 2009;14:259-68.

[113] Marjoux D, Baumgartner D, Deck C, Willinger R. Head injury prediction capability of the HIC, HIP, SIMon and ULP criteria. Accident Analysis and Prevention. 2008;40:1135-48.

[114] Kleiven S, von Holst H. Consequences of head size following trauma to the human head. Journal of Biomechanics. 2002;35:153-60.

[115] Kleiven S, von Holst H. Consequences of brain size following impact in prediction of subdural hematoma evaluated with numerical techniques. Proceedings of the International Conference on the Biomechanics of Impact (IRCOBI'01), 2001. p. 161-72.

[116] Li XG, Gao XL, Kleiven S. Behind helmet blunt trauma induced by ballistic impact: A computational model. International Journal of Impact Engineering. 2016;91:56-67.

[117] Meng S, Fahlstedt M, Halldin P. The effect of impact velocity angle on helmeted head impact severity: a rationale for motorcycle helmet impact test design. 2018 International Research Council on the Biomechanics of Injury (IRCOBI 2018), 2018. p. 454-69.

[118] Zhou Z, Li X, Kleiven S. Fluid-structure interaction simulation of the brain-skull interface for acute subdural haematoma prediction. Biomechanics and Modeling in Mechanobiology. 2018;18:155-73.

[119] Zhou Z, Li X, Kleiven S. Biomechanics of acute subdural hematoma in the elderly: A fluid-structure interaction study. Journal of Neurotrauma. 2019;36:2099-108.

[120] Kleiven S. Influence of direction and duration of impacts to the human head evaluated

using the finite element method. International IRCOBI Conference 2005. p. 41-57.

[121] Kimpara H, Nakahira Y, Iwamoto M, Miki K, Ichihara K, Kawano S-i, Taguchi T. Investigation of anteroposterior head-neck responses during severe frontal impacts using a brain-spinal cord complex FE model. SAE Technical Paper; 2006. p. 509-44.

[122] Iwamoto M, Kisanuki Y, Watanabe I, Furusu K, Miki K, Hasegawa J. Development of a finite element model of the total human model for safety (THUMS) and application to injury reconstruction. Proceedings of the international IRCOBI Conference 2002.

[123] Kato D, Nakahira Y, Atsumi N, Iwamoto M. Development of human-body model THUMS Version 6 containing muscle controllers and application to injury analysis in frontal collision after brake deceleration. IRCOBI Conference 2018. p. 207-23.

[124] Iwamoto M, Nakahira Y. Development and validation of the Total Human Model for Safety (THUMS) version 5 containing multiple 1D muscles for estimating occupant motions with muscle activation during side impacts. SAE Technical Paper; 2015. p. 53-90.

[125] Atsumi N, Nakahira Y, Iwamoto M. Development and validation of a head/brain FE model and investigation of influential factor on the brain response during head impact. International journal of vehicle safety. 2016;9:1-23.

[126] Deng G, Wang F, Yu C, Peng Y, Xu H, Li Z, Hou L, Wang Z. Assessment of standing passenger traumatic brain injury caused by ground impact in subway collisions. Accident Analysis & Prevention. 2022;166:106547.

[127] Ren L, Wang D, Liu X, Yu H, Jiang C, Hu Y. Influence of skull fracture on traumatic brain injury risk induced by blunt impact. International Journal of Environmental Research and Public Health. 2020;17:2392.

[128] Shang S, Zheng Y, Shen M, Yang X, Xu J. Numerical investigation on head and brain injuries caused by windshield impact on riders using electric self-balancing scooters. Applied Bionics Biomechanics. 2018;2018:5738090.

[129] Ghajari M, Peldschus S, Galvanetto U, Asgharpour Z, Iannucci L. Influence of the body on head rotational acceleration in motorcycle helmet oblique impact tests. IRCOBI Conference 2010. Hanover, Germany 2010. p. 95-106.

[130] Ghajari M, Galvanetto U, Iannucci L, Willinger Rm. Intracranial response in helmet oblique impacts. IRCOBI Conference 2011. Warsaw, Poland 2011. p. 90-4.

[131] Ghajari M, Hellyer PJ, Sharp DJ. Computational modelling of traumatic brain injury predicts the location of chronic traumatic encephalopathy pathology. Brain. 2017;140:333-43.

[132] Abayazid F, Ding K, Zimmerman K, Stigson H, Ghajari M. A new assessment of bicycle helmets: the brain injury mitigation effects of new technologies in oblique impacts. Annals of Biomedical Engineering. 2021;49:2716-33.

[133] Fahlstedt M, Abayazid F, Panzer MB, Trotta A, Zhao W, Ghajari M, Gilchrist MD, Ji S, Kleiven S, Li X, Annaidh AN, Halldin P. Ranking and rating bicycle helmet safety performance in oblique impacts using eight different brain injury models. Annals of

Biomedical Engineering. 2021;49:1097-109.

[134] Yu X, Wu T, Nguyen T-TN, Ghajari M. Investigation of blast-induced cerebrospinal fluid cavitation: Insights from a simplified head surrogate. International Journal of Impact Engineering. 2022;162:104146.

[135] Yu X, Ghajari M. An assessment of blast modelling techniques for injury biomechanics research. International journal for numerical methods in biomedical engineering. 2019;35:e3258.

[136] Yu X, Azor A, J Sharp D, Ghajari M. Mechanisms of tensile failure of cerebrospinal fluid in blast traumatic brain injury. Extreme Mechanics Letters. 2020;38:100739.

[137] Levy Y, Bian K, Patterson L, Ouckama R, Mao H. Head kinematics and injury metrics for laboratory hockey-relevant head impact experiments. Annals of Biomedical Engineering. 2021:2914-23.

[138] Ghajari M, Peldschus S, Galvanetto U, Iannucci L. Evaluation of the effective mass of the body for helmet impacts. International Journal of Crashworthiness. 2011;16:621-31.

[139] Zhou Z, Jiang B, Cao L, Zhu F, Mao H, Yang KH. Numerical simulations of the 10-year-old head response in drop impacts and compression tests. Computer Methods and Programs in Biomedicine. 2016;131:13-25.

[140] Meng S, Cernicchi A, Kleiven S, Halldin P. High-speed helmeted head impacts in motorcycling: A computational study. Accident Analysis & Prevention. 2020;134:105297.

[141] Wang J, Wang R, Gao W, Chen S, Wang C. Numerical investigation of impact injury of a human head during contact interaction with a windshield glazing considering mechanical failure. International Journal of Impact Engineering. 2020;141:103577.

[142] Khosroshahi SF, Duckworth H, Galvanetto U, Ghajari M. The effects of topology and relative density of lattice liners on traumatic brain injury mitigation. Journal of Biomechanics. 2019;97:109376.

[143] Li S, Xiao Z, Zhang Y, Li QM. Impact analysis of a honeycomb-filled motorcycle helmet based on coupled head-helmet modelling. International Journal of Mechanical Sciences. 2021;199:106406.

[144] Post A, Hoshizaki B, Gilchrist MD. Finite element analysis of the effect of loading curve shape on brain injury predictors. Journal of Biomechanics. 2012;45:679-83.

[145] Post A, Blaine Hoshizaki T, Gilchrist MD, Cusimano MD. Peak linear and rotational acceleration magnitude and duration effects on maximum principal strain in the corpus callosum for sport impacts. Journal of Biomechanics. 2017;61:183-92.

[146] Bian K, Mao H. Mechanisms and variances of rotation-induced brain injury: a parametric investigation between head kinematics and brain strain. Biomechanics and Modeling in Mechanobiology. 2020;19:2323-41.

[147] Carlsen RW, Fawzi AL, Wan Y, Kesari H, Franck C. A quantitative relationship between rotational head kinematics and brain tissue strain from a 2-D parametric finite element

analysis. Brain Multiphysics. 2021;2:100024.

[148] Yoganandan N, Li J, Zhang J, Pintar FA, Gennarelli TA. Influence of angular acceleration–deceleration pulse shapes on regional brain strains. Journal of Biomechanics. 2008;41:2253-62.

[149] Yu X, Ghajari M. Protective performance of helmets and goggles in mitigating brain biomechanical response to primary blast exposure. Annals of Biomedical Engineering. 2022:1-17.

[150] Ghajari M, Galvanetto U, Iannucci L. Influence of the body on kinematic and tissue level head injury predictors in motorcyclists accidents. Proceedings of IRCOBI Conference, . York, UK 2009. p. 275-86.

[151] Mohan P, Park C-K, Marzougui D, Kan C-D, Guha S, Maurath C, Bhalsod D. LSTC/NCAC dummy model development. 11th International LS-DYNA Users Conference 2010. p. 53-64.

[152] Shuaeib F, Hamouda A, Hamdan M, Umar RR, Hashmi M. Motorcycle helmet: Part II. Materials and design issues. Journal of Materials Processing Technology. 2002;123:422-31.

[153] Blanco DH, Cernicchi A, Galvanetto U. FE modeling of innovative helmet liners. 11th International LS-DYNA users conference 2010. p. 1-11.

[154] Tinard V, Deck C, Willinger R. Modelling and validation of motorcyclist helmet with composite shell. International Journal of Crashworthiness. 2012;17:209-15.

[155] Rahmanifar N, Eskandari F, Shafieian M. Mechanical Characterization of Expanded Polystyrene (EPS) as a Liner Foam in Motorcycle Helmets. 27th National and 5th International Iranian Conference on Biomedical Engineering (ICBME). Tehran, Iran: IEEE; 2020. p. 79-82.

[156] Juste-Lorente Ó, Maza M, Piqueras A, Lorente AI, López-Valdés FJ. Effects of including a penetration test in motorcyclist helmet standards: influence on helmet stiffness and impact performance. Applied Sciences. 2022;12:2455.

[157] Chang LT, Chang GL, Huang JZ, Huang SC, Liu DS, Chang CH. Finite element analysis of the effect of motorcycle helmet materials against impact velocity. Journal of the Chinese Institute of Engineers. 2003;26:835-43.

[158] Bonin SJ, Luck JF, Bass CR, Gardiner JC, Onar-Thomas A, Asfour SS, Siegmund GP. Dynamic response and residual helmet liner crush using cadaver heads and standard headforms. Annals of Biomedical Engineering. 2017;45:656-67.

[159] Gohel G, Bhudolia SK, Elisetty SBS, Leong KF, Gerard P. Development and impact characterization of acrylic thermoplastic composite bicycle helmet shell with improved safety and performance. Composites Part B: Engineering. 2021;221:109008.

[160] Obi BE. Polymeric foams structure-property-performance : a design guide. Oxford: William Andrew, imprint of Elsevier, 2018.

[161] DeMarco AL, Chimich DD, Gardiner JC, Nightingale RW, Siegmund GP. The impact response of motorcycle helmets at different impact severities. Accident Analysis and Prevention. 2010;42:1778-84.

[162] Gilchrist A, Mills NJ. Protection of the side of the head. Accident Analysis & Prevention. 1996;28:525-35.

[163] Fernandes F, Alves de Sousa R. Finite element analysis of helmeted oblique impacts and head injury evaluation with a commercial road helmet. Structural Engineering and Mechanics. 2013;48:661-79.

[164] Kostopoulos V, Markopoulos YP, Giannopoulos G, Vlachos DE. Finite element analysis of impact damage response of composite motorcycle safety helmets. Composites Part B: Engineering. 2002;33:99-107.

[165] Cui L, Kiernan S, Gilchrist MD. Designing the energy absorption capacity of functionally graded foam materials. Materials Science and Engineering: A. 2009;507:215-25.

[166] Ha NS, Lu G. A review of recent research on bio-inspired structures and materials for energy absorption applications. Composites Part B: Engineering. 2020;181:107496.

[167] Libonati F, Buehler MJ. Advanced structural materials by bioinspiration. Advanced Engineering Materials. 2017;19:1600787.

[168] Yin K, Mylo MD, Speck T, Wegst UGK. Bamboo-inspired tubular scaffolds with functional gradients. Journal of the Mechanical Behavior of Biomedical Materials. 2020;110:103826.

[169] Zhang W, Yin S, Yu TX, Xu J. Crushing resistance and energy absorption of pomelo peel inspired hierarchical honeycomb. International Journal of Impact Engineering. 2019;125:163-72.

[170] Jiang H, Ren Y, Jin Q, Zhu G, Hu Y, Cheng F. Crashworthiness of novel concentric auxetic reentrant honeycomb with negative Poisson's ratio biologically inspired by coconut palm. Thin-Walled Structures. 2020;154:106911.

[171] Xu F, Zhang X, Zhang H. A review on functionally graded structures and materials for energy absorption. Engineering Structures. 2018;171:309-25.

[172] Gross J, Timberg R, Graef M. Pigment and ultrastructural changes in the developing pummelo Citrus grandis' Goliath'. Botanical Gazette. 1983;144:401-6.

[173] Thielen M, Schmitt CNZ, Eckert S, Speck T, Seidel R. Structure–function relationship of the foam-like pomelo peel (Citrus maxima) — an inspiration for the development of biomimetic damping materials with high energy dissipation. Bioinspiration & Biomimetics. 2013;8:025001.

[174] Thielen M, Speck T, Seidel R. Viscoelasticity and compaction behaviour of the foam-like pomelo (Citrus maxima) peel. Journal of Materials Science. 2013;48:3469-78.

[175] Gupta N. A functionally graded syntactic foam material for high energy absorption under compression. Materials Letters. 2007;61:979-82.

[176] Sun G, Li G, Hou S, Zhou S, Li W, Li Q. Crashworthiness design for functionally graded foam-filled thin-walled structures. Materials Science and Engineering: A. 2010;527:1911-9.

[177] Yin H, Wen G, Hou S, Qing Q. Multiobjective crashworthiness optimization of functionally lateral graded foam-filled tubes. Materials & Design. 2013;44:414-28.

[178] Fang J, Gao Y, Sun G, Zhang Y, Li Q. Parametric analysis and multiobjective optimization for functionally graded foam-filled thin-wall tube under lateral impact. Computational Materials Science. 2014;90:265-75.

[179] Attia MS, Meguid SA, Nouraei H. Nonlinear finite element analysis of the crush behaviour of functionally graded foam-filled columns. Finite Elements in Analysis and Design. 2012;61:50-9.

[180] Zhang X, Zhang H. Optimal design of functionally graded foam material under impact loading. International Journal of Mechanical Sciences. 2013;68:199-211.

[181] Esmailzadeh M, Danesh Manesh H, Zebarjad SM. Fabrication and characterization of functional graded polyurethane foam (FGPUF). Polymers for advanced technologies. 2018;29:182-9.

[182] Yu X, Qin Q, Zhang J, Wang M, Xiang C, Wang T. Low-velocity impact of density-graded foam-filled square columns. International Journal of Crashworthiness. 2020:1-14.

[183] Koohbor B, Kidane A. Design optimization of continuously and discretely graded foam materials for efficient energy absorption. Materials & Design. 2016;102:151-61.

[184] Yin H, Wen G, Fang H, Qing Q, Kong X, Xiao J, Liu Z. Multiobjective crashworthiness optimization design of functionally graded foam-filled tapered tube based on dynamic ensemble metamodel. Materials & Design. 2014;55:747-57.

[185] Almasi D, Sadeghi M, Lau WJ, Roozbahani F, Iqbal N. Functionally graded polymeric materials: A brif review of current fabrication methods and introduction of a novel fabrication method. Materials Science and Engineering: C. 2016;64:102-7.

[186] Gibson LJ, Ashby MF. Cellular solids: structure and properties. Cambridge: Cambridge University Press, 1997.

[187] Schraad MW, Harlow FH. A stochastic constitutive model for disordered cellular materials: Finite-strain uni-axial compression. International Journal of Solids and Structures. 2006;43:3542-68.

[188] Kiernan S, Gilchrist MD. Towards a virtual functionally graded foam: Defining the large strain constitutive response of an isotropic closed cell polymeric cellular solid. International Journal of Engineering Science. 2010;48:1373-86.

[189] Chen D, Luo Q, Meng M, Sun G. Low velocity impact behavior of interlayer hybrid composite laminates with carbon/glass/basalt fibres. Composites Part B: Engineering. 2019;176:107191.

[190] Chen D, Sun G, Meng M, Jin X, Li Q. Flexural performance and cost efficiency of carbon/basalt/glass hybrid FRP composite laminates. Thin-Walled Structures. 2019;142:516-31.

[191] Pinnoji PK, Mahajan P. Analysis of impact-induced damage and delamination in the composite shell of a helmet. Materials & Design. 2010;31:3716-23.

[192] Tinard V, Deck C, Bourdet N, Willinger R. Motorcyclist helmet composite outer shell characterisation and modelling. Materials & Design. 2011;32:3112-9.

[193] Abderezaei J, Rezayaraghi F, Kain B, Menichetti A, Kurt M. An overview of the effectiveness of bicycle helmet designs in impact testing. Frontiers in bioengineering and biotechnology. 2021;9:718407.

[194] Folgar F. Thermoplastic matrix combat helmet with carbon-epoxy skin for ballistic performance. Advanced Fibrous Composite Materials for Ballistic Protection Woodhead Publishing; 2016. p. 437-56.

[195] Polanco-Loria M, Clausen AH, Berstad T, Hopperstad OS. Constitutive model for thermoplastics with structural applications. International Journal of Impact Engineering. 2010;37:1207-19.

[196] Matzenmiller A, Lubliner J, Taylor RL. A constitutive model for anisotropic damage in fiber-composites. Mechanics of Materials. 1995;20:125-52.

[197] Beusenberg MC, Happee R. An experimental evaluation of crash helmet design and effectiveness in standard impact tests. Proceedings of IRCOBI Conference Eindhoven, Netherlands 1993.

[198] Gilchrist A. Impact deformation of ABS and GRP motorcycle helmet shells. Plastics and Rubber Processing and Applications. 1994;21:141-50.

[199] Cernicchi A, Galvanetto U, Iannucci L. Virtual modelling of safety helmets: practical problems. International Journal of Crashworthiness. 2008;13:451-67.

[200] Chiu LNS, Falzon BG, Ruan D, Xu S, Thomson RS, Chen B, Yan W. Crush responses of composite cylinder under quasi-static and dynamic loading. Composite Structures. 2015;131:90-8.

[201] Van Den Bosch HLA. Crash helmet testing and design specifications: Eindhoven University of Technology, 2006.

[202] Sun G, Li S, Liu Q, Li G, Li Q. Experimental study on crashworthiness of empty/aluminum foam/honeycomb-filled CFRP tubes. Composite Structures. 2016;152:969-93.

[203] Zhang X, Zhang H, Wen Z. Experimental and numerical studies on the crush resistance of aluminum honeycombs with various cell configurations. International Journal of Impact Engineering. 2014;66:48-59.

[204] Sun G, Huo X, Chen D, Li Q. Experimental and numerical study on honeycomb sandwich panels under bending and in-panel compression. Materials & Design. 2017;133:154-68.

[205] Zhu G, Li S, Sun G, Li G, Li Q. On design of graded honeycomb filler and tubal wall thickness for multiple load cases. Thin-Walled Structures. 2016;109:377-89.

[206] Fang J, Sun G, Qiu N, Pang T, Li S, Li Q. On hierarchical honeycombs under out-of-plane crushing. International Journal of Solids and Structures. 2018;135:1-13.

[207] Kholoosi F, Galehdari SA. Design and analysis of a helmet equipped with graded honeycomb structure under impact of flat and hemi-spherical anvils. Procedia Engineering. 2017;173:1299-306.

[208] Iwamoto M, Nakahira Y, Tamura A, Kimpara H, Watanabe I, Miki K. Development of advanced human models in THUMS. 6th European LS-DYNA Users' Conference 2007. p. 47-56.

[209] Mills NJ, Gilchrist A. Response of helmets in direct and oblique impacts. International Journal of Crashworthiness. 1996;2:7-24.

[210] Pinnoji PK, Mahajan P, Bourdet N, Deck C, Willinger R. Impact dynamics of metal foam shells for motorcycle helmets: Experiments & numerical modeling. International Journal of Impact Engineering. 2010;37:274-84.

[211] Sun G, Chen D, Huo X, Zheng G, Li Q. Experimental and numerical studies on indentation and perforation characteristics of honeycomb sandwich panels. Composite Structures. 2018;184:110-24.

[212] SAE J211-1: instrumentation for impact test—Part 1—Electronic instrumentation. 2007.

[213] Jilin Y, Norman J. Further experimental investigations on the failure of clamped beams under impact loads. International Journal of Solids and Structures. 1991;27:1113-37.

[214] Jin X, Wang Z, Ning J, Xiao G, Liu E, Shu X. Dynamic response of sandwich structures with graded auxetic honeycomb cores under blast loading. Composites Part B: Engineering. 2016;106:206-17.

[215] Zhu F, Zhao L, Lu G, Gad E. A numerical simulation of the blast impact of square metallic sandwich panels. International Journal of Impact Engineering. 2009;36:687-99.

[216] Zhang D, Fei Q, Jiang D, Li Y. Numerical and analytical investigation on crushing of fractal-like honeycombs with self-similar hierarchy. Composite Structures. 2018;192:289-99.

[217] Jennett B, Teasdale G. Management of head injuries: FA Davis Company, 1981.

[218] Horgan TJ, Gilchrist MD. The creation of three-dimensional finite element models for simulating head impact biomechanics. International Journal of Crashworthiness. 2003;8:353-66.

[219] Ward C, Chan M, Nahum A. Intracranial pressure—a brain injury criterion. SAE Transactions. 1980:3867-80.

[220] Willinger R, Baumgartner D. Human head tolerance limits to specific injury mechanisms. International Journal of Crashworthiness. 2003;8:605-17.

[221] Sun G, Yu H, Wang Z, Xiao Z, Li Q. Energy absorption mechanics and design

optimization of CFRP/aluminium hybrid structures for transverse loading. International Journal of Mechanical Sciences. 2019;150:767-83.

[222] Lee K-H, Yi J-W, Park J-S, Park G-J. An optimization algorithm using orthogonal arrays in discrete design space for structures. Finite Elements in Analysis and Design. 2003;40:121-35.

[223] Hosseini SG, Eslami A. Orthogonal array design method for optimization experiments of sodium azide microencapsulation with stearic acid. Progress in Organic Coatings. 2010;68:313-8.

[224] Hosseini SG, Sharifnezhad H, Shirazi Z, Zohari N. Orthogonal array design method for optimization experiments of composite oxides (CuCr2O4/CuO) synthesis and investigation of their catalytic activity on thermal decomposition of ammonium perchlorate particles. Journal of Energetic Materials. 2022:1-19.

[225] Rafidah A, Nurulhuda A, Azrina A, Suhaila Y, Anwar IS, Syafiq RA. Comparison design of experiment (doe): Taguchi method and full factorial design in surface roughness. Applied Mechanics and Materials. 2014;660:275-9.

[226] Stufken J. Tagucbi Methods: A Hands-On Approach. Taylor & Francis; 1994.

[227] Park G-J, Hwang W-J, Lee W-I. Structural optimization post-process using Taguchi method. JSME international journal Ser A, Mechanics and material engineering. 1994;37:166-72.

[228] Phadke MS. Quality engineering using robust design: Prentice Hall PTR, 1995.

[229] Zhao X, Zhu G, Zhou C, Yu Q. Crashworthiness analysis and design of composite tapered tubes under multiple load cases. Composite Structures. 2019;222.

[230] Chinn B, Canaple B, Derler S, Doyle D, Otte D, Schuller E, Willinger R. COST 327 Motorcycle safety helmets. Review of Literature: Motorcycle Helmet; 2001.

[231] Hansen K, Dau N, Feist F, Deck C, Willinger R, Madey SM, Bottlang M. Angular impact mitigation system for bicycle helmets to reduce head acceleration and risk of traumatic brain injury. Accident Analysis and Prevention. 2013;59:109-17.

[232] Pang T, Li Y, Kang H, Sun G, Fang J, Li Q. On functionally-graded crashworthy shape of conical structures for multiple load cases. Journal of Mechanical Science and Technology. 2017;31:2861-73.

[233] Xu F. Enhancing material efficiency of energy absorbers through graded thickness structures. Thin-Walled Structures. 2015;97:250-65.

[234] Andena L, Caimmi F, Leonardi L, Nacucchi M, De Pascalis F. Compression of polystyrene and polypropylene foams for energy absorption applications: a combined mechanical and microstructural study. Journal of Cellular Plastics. 2019;55:49-72.

[235] Horvath JS. Expanded Polystyrene (EPS) geofoam: An introduction to material behavior. Geotextiles and Geomembranes. 1994;13:263-80.

[236] Atmatzidis DK, Missirlis EG, Chrysikos DA. An investigation of EPS Geofoam behaviour

in compression. Proceedings of EPS Geofoam. 2001:1-12.

[237] Khalaj O, Mohammad Amin Ghotbi Siabil S, Naser Moghaddas Tafreshi S, Kepka M, Kavalir T, Křížek M, Jeníček Š. The experimental investigation of behaviour of expanded polystyrene (EPS). IOP Conference Series: Materials Science and Engineering. 2020;723:012014.

[238] De Sousa RA, Gonçalves D, Coelho R, Teixeira-Dias F. Assessing the effectiveness of a natural cellular material used as safety padding material in motorcycle helmets. Simulation. 2012;88:580-91.

[239] Jeong KY, Cheon SS, Munshi MB. A constitutive model for polyurethane foam with strain rate sensitivity. Journal of Mechanical Science and Technology. 2012;26:2033-8.

[240] Shah QH, Topa A. Modeling large deformation and failure of expanded polystyrene crushable foam using LS-DYNA. Modelling and Simulation in Engineering. 2014;2014:1-7.

[241] Willinger R, Baumgartner D, Guimberteau T. Dynamic characterization of motorcycle helmets: modelling and coupling with the human head. Journal of Sound and Vibration. 2000;235:611-25.

[242] Hu J, Wei L. Study on the energy absorption characteristics of expanded polystyrene foam. Chinese Journal of Applied Mechanics. 2015;32:430-4.

[243] Cronin DS, Ouellet S. Low density polyethylene, expanded polystyrene and expanded polypropylene: Strain rate and size effects on mechanical properties. Polymer Testing. 2016;53:40-50.

[244] Chen W, Hao H, Hughes D, Shi Y, Cui J, Li Z-X. Static and dynamic mechanical properties of expanded polystyrene. Materials & Design. 2015;69:170-80.

[245] Lei Z, Yao X, Long S, Chang J, Wang H. Dynamic compression characteristics of polystyrene foam materials. Chinese Journal of High Pressure Physics. 2019;33:1-10.

[246] ASTM D1621-16 Standard test method for compressive properties of rigid cellular plastics. ASTM International; 2016.

[247] Reid SR, Reddy TY, Gray MD. Static and dynamic axial crushing of foam-filled sheet metal tubes. International Journal of Mechanical Sciences. 1986;28:295-322.

[248] Sun Y, Li QM. Dynamic compressive behaviour of cellular materials: A review of phenomenon, mechanism and modelling. International Journal of Impact Engineering. 2018;112:74-115.

[249] Sun Y, Li QM, Lowe T, McDonald SA, Withers PJ. Investigation of strain-rate effect on the compressive behaviour of closed-cell aluminium foam by 3D image-based modelling. Materials & Design. 2016;89:215-24.

[250] Ozturk UE, Anlas G. Finite element analysis of expanded polystyrene foam under multiple compressive loading and unloading. Materials & Design. 2011;32:773-80.

[251] Zheng Z, Wang C, Yu J, Reid SR, Harrigan JJ. Dynamic stress–strain states for metal

foams using a 3D cellular model. Journal of the Mechanics and Physics of Solids. 2014;72:93-114.

[252] Chen Y, Bai Z, Zhang L, Wang Y, Sun G, Cao L. Crashworthiness analysis of octagonal multi-cell tube with functionally graded thickness under multiple loading angles. Thin-Walled Structures. 2017;110:133-9.

[253] Xiao Z, Fang J, Sun G, Li Q. Crashworthiness design for functionally graded foam-filled bumper beam. Advances in Engineering Software. 2015;85:81-95.

[254] Li G, Zhang Z, Sun G, Xu F, Huang X. Crushing analysis and multiobjective optimization for functionally graded foam-filled tubes under multiple load cases. International Journal of Mechanical Sciences. 2014;89:439-52.

[255] Watanabe R, Katsuhara T, Miyazaki H, Kitagawa Y, Yasuki T. Research of the relationship of pedestrian injury to collision speed, car-type, impact location and pedestrian sizes using human FE model (THUMS Version 4). SAE Technical Paper; 2012. p. 269-321.

[256] Pellman EJ, Viano DC, Withnall C, Shewchenko N, Bir CA, Halstead PD. Concussion in professional football: helmet testing to assess impact performance--part 11. Neurosurgery. 2006;58:78-95.

[257] Chu C-S, Lin M-S, Huang H-M, Lee M-C. Finite element analysis of cerebral contusion. Journal of Biomechanics. 1994;27:187-94.

[258] Li K, Wang J, Liu S, Su S, Feng C, Fan X, Yin Z. Biomechanical behavior of brain injury caused by sticks using finite element model and Hybrid-III testing. Chinese Journal of Traumatology. 2015;18:65-73.

[259] Bain AC, Meaney DF. Tissue-level thresholds for axonal damage in an experimental model of central nervous system white matter injury. Journal of Biomechanical Engineering. 2000;122:615-22.

[260] Deck C, Willinger R. Improved head injury criteria based on head FE model. International Journal of Crashworthiness. 2008;13:667-78.

[261] Hoshizaki TB, Post A, Kendall M, Cournoyer J, Rousseau P, Gilchrist MD, Brien S, Cusimano M, Marshall S. The development of a threshold curve for the understanding of concussion in sport. Trauma (London, England). 2017;19:196-206.

[262] Willinger R, Ryan GA, McLean AJ, Kopp CM. Mechanisms of brain injury related to mathematical modelling and epidemiological data. Accident Analysis & Prevention. 1994;26:767-79.

[263] Gennarelli TA, Thibault LE, Ommaya AK. Pathophysiologic responses to rotational and translational accelerations of the head. Proceedings of 16th stapp car crash conference: Society of Automotive Engineers; 1972. p. 269–308.

[264] Hirsch AE, Ommaya AK, Mahone RM. Tolerance of subhuman primate brain to cerebral concussion. Naval Ship Research and Development Center; 1968.

[265] Yang C, Li QM. Dual damage criteria in a crash stop. International Journal of Mechanical Sciences. 2020;183.

Appendix A: Head Responses under Frontal Translational Acceleration Loads

The different typical frontal translational acceleration loads were applied to head impact simulations in **Chapter 5** to investigate the interactive influences of various acceleration loading configurations, i.e. impact duration and peak magnitude with different loading curve shapes, on head responses. Tissue-level injury predictors, i.e. intracranial pressure, von Mises stress and maximum principal strain, for the head under different frontal translational acceleration loads are presented in the following Figures.
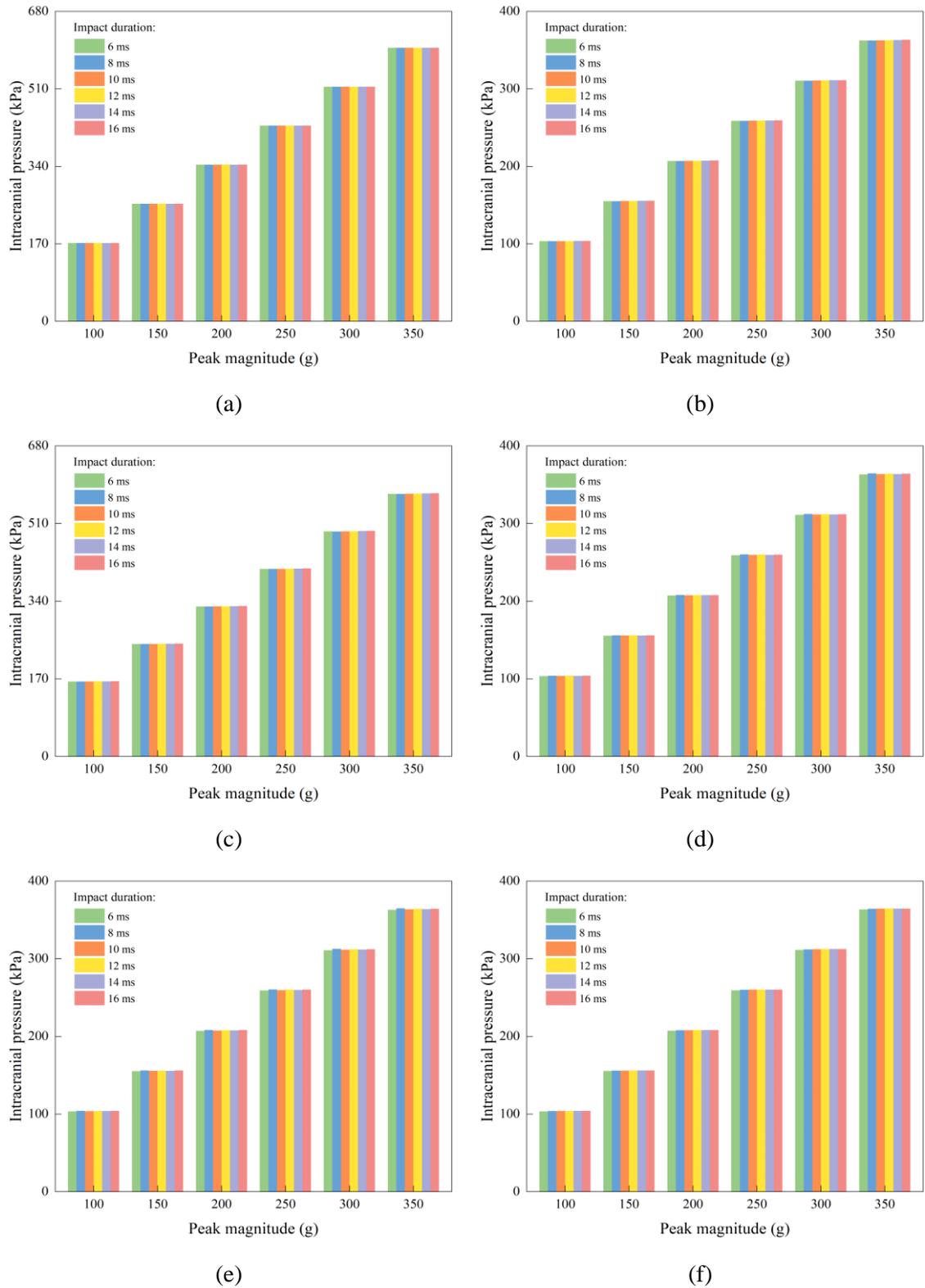
(a)

(b)

(c)

(d)

(e)

(f)

Figure A.1. The intracranial pressure results for the head model subjected to frontal translational acceleration loads with six different loading curve shapes, (a) ESS, (b) EPTS, (c) ENTS, (d) EITS, (e) EHSS, (f) EHVS
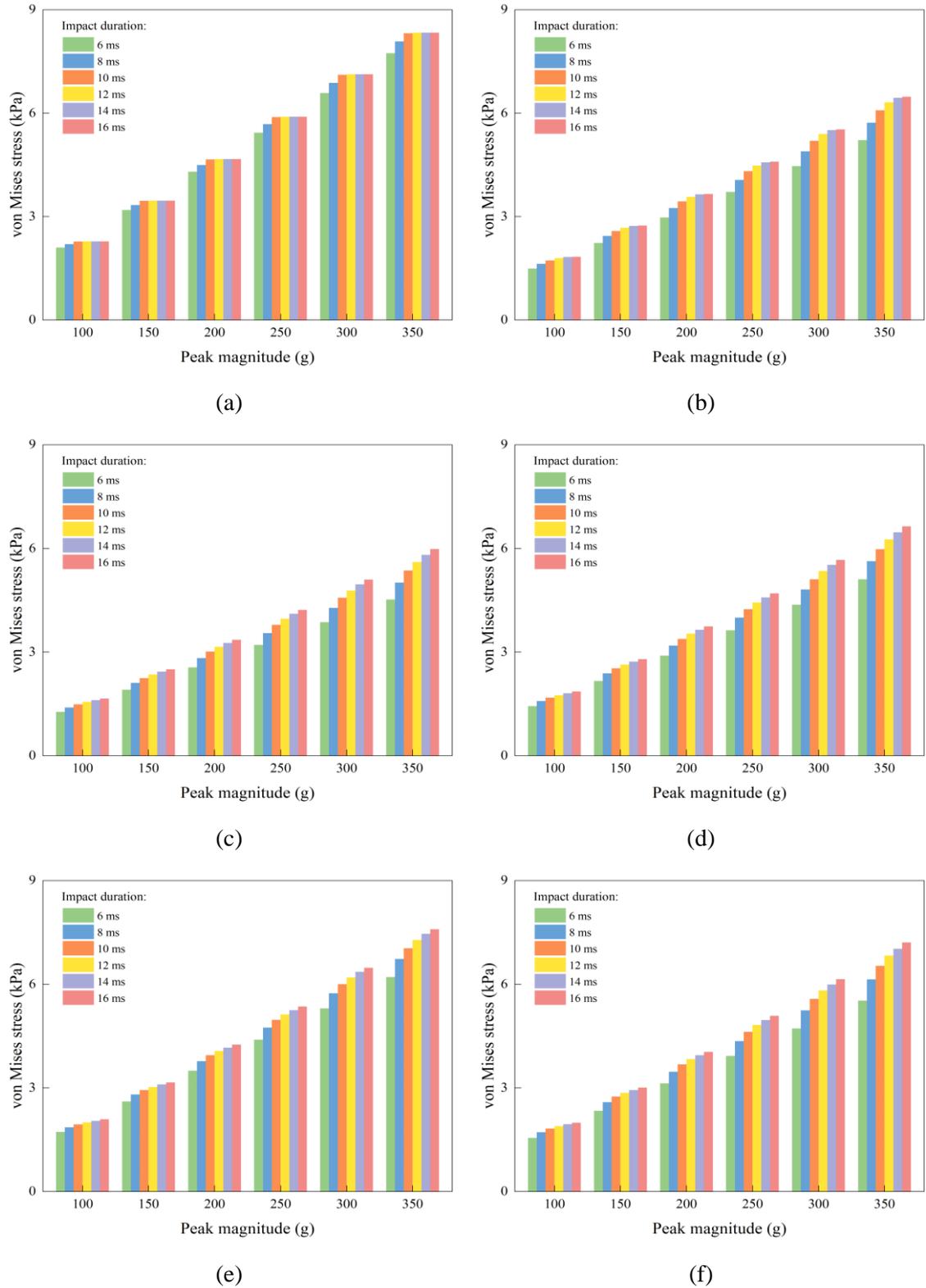
(a)

(b)

(c)

(d)

(e)

(f)

Figure A.2. The von Mises stress results for the head model subjected to frontal translational acceleration loads with six different loading curve shapes, (a) ESS, (b) EPTS, (c) ENTS, (d) EITS, (e) EHSS, (f) EHVS
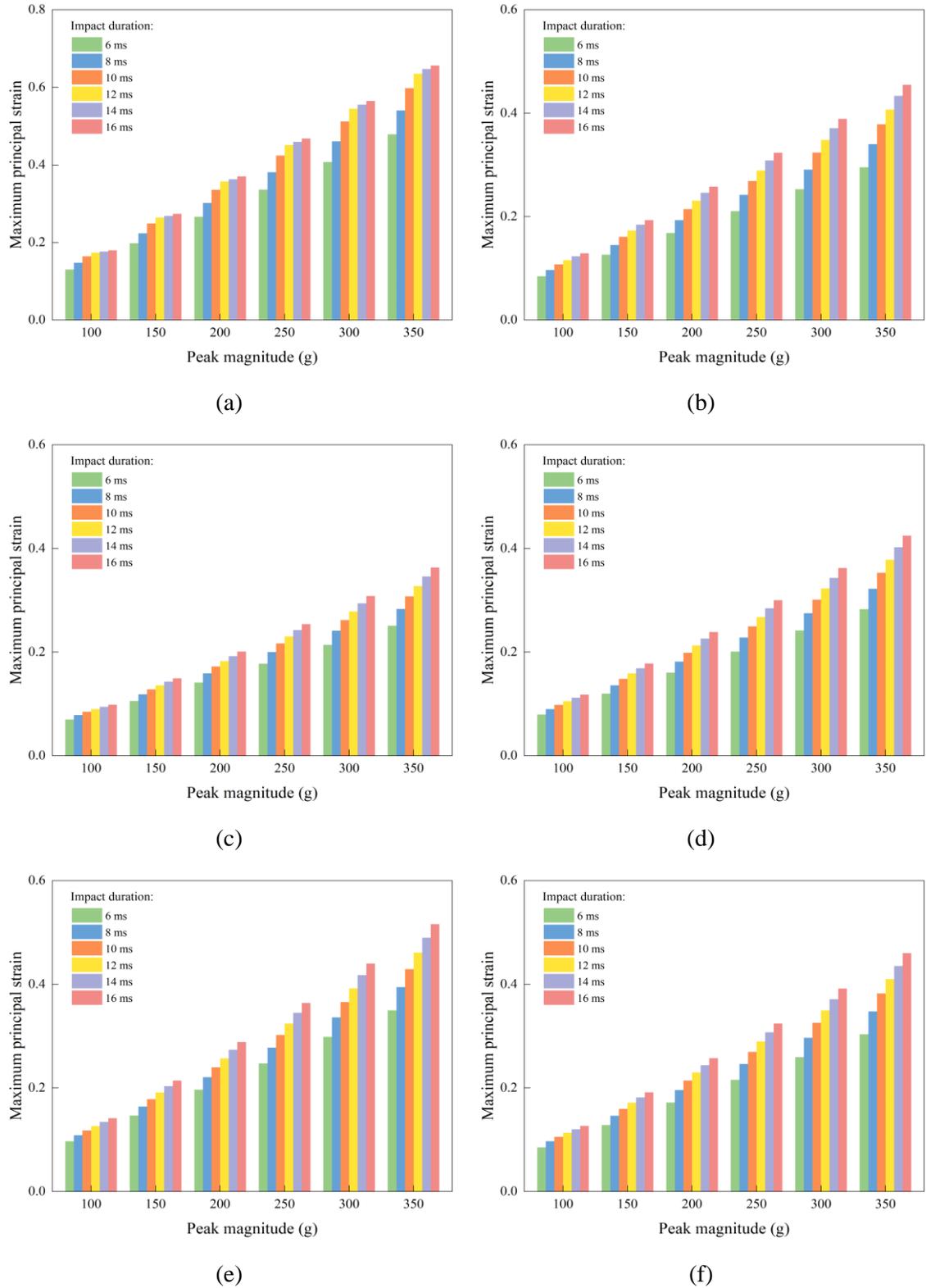
(a)

(b)

(c)

(d)

(e)

(f)

Figure A.3. The maximum principal strain results for the head model subjected to frontal translational acceleration loads with six different loading curve shapes, (a) ESS, (b) EPTS, (c) ENTS, (d) EITS, (e) EHSS, (f) EHVS